

2

PL-TR-91-2105

AD-A240 070



NEAR SOURCE CONTRIBUTIONS TO TELESEISMIC P WAVE
CODA AND REGIONAL PHASES

Thorne Lay

University of California, Santa Cruz
Earth Sciences Board
Santa Cruz, CA 95064

27 April 1991

DTIC
ELECTE
SEP 05 1991
S B D

Final Report
1 January 1989-31 December 1990

APPROVED FOR PUBLIC RELEASE; DISTRIBUTION UNLIMITED



PHILLIPS LABORATORY
AIR FORCE SYSTEMS COMMAND
HANSCOM AIR FORCE BASE, MASSACHUSETTS 01731-5000

91-09623

07 0 A 0tef

SPONSORED BY
Defense Advanced Research Projects Agency
Nuclear Monitoring Research Office
ARPA ORDER NO. 5299

MONITORED BY
Phillips Laboratory
Contract F19628-89-K-0011

The views and conclusions contained in this document are those of the authors and should not be interpreted as representing the official policies, either expressed or implied, of the Defense Advanced Research Projects Agency or the U.S. Government.

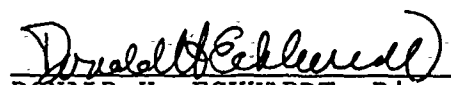
This technical report has been reviewed and is approved for publication.



JAMES F. LEWKOWICZ
Contract Manager
Solid Earth Geophysics Branch
Earth Sciences Division



JAMES F. LEWKOWICZ
Branch Chief
Solid Earth Geophysics Branch
Earth Sciences Division



DONALD H. ECKHARDT, Director
Earth Sciences Division.

This report has been reviewed by the ESD Public Affairs Office (PA) and is releasable to the National Technical Information Service (NTIS).

Qualified requestors may obtain additional copies from the Defense Technical Information Center. All others should apply to the National Technical Information Service.

If your address has changed, or if you wish to be removed from the mailing list, or if the addressee is no longer employed by your organization, please notify PL/IMA, Hanscom AFB, MA 01731-5000. This will assist us in maintaining a current mailing list.

Do not return copies of this report unless contractual obligations or notices on a specific document requires that it be returned.

(Block 13, continued)

point velocity can be inferred from teleseismic signals. Such observations have the potential to both improve yield estimation (by indicating coupling conditions) and to shed light on the basic mechanisms of coda excitation. Reliable isolation of any near-source influences requires thorough suppression of propagation and near-receiver effects on the signals, which are shown herein to be significant for comparisons of P and P coda. A spectral factoring procedure is used to determine event-averaged source spectra from which propagation and receiver terms have been removed for both direct P signals and early P coda. A large short-period waveform data set (2457 signals) for 71 events at the Nevada and Novaya Zemlya test sites is analyzed with the event-averaging procedure. Spectral ratios, and slopes of spectral ratios, for the event-averaged P and P coda source terms are examined for dependence on event magnitude, burial depth, overburden velocity and other known source characteristics. The slopes of P/P coda ratios for NTS events show only weak dependence on near-source properties for the event-averaged spectra, while individual stations sometimes show strong systematic trends, as discovered by Gupta and Blandford (1987). The tendency is for larger, deeper events (with higher average overburden velocities) to have relative enrichment of high frequency P wave energy compared to the coda. At frequencies less than 0.6 Hz, single frequency P/P coda spectral ratios increase with increasing magnitude, depth and overburden velocity. For Novaya Zemlya, the slope of P/P coda shows a strong variation with magnitude, but P -waves from larger events have relatively *depleted* high frequency content. Differences in magnitude-depth scaling may account for this difference between test sites. Single frequency P/P coda spectral ratios at frequencies less than 1.0 Hz increase with magnitude for Novaya Zemlya similarly to the NTS events, possibly as a result of enhanced coda excitation for shallower events combined with low frequency pP interference. These variations are not yet quantitatively understood, but may ultimately provide empirical procedures for characterizing the near-source environment of isolated events or additional test site explosions.

Energy radiated upward from underground nuclear explosions has a complex interaction with the free surface that strongly influences the seismic wavefields recorded at teleseismic and regional distances. This interaction, differing from that for earthquakes primarily due to the much higher strains and strain rates involved, is essential to understand for both explosion yield estimation and event discrimination. Reflection of explosion P wave energy from the free surface, which produces the pP phase, involves frequency-dependent, non-linear processes that are intimately linked to surface spallation. Attempts to characterize the teleseismic pP arrival using a variety of time series analysis procedures have yielded seemingly inconsistent results, which can be attributed to a combination of limited bandwidth, neglected frequency dependence, and unresolved trade-offs with source time function, receiver and attenuation effects. Recovery of broadband ground displacement, now viable with modern instrumentation, is resulting in more robust characterizations of the pP and spallation arrivals; however, the intrinsic trade-offs with source parameters and attenuation remain. Numerical procedures to account for the non-linear interactions, surface topographic effects, and shallow crustal heterogeneity are enabling a more complete modeling of the free surface interaction.

Table of Contents:

Chapter 1.		1
	Near-Source Contributions to Teleseismic P-Waves and P-Wave Coda for Underground Explosions.	
Chapter 2.		33
	The Teleseismic Manifestation of pP: Problems and Paradoxes	
Chapter 3.		81
	Nuclear Testing and Seismology	



Accession For	
NTIS GRA&I	<input checked="" type="checkbox"/>
DTIC TAB	<input type="checkbox"/>
Unannounced	<input type="checkbox"/>
Justification	
By _____	
Distribution/	
Availability Codes	
Dist	Avail and/or Special
A-1	

Chapter 1

Near-Source Contributions to Teleseismic P-Waves and P-Wave Coda for
Underground Explosions

by

Thorne Lay and Tianrun Zhang

Abstract

Characterization of near source crustal properties for underground nuclear explosions using distant seismic observations can potentially improve nuclear test monitoring capabilities. Previous analyses of the relative spectral content of direct P -waves and P -wave coda have suggested that important physical parameters such as source overburden velocity and shot point velocity can be inferred from teleseismic signals. Such observations have the potential to both improve yield estimation (by indicating coupling conditions) and to shed light on the basic mechanisms of coda excitation. Reliable isolation of any near-source influences requires thorough suppression of propagation and near-receiver effects on the signals, which are shown herein to be significant for comparisons of P and P coda. A spectral factoring procedure is used to determine event-averaged source spectra from which propagation and receiver terms have been removed for both direct P signals and early P coda. A large short-period waveform data set (2457 signals) for 71 events at the Nevada and Novaya Zemlya test sites is analyzed with the event-averaging procedure. Spectral ratios, and slopes of spectral ratios, for the event-averaged P and P coda source terms are examined for dependence on event magnitude, burial depth, overburden velocity and other known source characteristics. The slopes of P/P coda ratios for NTS events show only weak dependence on near-source properties for the event-averaged spectra, while individual stations sometimes show strong systematic trends, as discovered by Gupta and Blandford (1987). The tendency is for larger, deeper events (with higher average overburden velocities) to have relative enrichment of high frequency P wave energy compared to the coda. Single frequency P/P coda spectral ratios increase with increasing magnitude, depth and overburden velocity for frequencies less than 0.5 Hz, with these trends being reversed near 0.8 Hz. For Novaya Zemlya, the slope of P/P coda shows a strong variation with magnitude, but P -waves from larger events have relatively *depleted* high frequency content. Differences in magnitude-depth scaling may contribute to this difference between test sites. Single frequency P/P coda spectral ratios at frequencies less than 1.0 Hz increase with magnitude for Novaya Zemlya similarly to the NTS events, possibly as a result of enhanced coda excitation for shallower events combined with low frequency pP interference. These variations are not yet quantitatively understood, but may ultimately provide empirical procedures for characterizing the near-source environment of isolated events or additional test site explosions.

Introduction

Seismic radiation from underground nuclear explosions provides the primary means by which explosion parameters and source region properties can be determined. Source region properties influence the coupling and energy partitioning of the seismic radiation, so accurate explosion yield estimation requires knowledge of the source environment. Unfortunately, the amplitude and spectral influences of the source environment are masked by propagation effects along the entire path to the receiver. In order to isolate the source medium influence, several recent studies have advocated analysis of the differential energy content of direct *P*-wave signals and *P*-wave coda (e.g. Gupta and Blandford, 1987; Lay and Welc, 1987; Lay, 1987; Lynnes and Lay, 1988a, Murphy and O'Donnell, 1987). Relative comparisons of signals in the same wavetrain at a given station intrinsically eliminate common source radiation and receiver propagation effects, potentially revealing event-to-event variations in energy flux caused by near-source factors. Experience with *P*-wave coda indicates that it can provide a relatively stable reference signal that highlights the more pronounced variations in the *P* phase (e.g. Bullitt and Cormier, 1984; Gupta et al., 1985; Lay and Welc, 1987). However, it is also known that *P* coda can be systematically affected by regional heterogeneity (Lay and Welc, 1987) and the excitation of the coda is poorly understood, so relative variations between *P* and *P* coda cannot be automatically attributed entirely to *P*.

Both time-domain and frequency-domain comparisons of *P* and *P* coda have revealed interesting patterns that appear to vary with source environment. Time-domain studies of energy flux in different frequency passbands have shown that for frequencies less than about 0.7 Hz *P/P* coda energy ratios increase with magnitude for events at the Nevada, Amchitka, and Novaya Zemlya test sites (Lay, 1987; Lynnes and Lay, 1988a). This has been interpreted as the result of enhanced low frequency coda excitation for shallower (smaller) events (Lay, 1987). At intermediate frequencies around 1.0 Hz, interference with the *pP* arrival causes highly variable magnitude scaling of the *P/P* coda energy ratio, primarily because scalloping due to the *pP* phase affects the direct *P* signal window but not the *P* coda energy (Gupta and Blandford, 1987; Lay, 1987; Lynnes and Lay, 1988a). Frequency-domain comparisons, involving *P/P* coda spectral ratios over a broader frequency range (0.5-3.0 Hz), show even more interesting trends. Gupta and Blandford (1987) found that the slopes of the spectral ratios of *P/P* coda for an isolated NORSAR channel (NA0) and a NORSAR subarray (1A) show systematic increases with average overburden velocity, working-point velocity, and burial depth for 20 NTS events at Pahute Mesa and Yucca Flat. Their interpretation is that enrichment of high frequency content of

the direct P wave due to increasing depth occurs, as predicted by Mueller and Murphy (1971) source scaling, whereas the P coda is relatively stable because the energy averages a large volume around the shot point. The volume averaging property of the coda may intrinsically reduce its sensitivity to the localized overburden velocity, although this idea has not yet been fully quantified.

In the study by Gupta and Blandford (1987) it was mentioned that the P/P coda behavior showed large variations with both azimuth and epicentral distance, thus the generality of the NORSAR results is unclear. If strong near-source influences on the relative spectral content of P and P coda exist, it is reasonable to expect a similar effect at all recording stations. This paper will further pursue the frequency domain P/P coda comparison approach using an extensive data set for many more events and receivers. At this stage, the investigation is still empirical, as full quantification of the P coda wavefield is beyond our present capabilities. Significant differences in the energy partitioning for explosions in different media are observed, which will provide the basis for future efforts to fully quantify the seismic signal sensitivity to the near-source environment.

Data Analysis Procedures

The data set used in this analysis is the same as has been examined in earlier time-domain investigations of near-source influences on teleseismic P waves (Lay, 1987; Lynnes and Lay, 1988a). It is comprised of short-period vertical component recordings for underground explosions at the Nevada (NTS) and Novaya Zemlya test sites. The waveforms were recorded at globally distributed WWSSN and Canadian Seismic Network (CSN) stations and were manually digitized. The total number of digitized waveforms available for this study is 2457, from 25 Pahute Mesa, 32 Yucca Flat, and 14 Novaya Zemlya events. Only stations in the distance range 25° to 95° were used for each test site, giving 71 stations for NTS events and 90 stations for the Soviet tests. The complete set of waveforms, and full event information have been presented elsewhere (Burger et al., 1985; Lay et al., 1986; Lay, 1987).

For most of the signals, about 30 sec of the P waveform was digitized, as well as a 10-15 sec noise window, so our signal windowing was constrained to be slightly different than that of Gupta and Blandford (1987). The direct P signal window was taken to be a 6.4 sec interval initiating 1.4 sec prior to the first arrival. Cosine tapers were applied to the start and end of this window, such that the spectrum emphasizes the first 3.5 sec of the P arrival. Note that this corresponds to the $P(6.4 \text{ sec})$ window of Gupta and Blandford (1987), and includes the pP arrival as well as the next two cycles of the waveform, which

may include spall and near-source scattered energy. Conventional fast Fourier transforms were used to estimate the spectra. The amplitude spectra were computed from the noise-corrected power spectra with normalization for differing window lengths, and were corrected for the varying instrument responses. The amplitudes were also corrected for geometric spreading to a reference distance of 50° using the Veith-Clawson (1972) curve. Murphy et al. (1989) have shown that this spreading correction appears to be valid over the 0.5-2.25 Hz spectral range.

For the *P* coda window, we used 12.8 and 19.2 sec duration intervals immediately after the *P* window, again applying moderate tapers and omitting traces with digitized coda windows short of the desired length by more than 2 sec. The results shown in this paper are all for the 12.8 sec coda window, as this provided a more extensive data set with somewhat better stability. Spectral points with signal/noise ratios less than 1.5 were excluded. In general, it would be desirable to have a longer coda window, but both the digitized signal lengths and the low signal-to-noise ratio for the coda motivated us to use the shorter window, which we refer to as the early *P* coda. The results found for the 19.2 sec window are very similar to those shown here, leading us to expect that the window length is not critical, given the extent of averaging in our analysis.

The limited resolution of the hand-digitized data and the limited bandwidth observed for highly attenuated signals from the NTS constrain our useful frequency band to the interval 0.3-2.5 Hz, with the lowest signal-to-noise ratios typically being at frequencies less than 0.4 Hz. This is again not ideal for resolution of subtle near-source effects; however, digital data sets are sparse for the large historic events that we consider in this study. Hopefully, the extensive averaging that is performed offsets the limitations of the hand-digitized data, although we are aware of the possibility that a single high quality digital station may have comparable resolution to our global data set for certain applications.

Motivated by the interesting results of Gupta and Blandford (1987), we initially considered individual station spectral ratios of *P/P* coda, computing the slope of the logarithm (base 10) of the ratio for each event. The spectral ratio confidence intervals were obtained using the noise spectra in the maximum likelihood estimation procedure from Nakanishi (1979), with the confidence intervals then being used as weighting factors in a least squares regression for a best fit linear slope. Regressions were performed over the band 0.3-2.5 Hz, for data points satisfying the signal-to-noise criterion for both *P* and *P* coda spectra. Following Gupta and Blandford (1987), the slopes of the spectral ratios were compared with known source information, including first-cycle magnitudes, or $m_b(ab)$ (Lay et al., 1986), source depth, average working point velocity and average overburden velocity for each event.

Figure 1 shows the single station results obtained for two WWSSN stations that recorded many of the 57 NTS events. Station KON is co-located with digital station KONO, for which Gupta and Blandford (1987) report results similar to their analysis of NORSAR data. It is encouraging to find that KON does display the expected increase in P/P coda slopes with increasing average overburden velocity. The correlation coefficient for this comparison is 0.592, with a regression slope of 0.168 sec/km. Station ARE is at a substantially different azimuth, but the regression with overburden velocity also has a positive slope (0.281 sec/km) with a correlation coefficient of 0.637. The corresponding numbers found for NORSAR station NAO are 0.236 sec/km with correlation 0.869, for a different population of events (Gupta and Blandford, 1987). The scatter in the WWSSN data appears to be somewhat greater, but a substantially larger data set is included. The qualitative consistency indicates that the analog data are adequate for this analysis. As was the case for NAO, the correlations and regression slopes are slightly reduced for the comparisons with working point velocity for KON and ARE. Comparable correlations are found for $m_b(ab)$ and depth, reflecting the general tendency for the velocity measures to increase with burial depth.

Sixteen stations, each recording more than 35 of the NTS events, were similarly processed, with the results for regressions on overburden velocity being given in Table 1. It turns out that ARE and KON are the two stations with the highest correlations and largest regression slopes for overburden velocity. Stations at similar azimuths can have significantly different P/P coda behavior, as was noted by Gupta and Blandford (1987). Note that NUR, a high quality station close to KON, has negligible regression slope and a low correlation. The underlying cause of this variability is illustrated in Figure 2. The P and P coda spectra, and their ratios, are shown for two CSN stations that recorded the same Pahute Mesa event, TYBO. Both stations have favorable signal-to-noise characteristics, but the spectral ratios have much different slopes. Over a suite of events, the slopes do not necessarily vary systematically in a fashion that would indicate a simple site-dependent change in reference slope. This gives rise to the inconsistent results in Table 1. Confronted with the fact that only a few isolated stations show a significant trend, one must appraise the degree to which near-source information has been isolated by the ratioing procedure.

There is cause for concern that NORSAR and KON may have anomalous behavior along the paths of the direct P waves for NTS events. Lynnes and Lay (1988b) demonstrate that teleseismic stations at azimuths to the northeast of NTS have anomalously low amplitudes and early arrival times for all NTS events, with more pronounced patterns for Pahute Mesa events. This is believed to be caused by defocussing by mantle velocity

heterogeneity in the crust and upper mantle beneath Pahute Mesa as well as larger scale heterogeneity deeper than 400 km beneath the Basin and Range province. The early *P* coda exhibits similar amplitude variations, but with a reduced range (Lay and Welch, 1987), indicating that some differential effect may accumulate due to the spatial averaging properties of the coda. The Yucca Flat and Pahute Mesa event populations have limited overlap in Figure 1, raising the possibility of an intersite baseline shift, but even the Pahute Mesa data alone suggest correlations, as is true of Gupta and Blandford's (1987) data for NA0 (see their Figure 4). The fact that ARE is at a much different azimuth, but shows similar correlations to those at KON is not easily explained by mantle heterogeneity. It is possible that only rare points or regions, such as Norway, may be sensitive to the near-source effect.

An alternative interpretation of the station variability of *PIP* coda is that the processes shaping the two spectra are highly variable from station to station, requiring a procedure that suppresses the site contributions for each signal type before any subtle near-source variations can be detected. Figure 2 gives credence to this possibility, and thus we pursue a spectral-factoring approach in the remainder of this paper. The separation of source and site spectral factors is accomplished using a least-squares procedure similar to that introduced by Murphy et al. (1989) and Murphy (1989). In this procedure frequency dependent station correction factors and network-averaged source spectra are determined for a suite of events recorded at a global array of stations. For the observed $m_{ij}(f)$, which are logarithms of the *P* or *P* coda spectral amplitude at frequency *f* at station *j* from event *i*, a least-squares procedure minimizes the residual error for the model:

$$m_{ij}(f) = M_i(f) + S_j(f) + \epsilon_{ij}(f)$$

where $M_i(f)$ is the event-averaged logarithmic source amplitude, $S_j(f)$ is the logarithmic station correction for station *j*, and ϵ_{ij} is a Gaussian distributed error term with zero mean. The simultaneous inversion for the source and receiver terms is constrained so that for each frequency point, the sum of the $S_j(f)$ over the number of observing stations is zero. Thus, common effects on the spectra, such as caused by the upper mantle attenuation under the test site, are contained in the $M_i(f)$ terms. The $S_j(f)$ terms then contain the systematic frequency dependent propagation terms that deviate from the network average. Murphy et al. (1989) show that as long as the number of observations at each station is 5 or more the resulting factorization process results in smooth, stable source spectra.

Two analyses were performed using this spectral factoring procedure. First, event-averaged spectra were obtained separately for the *P* and *P* coda windows, and then ratios of

the average spectra were examined for near-source influences. Separate site correction spectra for P and P coda windows were obtained and can be examined to understand the variations seen in Figure 2. In the second approach, P/P coda spectral ratios were first computed for each observation, and the ratioed spectra were put into the event-averaging procedure. This procedure results in an event-averaged P/P coda spectral ratio, as well as spectral ratio site terms. The latter procedure reduces instrument correction effects and gives a different intrinsic weighting to the data entering the factoring procedure. We found that the two approaches give very similar results for the final P/P coda spectral ratios, mainly because of the large number of data available for the analysis. This paper only presents results for the first procedure, in which separate event-averaged spectra are determined.

Results for the Nevada Test Site

The Pahute Mesa and Yucca Flat event populations were treated separately, given the concern about potential inter-subsite propagation differences like those studied by Lynnes and Lay (1988b). Since the events are relatively tightly clustered in each subsite, it is reasonable to assume that the scattering processes contributing to the receiver terms for both P and P coda windows are fairly stable for each event population. The event-averaged P and P coda spectra for the 25 Pahute Mesa events are shown in Figure 3. As demonstrated by Murphy et al. (1989), the source spectra obtained by the least-squares processing are quite smooth. The spectra are not particularly sensitive to the precise set of stations used, as long as a large number of data are available. Murphy (1989) has obtained corresponding network-averaged spectra for Pahute Mesa events, and shows that normalization by a Mueller-Murphy (1971) source model indicates an apparent t^* value of around 0.75 s as an average value over this frequency band. We do not need to consider the absolute source parameters in this study, as all of our results involve ratios relative to the P coda spectra, which should have a common average t^* effect.

The event-averaged P spectra have stronger scalloping around 1 Hz than the P coda spectra, and a somewhat greater overall range. This is believed to represent an enhanced effect of the free surface reflection, pP in the direct phase spectra. If the pP phase is modeled as a delayed echo of the direct arrival, the estimated pP lag times required to produce the scalloped arrivals are found by Murphy (1989) to have very consistent delays to those inferred by relative waveform inversion (Lay, 1985); however, the apparent pP delay times are anomalously long with respect to the known burial depths and overburden velocities, as is commonly observed for explosions (Lay, 1991). The inferred pP

amplitudes are also significantly reduced compared to those expected for an elastic free surface reflection, which would predict deeper regularly spaced scalloping. To some degree the spectral nulls are smoothed out by the spectral carpentry and the event-averaging procedure, but the absence of clear higher frequency scalloping does indicate that the free surface reflection is probably complex and frequency-dependent. The absence of associated scalloping in the coda spectra is probably due to a combination of more extensive averaging and a dominance of the coda by waves that left the source more horizontally, as both body and surface waves, before scattering into the teleseismic wavefield. The contribution from near-receiver generated coda produced by scattering of the direct P arrival appears to be homogenized to such a degree that it also loses any pP character. These spectra thus clearly do contain variable near-source information, and our objective is to determine whether systematic trends with important source parameters can be detected.

The spectral factoring procedure also returns frequency-dependent site factors for each source region. Examples are shown for the Pahute Mesa source region in Figure 4. The site factors for the two CSN stations from Figure 2 are shown, for P and P coda. As expected, the two stations display significant differences in the relative behavior of the P and P coda terms, such that the P/P coda ratios are systematically different at the two stations. The site factors are plotted so that the negative value of the regression slopes are proportional to the path differential t^* , relative to the overall array mean. Both stations are in the North West Territories, but BLC is in the craton, while INK is on the western platform margin. BLC has relatively negative (fast) P and S wave travel time anomalies (Wickens and Buchbinder, 1980; Lay and Helmberger, 1983), thus one might anticipate that it would have a less attenuating path as suggested by the positive slope for the P window. However, the P coda window does not reflect this, indicating that the scattered arrivals encounter higher scattering or intrinsic attenuation. The P factors are not as smooth as P coda factors for either station, indicating that site resonances shape the spectra as well as differential path attenuation. Corresponding station spectra for the Pahute Mesa events were extracted for all 71 stations, and generally exhibit comparable behavior. The Yucca Flat event set gives similar station terms and comparable variations between P and P coda station factors. The spectral factorization was also applied using all 57 NTS events in a simultaneous inversion. The event-averaged spectra are very similar to those obtained in the separate subsite inversions. It appears that even the subsite data sets are sufficient to provide stable characterization of the source spectra. The results shown in this paper are for the separate subsite results, but are very similar to those for the combined inversion.

Ratios of the event-averaged P and pP coda spectra for each NTS event were computed, with the variance estimates on the individual spectral estimates being used to calculate confidence intervals on the ratio. The confidence intervals were then used as inverse weighting factors in a linear regression over the frequency range 0.3 to 2.5 Hz. Figure 5 shows representative examples of this procedure for two of the Pahute Mesa tests. Event PIPKIN is a low-magnitude event with a shallow (0.62 km) burial depth, while COLBY is a large event with a burial depth of 1.27 km. Note that the logarithmic ratios emphasize the differential scalloping of the spectra due to the pP effect. The spectral ratios are quite smooth relative to single station ratios (see Figure 2). While these events are substantially different in magnitude and burial depth, the P/P coda ratios both have very flat slopes, and the most notable differences are in the shift to lower frequencies of the main scalloping null for the larger event, and the baseline shift of the ratios to values greater than 1 for the larger event. The larger event does have a slightly more positive slope. The lowest frequency spectral point is unstable primarily because of low signal-to-noise and uncertainty in low frequency instrument responses, so it was not used in the regressions. Spectral fitting procedures like those used by Murphy (1989) can be applied to correct the P spectra scalloping for a model of the pP phase, potentially improving the sensitivity of the spectral ratio slope estimates, but we have not pursued this because of the uncertainty in the frequency dependence of the process resulting in low pP amplitudes and reduced high frequency scalloping.

Similar results are shown for two Yucca Flat events in Figure 6. The set of events at this test site only span a limited range in magnitude, of about 0.5 magnitude units, so it is necessary to combine these events with the Pahute Mesa events to explore a wide range in source parameters. The Yucca Flat events do commonly show scalloping around 1 Hz, which is likely due to a free surface interaction, although anomalous pP parameters are again implied. The Yucca Flat data are more limited in bandwidth because the events are small and the waveforms of the direct P signal are complex. There is again a very slight tendency for the larger events to have more positive slopes.

In order to establish whether the near-source environment has any systematic effect on the P/P coda relative behavior, the slopes of the ratios were compared with a variety of source parameters. The results of some of the comparisons that were made are shown in Figure 7. The standard deviation of the regression slopes is used to define weighting factors in regressions on each of the near-source parameters. The combined NTS data set of 57 events indicates very little explicit dependence on event size, with slightly positive slopes and correlation coefficients of only 0.245 and 0.197 for $m_b(ab)$ and $m_b(ISC)$ respectively. There is a stronger influence of burial depth, with a slightly increased

correlation coefficient of 0.305, but the correlation improves significantly to 0.542 if the distance to water table is used (all of the events used are at or below the water table). The NTS data have a moderate dependence on average overburden velocity, with a positive slope of 0.034 sec/km, and a correlation coefficient of 0.462. Average overburden velocities were not available for every event, so only 34 points were used in this determination, compared to 20 for Gupta and Blandford (1987). As in their study, there is a distinct tendency for the Yucca Flat ratio slopes to be more negative than those of Pahute Mesa events, thus some of this trend is defined by an intersite difference that may have a complex relationship to the differences in the near-source structure. The range of *PIP* coda slope variations is much smaller for our event-averaged results than for the NORSAR or some other single station values, and the trends are reduced correspondingly, but still have the same general tendency. As was the case in the study by Gupta and Blandford (1987), the correlation with working point velocity is reduced relative to those for overburden velocity and depth. Comparisons with other near-source factors such as tectonic release *F*-factor, *pP* lag times, explosion moments, and explosion yield all show at most slight positive trends, with correlations less than that for source depth.

The results in Figure 7 are consistent with the variability suggested by the individual station analyses summarized in Table 1. Relative to the strong trends for a few isolated stations such as NAO, KON and ARE, the combined *PIP* coda behavior shows much more subdued trends with near-source parameters such as overburden velocity and working point velocity. This raises something of a dilemma, in that one must either place great confidence in what appear to be very unusual stations that may be subject to a subtle propagation bias, or one must accept the diminished resolution offered by the more robust event-averaging results. In both cases the spectra indicate a relative increase in the high frequency content of direct *P* compared to *P* coda for increasing average overburden velocity (and depth), but the apparent significance of this is influenced by choice of stations and analysis procedure. Murphy and O'Donnel (1987) scaled NTS event-averaged *P* and *P* coda spectra to a common yield of 150 kt, and then computed the ratio, finding a slightly negative *PIP* coda slope. Their result is consistent with the slightly negative average value of all slopes in Figure 7. Their processing made no corrections for source-parameter dependence of the ratios in the scaling to a common yield. The weak near-source sensitivity of the *PIP* coda slopes will be discussed further below.

The baseline shift of the spectral ratios in Figure 5 for different magnitude events suggests that single frequency *PIP* coda ratios may have systematic behavior with source parameters. This is explored further in Figure 8, where the spectral ratio of event-averaged spectra at two different frequencies are compared with $m_b(ab)$, depth, average overburden

velocity and working point velocity. These comparisons result in more systematic behavior than the spectral slope results. At a frequency of 0.469 Hz, the P/P coda ratios increase quite regularly with magnitude, depth, and overburden velocity. Poorer correlation is found with working point velocity. The Yucca Flat data alone do not define a trend, but the Pahute Mesa data do show systematic variation, so this does not appear to be just a subsite effect. At frequencies from 0.78 to 1.0 Hz, similar comparisons have reduced trends, or even strongly opposite trends, as shown in Figure 8. This appears to be directly the result of pP scalloping moving into the passband for the larger, more deeply buried events, causing a rapid reduction in the P spectral levels.

This pP interference interpretation is supported by Figure 9, which summarizes the slope determinations for comparisons of P/P coda ratios at each frequency with depth, $m_b(ab)$ and average overburden velocity. The influence of these parameters is difficult to separate because they all show very similar variations with frequency, with the strong reversal in trend corresponding well with the expected pP effect. It seems likely that depth is the dominant factor, given its more extreme variations and clear physical link to the pP induced trend. This frequency-dependent variation of the relative energy flux in the direct signal and the early coda was characterized by very different time-domain measures by Lay (1987) and Lynnes and Lay (1988a), and appears to be a robust feature of the data set. Peaking of the spectrum near 0.5 Hz, with a corresponding minimum at 1.0 Hz is expected if the low frequency pP behavior has a strong (-1.0) reflection coefficient and a delay time of about 1 sec, which is near the largest delay expected for NTS events. Thus, these trends may be attributed to a systematic shift with source depth of a strong free surface interaction. This explanation is somewhat at odds with the absence of stronger pP scalloping, particularly at high frequencies. Thus, a frequency dependent pP effect, or some additional factor is suggested. An obvious concern is that the low frequency behavior simply reflects a noise-level saturation, as will be discussed later.

Results for the Novaya Zemlya Test Site

Application of the P/P coda analysis to a foreign test site must proceed with very little knowledge of the actual near-source properties. In addition, our data set for Novaya Zemlya is relatively limited, and data for the two subsites (11 events at the northern subsite and 3 events at the southern subsite) on the island had to be merged to provide enough sampling for the event-averaging procedure to be applied. Burger et al. (1986) have reported systematic waveform variations between the northern and southern subsites, but we proceed under the assumption that the heavy averaging in the processing provides

reliable average source spectra. This is supported by the large total number of stations (90) that contribute data due to the favorable network distribution. The signals are also not as band-limited as for NTS events due to the lower level of near-source attenuation.

Examples of event-averaged P and pP coda spectra for two Novaya Zemlya events are shown in Figure 10. While the lowest frequency point is again unstable due to noise levels, it is clear that the spectra have even less pronounced pP scalloping than the NTS data (Figures 5 and 6). This is an interesting result, compatible with the results of P -wave averaging by Murphy and O'Donnell (1988). Other Soviet test sites also yield fairly smooth event-averaged P spectra: Murphy and O'Donnell (1987) found very little spectral scalloping in event-averaged spectra for Shagan River events and correspondingly low pP amplitude estimates. Using a multi-channel deconvolution method that emphasizes the common high frequency source radiation, Chan et al. (1988) find much stronger pP amplitudes for Novaya Zemlya events than implied by Figure 10. This is partially due to very short pP delay times, of only 0.2-0.6 sec, estimated by deconvolution. These short delays shift any scalloping to higher frequencies than for NTS events. Delay times less than 0.4 sec will produce scalloping outside of our frequency passband. Application of the same deconvolution algorithm to NTS events indicates very complex free surface interactions for Pahute Mesa events, with weak pP arrivals (Der et al., 1987a,b). Burger et al. (1986) also find strong pP amplitudes for Novaya Zemlya events using a waveform inversion procedure that emphasizes the lower frequency content, and their pP delay time estimates of 0.55-0.74 sec tend to be 0.3-0.4 sec longer than those for the same events estimated by deconvolution (Chan et al., 1988).

The modest spectral scalloping between 1.5 and 1.8 Hz in Figure 10 is quite consistent with the pP delay time estimates for these two events from Burger et al. (1986): 0.64 sec for October 14, 1969 (predicted spectral null at 1.56 Hz), and 0.58 sec for November 2, 1974 (predicted null at 1.72 Hz). For comparison, Chan et al. (1986) estimate delay times of 0.35 sec and 0.62 sec respectively for these two events. Frequency-dependence of the pP reflection and multiple arrivals caused by spallation of the free-surface are likely to be the cause of differences in pP parameter estimation for different methodologies (Lay, 1991). The shorter pP lag estimates are likely to give more accurate indications of source depth. The very short delay times estimated by Chan et al. (1988) indicate unusually shallow burial depths at Novaya Zemlya, particularly for events at the northern subsite, with less variation than expected based on normal yield-scaling for the observed magnitude range.

The spectral ratio slopes in Figure 10 show a systematic decrease in slope with increasing magnitude, and somewhat higher spectral ratio levels for the larger events. The

slope estimates for all 14 events are compared with $m_b(ab)$, explosion source strength, pP lag time, and pP/P absolute amplitude ratio in Figure 11. The latter three measures are obtained by waveform intercorrelation processing of the signals by Burger et al. (1986). These pP parameters should be interpreted as 'apparent' pP parameters for the lower frequency component of the signal, which corresponds to our frequency band. There is no independent information about average overburden velocity or other detailed near-source parameters for this test site. There is evidence that the majority of events are buried at relatively shallow depths, and that the region has higher velocity source rocks than the NTS area (e.g. Burger et al. 1986; Chan et al., 1988).

The P/P coda spectral ratio slopes for Novaya Zemlya show a systematic decrease with increasing magnitude, and to the degree that the estimates of apparent pP lag times reflect actual burial depth variations, there is a corresponding variation with depth. The variation of P/P coda slope for estimates of explosion source strength is similar to that for magnitude, as expected. The relative pP amplitude estimates also show a systematic variation, but note the high pP amplitudes from the intercorrelation procedure of Burger et al. (1986). These values appear to be influenced by a more complex process than a simple free-surface reflection, and qualitatively can be interpreted as a mapping of the combined pP and spallation effects into a single arrival. Given the apparently shallow burial depths and possible departure from normal yield-scaling of burial depth, it is likely that the intercorrelation results reflect more of a spallation volume contribution rather than a true burial depth effect. While the precise interference effect is not known, and appears to be complicated judging from the results of deconvolution analysis (Chan et al. 1988), it is clear that there is a systematic differential effect on the P and pP coda spectra. The trends are all significantly different than any found for NTS events, showing that there are fundamental differences in the energy flux partitioning between the test sites (see also Lay and Welc, 1987; Lay, 1987; Gupta et al., 1989).

The P/P coda ratios for Novaya Zemlya are not significantly different than for NTS events, even allowing for a 0.3 magnitude unit shift between the sites. This is not inconsistent with the analysis by Lay and Welc (1987), which reported lower complexity measures for Novaya Zemlya events, as characterized by energy centroid times, because the differences they observe are mainly accumulated in the first 5 sec of the waveform, during which the Novaya Zemlya data are more impulsive than comparable magnitude NTS events. Murphy and O'Donnell (1987) find that absolute ratios of P/P coda are higher for yield-scaled events at Shagan River than at NTS, but any such trend in our data is at best subtle. However, we do find that for frequencies less than 1.0 Hz the P/P coda single frequency ratios increase systematically with magnitude, as is true for the low frequency

spectral ratios for NTS events (Figure 8). Regressions were performed on magnitude for the ratios at each frequency, with the results being summarized in Figure 12. The ratios have positive slopes and high correlation coefficients up until about 1 Hz, with higher frequencies sometimes having negative slopes and correlations, but with more sporadic behavior. Very similar trends are found in comparison with the apparent pP delay time and relative amplitude estimates.

Discussion

This empirical analysis of the spectral content of direct P -waves and early P -wave coda from underground nuclear explosions at the NTS and Novaya Zemlya test sites demonstrates that there is some sensitivity to near-source properties in the differential behavior of teleseismic P and P coda. The application of spectral-factoring to combine spectra from a global set of stations has somewhat degraded the apparent sensitivity to overburden velocity suggested by a few isolated stations for NTS events. This casts doubt on our ability to remotely constrain overburden velocity by spectra from either networks or single stations if we are lacking extensive calibration data. The processes that shape the spectra at different stations may have such high variability that only a few isolated stations have favorable behavior, or alternatively those stations may erroneously indicate greater near-source influence than actually exists.

The general tendency that is found for NTS events is for events with higher average overburden velocities to have relative enrichment of high-frequency P spectral content, which is consistent with near-field observations for constant yield events in varying media, as discussed by Gupta and Blandford (1987). The differential behavior of the P coda may be attributed to the shallower origin of much of the energy that arrives in the coda, as a result of near-surface scattering and delayed surface-interaction arrivals. Gupta and Blandford (1987) question whether this can actually explain the large differences they observed at NORSAR, but perhaps those particular phases are enhanced by path specific properties. The more subdued trends of the event-averaged spectra may be easier to explain, but this will still require quantitative three-dimensional modeling, which is beyond the scope of this paper. It is possible that inadequate signal-to-noise levels of the hand-digitized data have simply undermined the advantages of the spectral averaging process, so further P/P coda analysis of global digital array data is desirable. This paper does demonstrate that individual station behavior is strongly influenced by site-specific effects, thus the absolute value of isolated P/P coda spectral ratio slopes should not be interpreted as completely due to a near-source effect.

While our NTS data are generally supportive of the interpretations of Gupta and Blandford (1987), the Novaya Zemlya signal behavior appears to be different. Lack of independent knowledge of the relation between event size and overburden velocity at Novaya Zemlya handicaps our interpretation; however, the decrease of P/P coda spectral slope with magnitude probably cannot be fully explained by the mechanisms Gupta and Blandford (1987) proposed for NTS. It is generally believed that test site subsurface heterogeneity is stronger at NTS than at Novaya Zemlya, and that events at the northern Novaya Zemlya test site may depart from normal yield-scaled burial depths, so it is not likely that there is much overburden velocity variation for the latter events. Diminished variability in near-source overburden may account for some of the test site differences, but it appears that additional mechanisms affect the spectra.

The systematic behavior of the individual frequency P/P coda spectral ratios for the NTS events is evidence in favor of the reliability of our event-averaged spectra for establishing sensitivity to near-source properties. Noise level saturation at low frequencies is a possible contaminating factor, but probably should not result in such systematic trends. The complementary trends with increasing magnitude of increasing ratios at frequencies less than 0.5 Hz and decreasing ratios around 0.8 Hz are most readily interpreted as the effect of the free surface interaction. While it does not appear that the pP phase is a coherent, single arrival, both this spectral analysis and the time domain waveform analysis of Lay (1985), indicate that the low frequency direct P spectra have a strong 'effective' pP interference that varies systematically with burial depth. Constructive interference at the lower frequencies and destructive interference at the mid-frequencies should shift systematically through the frequency band as depth (and magnitude) varies. The differential effect on the ratios appears to stem from the averaging properties of the P coda. This frequency-dependent behavior is clearly what controls the pP parameter estimation procedures of intercorrelation (e.g. Lay, 1985; Burger et al., 1986) or model fitting of event-averaged spectra (e.g. Murphy, 1989). It can also account for the frequency-dependent shifts of energy centroids for different passbands (Lay, 1987). The possibility that the spectral ratio behavior is not entirely due to variation of the P spectra alone is raised by the fact that the Novaya Zemlya data also show the systematic increase with magnitude at low frequencies. Since these events are less deeply buried, and have shorter apparent pP delay times, it seems unlikely that spectral modulation from free surface interaction alone is responsible.

Another interpretation of the low frequency P/P coda ratio behavior, advanced by Lay (1987) and Lynnes and Lay (1988a) is that shallow events have enhanced low frequency coda levels due to a greater contribution of near-source surface-wave scattering into the

teleseismic coda. This interpretation can explain the strength of the low frequency P/P coda ratio trends with depth and magnitude in Figure 8 and 12, but such behavior alone cannot account for the negative average values of P/P coda ratio slopes for NTS (Figure 7), or the increase in slopes (to values near zero) with increasing magnitude and burial depth. Another problem with this interpretation is that P coda spectra appear to give better estimations of yield than corresponding P spectra, especially at low frequencies (Gupta et al., 1985). The Novaya Zemlya data do have a systematic decrease in P/P coda slope with increasing magnitude and apparent pP lag (Figure 11), which could result from enhanced low frequency coda for smaller (shallower?) events, but the slopes for the larger events are negative, which requires an additional effect. If the variation in burial depth is actually small, a volumetric influence, by which larger source volumes excite more high frequency energy in the coda (or a depletion of high frequency content of the direct P) must be invoked. These qualitative ideas can only be tested by extensive modeling, perhaps including non-linear surface interactions. The need for such modeling is suggested by the fact that the reduction of P/P coda slopes with magnitude for the Novaya Zemlya events could lead to erroneous interpretations of the near-source environment based on comparison with the NTS behavior. It may be that the differences between the sites are due to competing burial depth and overburden velocity influences on the spectra, or possibly non-spherical source radiation, or different coda generation mechanisms play a role. Until this is better understood it will be difficult to place any confidence in remotely determined near-source properties.

Conclusions

A large data set of teleseismic short-period P wave seismograms from underground nuclear explosions has been examined to test whether the differential spectral content of P and early P coda is sensitive to near-source properties. Application of a spectral factoring procedure designed to remove receiver and propagation spectral factors results in stable event-averaged spectra for P and P coda. The slopes of P/P coda spectral ratios show a slight sensitivity to overburden velocity, burial depth relative to the water table, and working point velocity for NTS events, with events in higher velocity rock having relatively enhanced high frequency P spectra. The Novaya Zemlya events show a different trend, with larger events having relatively decreased P spectral content. These test site specific patterns are difficult to reconcile with any single near-source influence. All of the events show a tendency for P/P coda spectral levels to increase with magnitude at frequencies around 0.5 Hz, and to decrease at higher frequencies (near 0.8 Hz for NTS,

1.6 Hz for Novaya Zemlya). The latter behavior is most reasonably attributed to interference effects with free surface phases that preferentially affect the *P* spectra. However; systematic frequency-dependent variations of the *P* coda spectra may also play a role in these patterns. Quantification of the observed behavior is required before there is any hope of reliably remotely characterizing near-source environment for isolated tests.

Acknowledgements

We thank Jerry Carter, Chris Lynnes and Indra Gupta for their assistance in accessing information about NTS source properties. This research was supported by the W. M. Keck Foundation and the Defense Advanced Research Projects Agency and was monitored by the Phillips Laboratory under Contract F19628-89-K-0011. This is contribution number 125 of the Institute of Tectonics and the C.F. Richter Seismological Laboratory.

References

- Bullitt, J. T. and V. F. Cormier (1984). The relative performance of m_b and alternative measures of elastic energy in estimating source size and explosion yield, *Bull. Seism. Soc. Am.*, **74**, 1863-1882.
- Burger, R. W., T. Lay, and L. J. Burdick (1986). Estimating the relative yields of the Novaya Zemlya tests by waveform intercorrelation, *Geophys. J. R. Ast. Soc.*, **87**, 775-800.
- Burger, R. W., T. Lay, C. G. Arvesen, and L. J. Burdick (1985). Estimating seismic yield, *pP* parameters and tectonic release characteristics at the Novaya Zemlya test site, *Technical Report, WCCP-R-85-03*, Woodward-Clyde Consultants, Pasadena, California.
- Chan, W. W., K. L. McLaughlin, R. K. Cessaro, M. E. Marshall, and A. C. Lees (1988). Yield estimation of Novaya Zemlya explosions from short-period body waves, *Technical Report, TGAL-88-03*, Teledyne Geotech Alexandria Laboratories, Virginia.
- Der, Z. A., A. C. Lees, W. W. Chan, R. H. Shumway, K. L. McLaughlin, E. Smart, T. W. McElfresh, and M. E. Marshall (1987a). Maximum-likelihood multichannel deconvolution of *P* waves at seismic arrays, *Technical Report, TGAL-87-3*, Teledyne Geotech Alexandria Laboratories, Virginia.
- Der, Z. A., R. H. Shumway, and A. C. Lees (1987b). Multi-channel deconvolution of *P* waves at seismic arrays, *Bull. Seism. Soc. Am.*, **77**, 195-211.
- Gupta, I. N. and R. R. Blandford (1987). A study of *P* waves from Nevada test site explosions: near-source information from teleseismic observations? *Bull. Seism. Soc. Am.*, **77**, 1041-1056.
- Gupta, I. N., R. R. Blandford, R. A. Wagner, and J. A. Burnett (1985). Use of *P* coda for explosion medium and improved yield determination, in *The VELA Program*, Ed. A. U. Kerr, Executive Graphics Services, Washington, D. C., pp. 711-720.

- Gupta, I. N., C. S. Lynnes, R. S. Jih, and R. A. Wagner (1989). A study of teleseismic P and P coda from U.S. and Soviet nuclear explosions, *Proceedings 11th annual DARPA/AFGL Seismic Research Symposium*, Air Force Geophysics Lab, Hanscom AFB, Massachusetts, pp 389-399.
- Lay, T. (1985). Estimating explosion yield by analytical waveform comparison, *Geophys. J. R. astr. Soc.*, **82**, 1-31.
- Lay, T. (1987). Analysis of near-source contributions to early P-wave coda for underground explosions. II. Frequency dependence, *Bull. Seism. Soc. Am.*, **77**, 1252-1273.
- Lay, T. (1991). The teleseismic manifestation of pP: Problems and paradoxes, AGU Monograph on Explosion Phenomenology, in press.
- Lay, T. and D. V. Helmberger (1983). Body-wave amplitude and travel-time correlations across North America, *Bull. Seism. Soc. Am.*, **73**, 1063-1076.
- Lay, T. and J. L. Welc (1987). Analysis of near-source contributions to early P-wave coda for underground explosions. I. Waveform complexity, *Bull. Seism. Soc. Am.*, **77**, 1017-1040.
- Lynnes, C. S. and T. Lay (1988a). Observations of teleseismic P wave coda for underground explosions, *PAGEOPH*, **128**, 231-249.
- Lynnes, C. S. and T. Lay (1988b). Analysis of amplitude and travel-time anomalies for short-period P-waves from NTS explosions, *Geophys. J.*, **92**, 431-443.
- Mueller, R. A. and J. R. Murphy (1971). Seismic characteristics of underground nuclear detonations. Part I. Seismic spectrum scaling, *Bull. Seism. Soc. Am.*, **61**, 1675-1692.
- Murphy, J. R. (1989). Network-averaged teleseismic P-wave spectra for underground explosions. Part II. Source characteristics of Pahutē Mesa-explosions, *Bull. Seism. Soc. Am.*, **79**, 156-171.
- Murphy, J. R., B. W. Barker, and A. O'Donnell (1989). Network-averaged teleseismic P-wave spectra for underground explosions. Part I. Definitions and examples, *Bull. Seism. Soc. Am.*, **79**, 141-155.
- Nakanishi, I. (1979). Attenuation of multiple ScS waves beneath the Japanese arc, *Phys. Earth Planet. Int.*, **19**, 337-347.
- Veith, K. F. and G. E. Clawson (1972). Magnitude from short-period P-wave data, *Bull. Seism. Soc. Am.*, **62**, 435-452.
- Wickens, A. J. and G. G. R. Buchbinder (1980). S-wave residuals in Canada, *Bull. Seism. Soc. Am.*, **70**, 809-822.

Table 1
OVERBURDEN VELOCITY DEPENDENCE OF P/PCODA SLOPE
FOR THE STATIONS WITH MORE THAN 35 OBSERVATIONS

STATION	POSITION	DIS- TANCE	AZIMUTH	NUMBER OF OBSER- VATION	CORRE- LATION COEFFI- CIENT	SLOPE VERSUS OVER- BURDEN
ARE	Peru	68	133	44	0.637	0.281
KON	Norway	74	25	36	0.592	0.168
STJ	Newfoundland	47	56	39	0.177	0.167
GDH	Greenland	46	26	40	0.207	0.107
ATL	Georgia	26	88	40	0.402	0.104
TOL	Spain	81	46	42	0.403	0.089
KTG	Greenland	57	24	43	0.291	0.083
UME	Sweden	74	19	44	0.334	0.047
SHK	Japan	84	309	48	0.172	0.047
TRN	Trinidad	56	104	42	0.301	0.044
NUR	Finland	78	19	53	0.341	0.040
STU	Germany	82	33	42	0.227	0.034
MAT	Japan	80	308	44	0.000	0.026
CAR	Venezuela	51	108	47	0.032	0.006
COL	Alaska	34	336	40	-0.012	-0.008
KIP	Hawaii	40	259	43	-0.280	-0.141

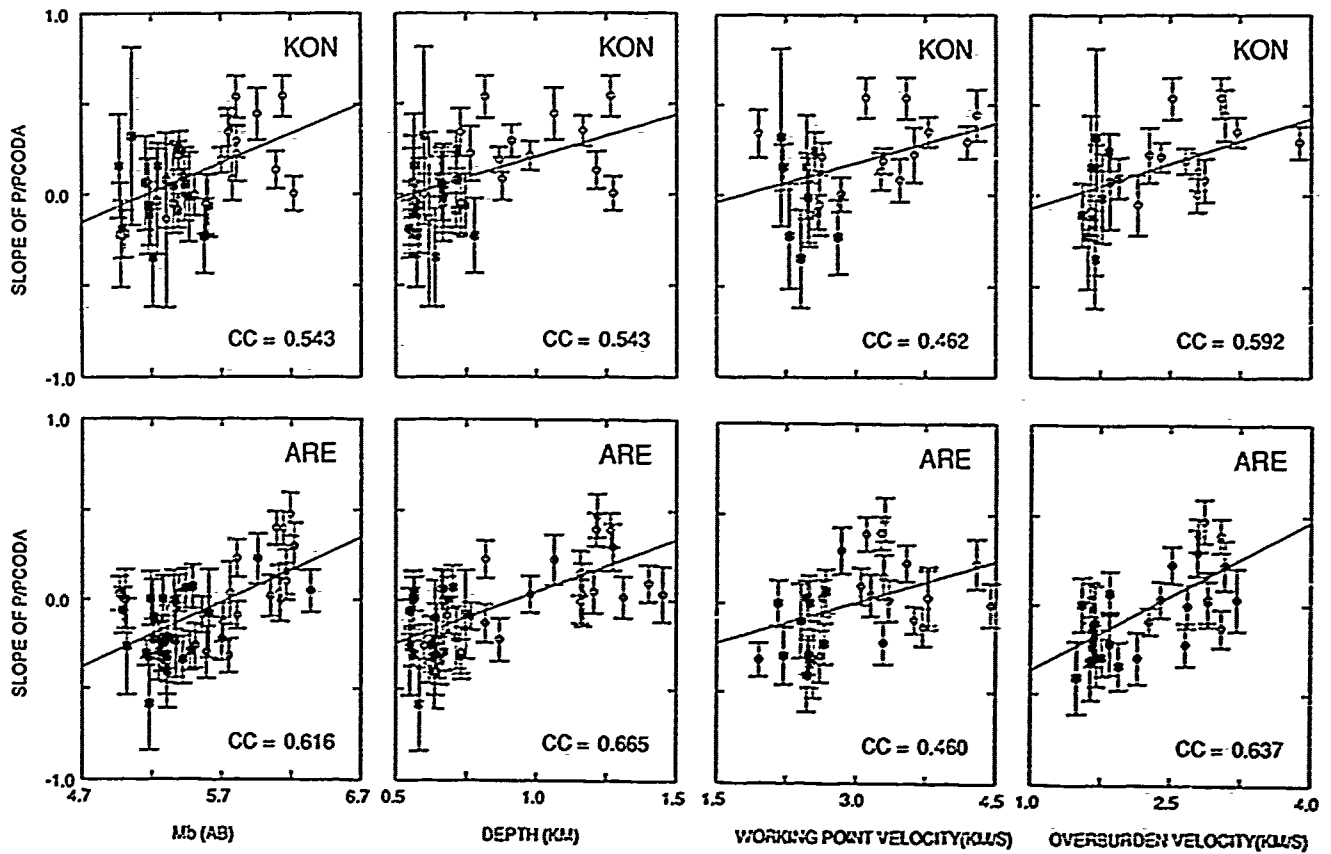


Figure 1. The slope of the spectral ratio of *P/P* coda is plotted as a function of first-cycle m_b (ab) magnitude, burial depth, working point velocity and average overburden velocity for WWSSN stations KON (top row) and ARE (bottom row) for NTS explosions. The correlation coefficient for each comparison is shown. These results are qualitatively consistent with those of Gupta and Blandford (1987) with the spectral ratio slopes increasing with increasing overburden velocity.

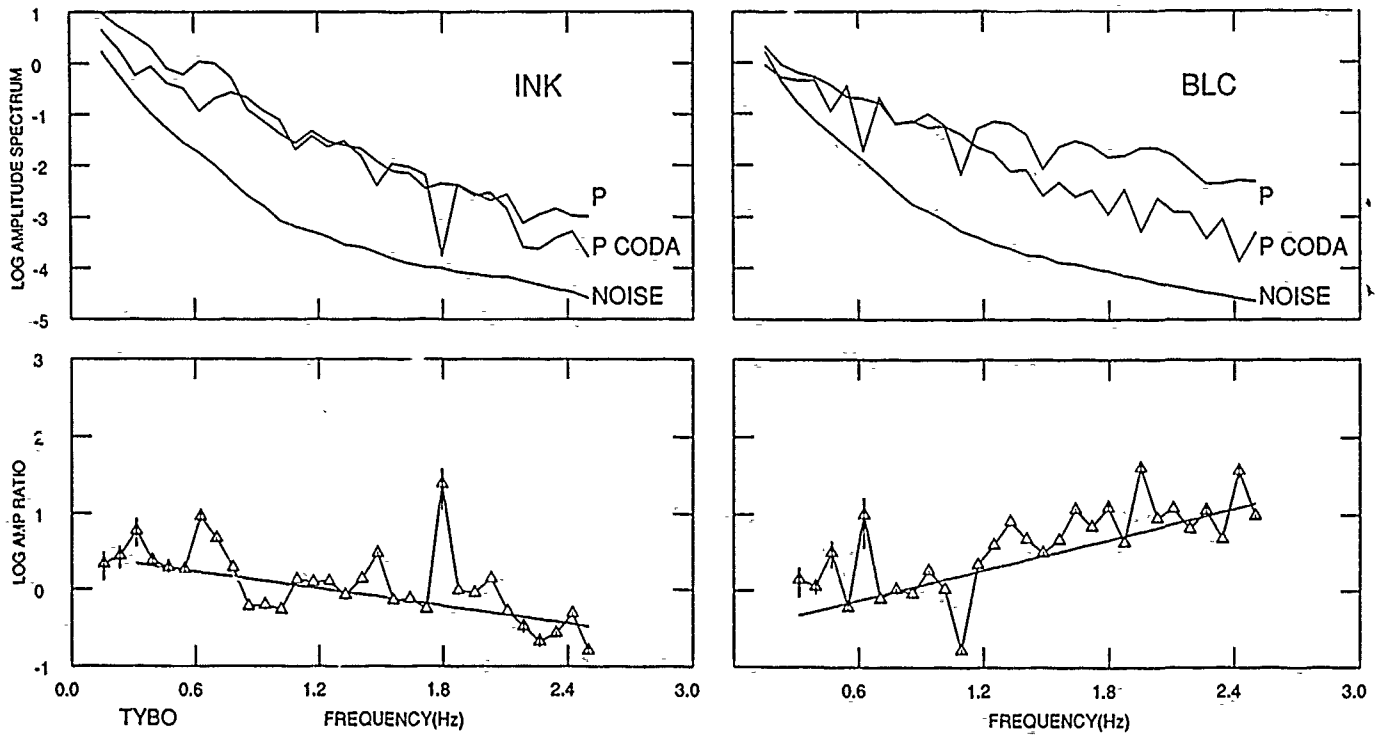


Figure 2. Comparison of the *P* and *P* coda amplitude spectra for two CSN stations, INK (left) and BLC (right) that recorded the Pahute Mesa explosion TYBO. The top figures show the signal amplitude spectra as well as smoothed noise spectra, while the lower figures show the logarithm of the *P/P* coda spectral ratios, with a signal-to-noise weighted linear regression curve. Note that the two stations have significantly different spectral ratios, characterized by the regression slopes, for the same event.

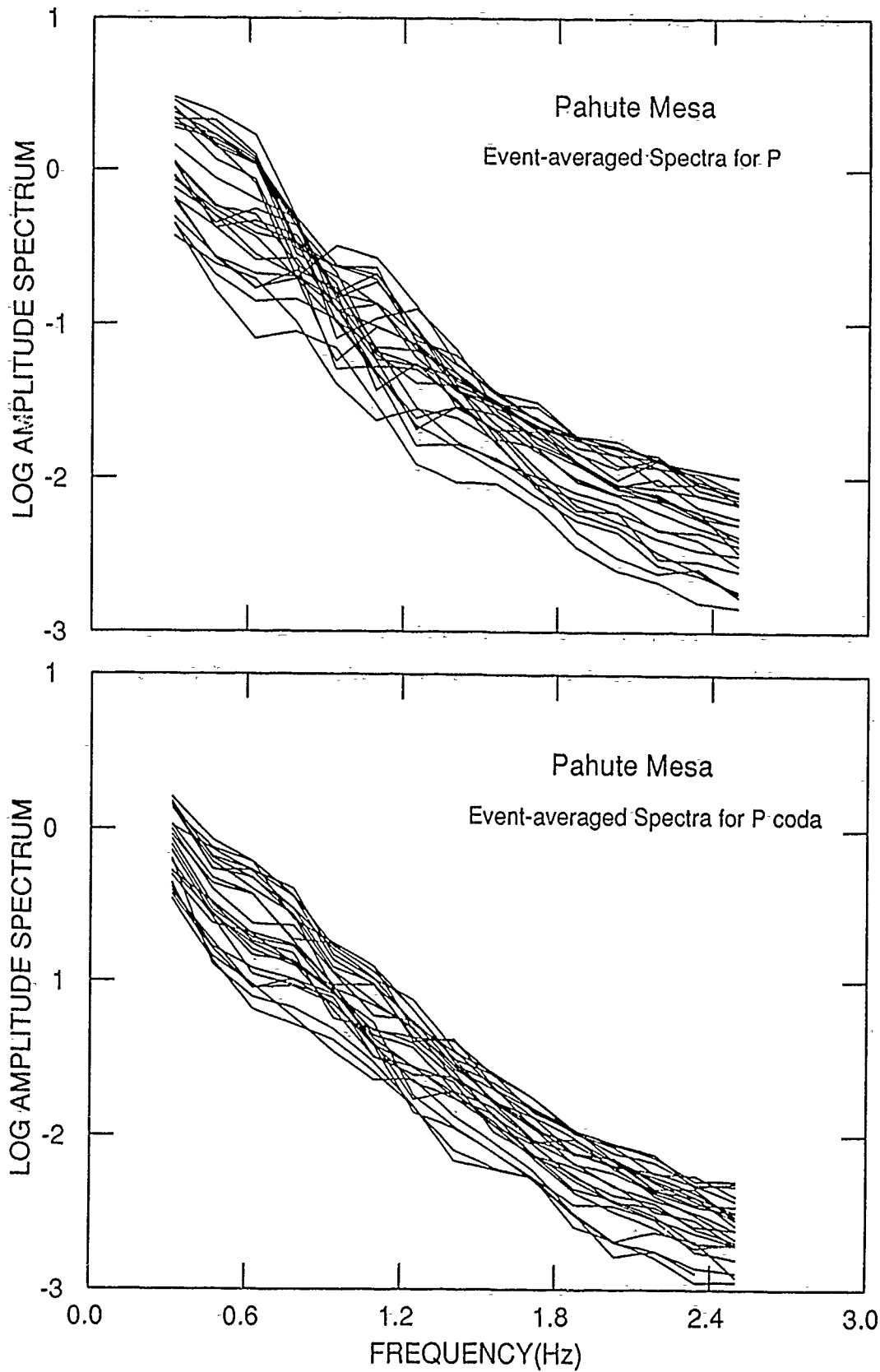


Figure 3. Event-averaged source spectra for 25 Pahute Mesa explosions for the direct P signals (top) and the early coda signals (bottom). The P spectra show scalloping near 1 Hz associated with pP interference that is missing from the P coda spectra. The pP interference varies with source depth, thus the scalloping shifts to higher frequencies for the smaller events.

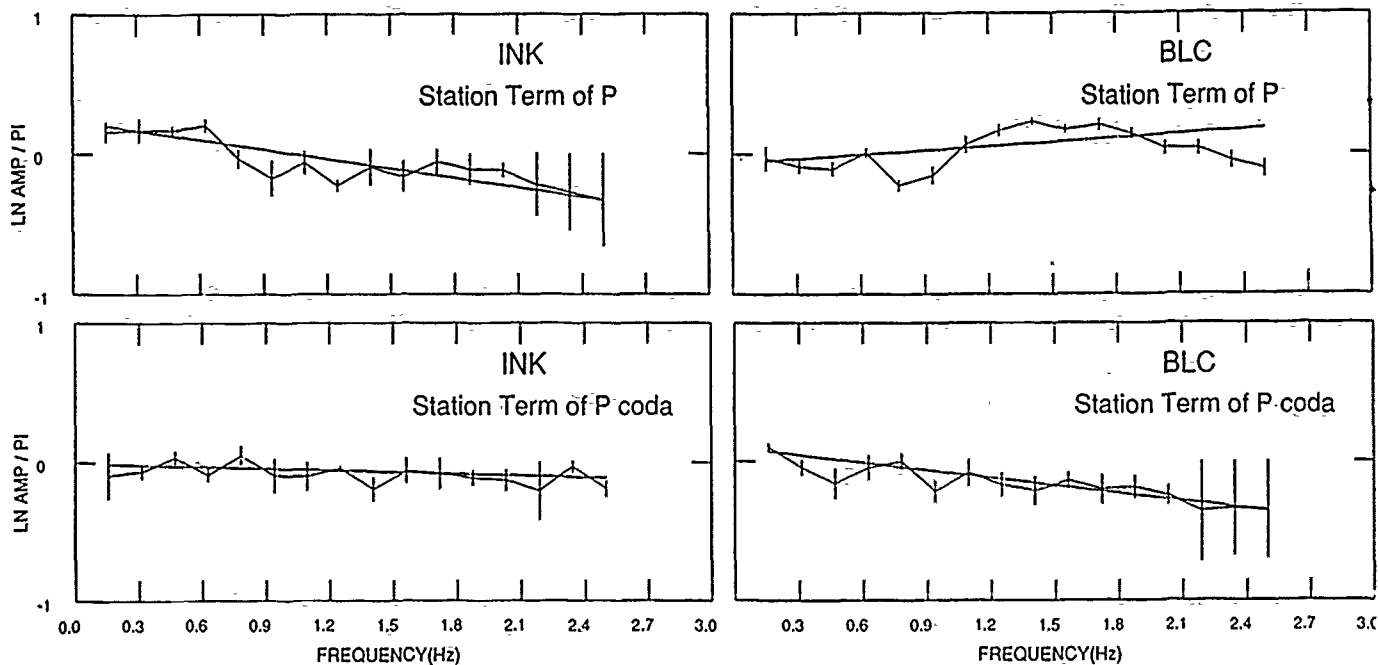


Figure 4. Event-averaged receiver terms for the two CSN stations from Figure 2 for the 25 Pahute Mesa explosions. The *P* and *P* coda station spectra are shown with vertical bars indicating the standard deviation of the spectral estimate at each frequency and a variance-weighted linear regression curve is superimposed. The spectra are plotted such that the slope of the curve is proportional to the differential attenuation from the mean value for the entire suite of stations for the corresponding phase. The relative differences in slope for *P* and *P* coda at the two stations account for the differences in the spectral ratio slopes shown in Figure 2, demonstrating the need for the spectral factoring procedure.

PAHUTE MESA EVENT-AVERAGED SPECTRA

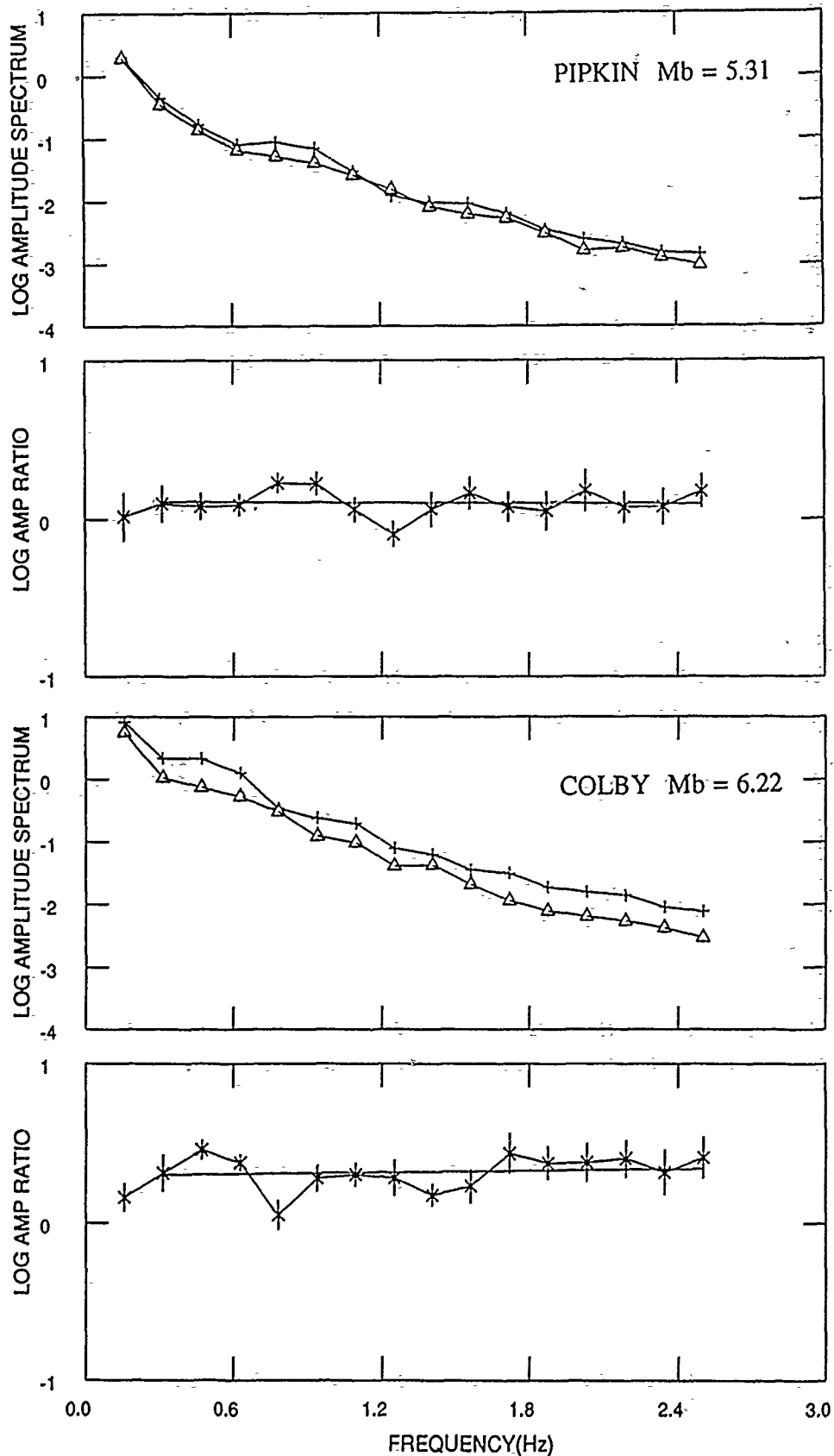


Figure 5. Two examples of event-averaged P (crosses) and P coda (triangles) spectra and associated spectral ratios (x's) for Pahute Mesa events. The P spectra show clear evidence of a shift in pP -scalloping to lower frequency with increasing magnitude (and hence increasing burial depth). However, the slopes of the spectral ratios are only slightly different, with the larger event having a slightly more positive slope. Note that the absolute amplitude ratios do increase systematically with increasing event size for frequencies removed from the spectral ratio minima caused by pP .

YUCCA FLAT EVENT-AVERAGED SPECTRA

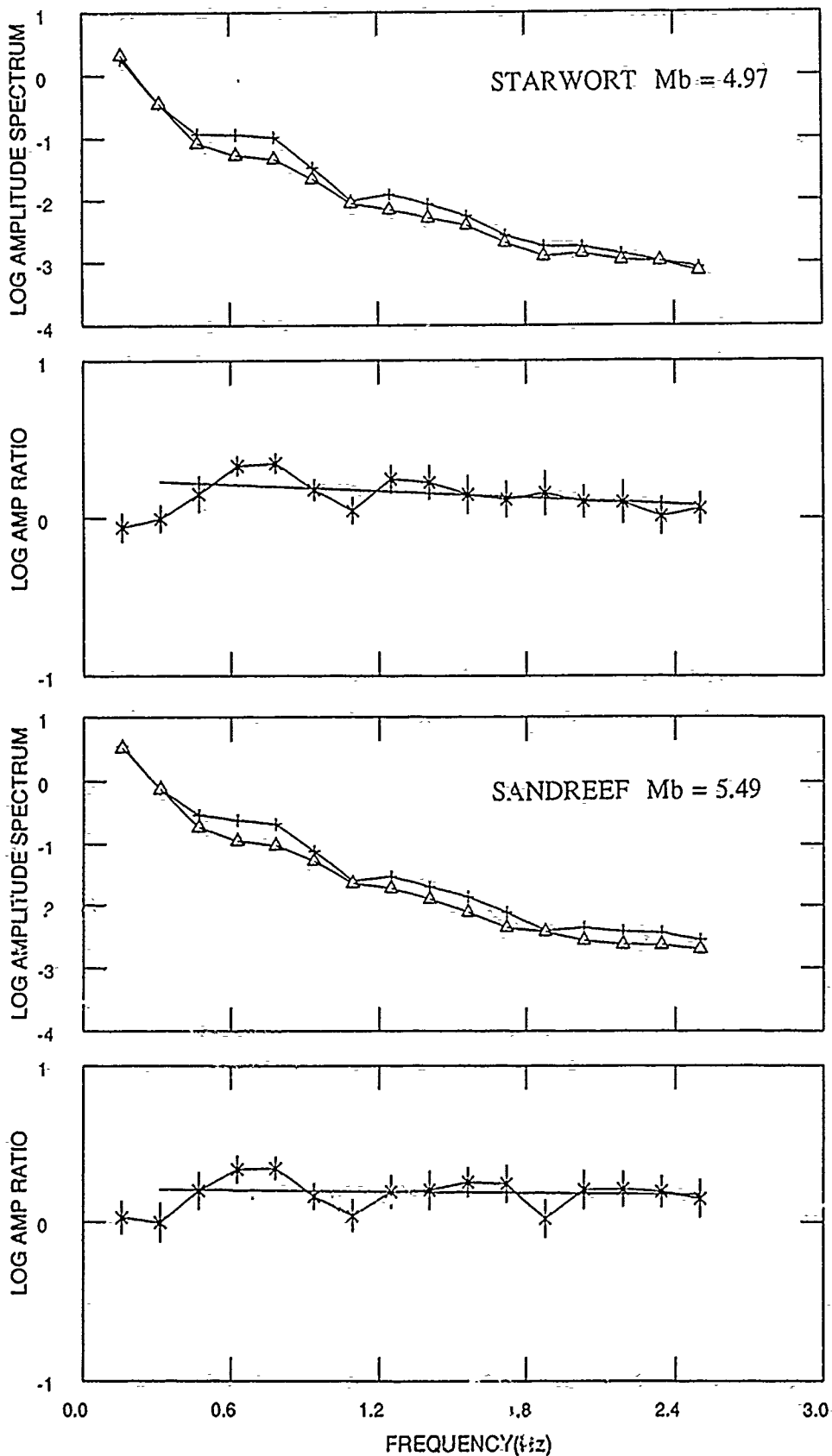


Figure 6. Results similar to those in Figure 5, but for two Yucca Flat events. The *P* spectra again exhibit greater modulation than the *P* coda spectra, with the ratios emphasizing the *pP* effect near 1.0 Hz. The Yucca Flat events only span a magnitude range of about 0.5 magnitude units, but little in the way of a magnitude-dependent variation in the spectral ratio slopes is indicated.

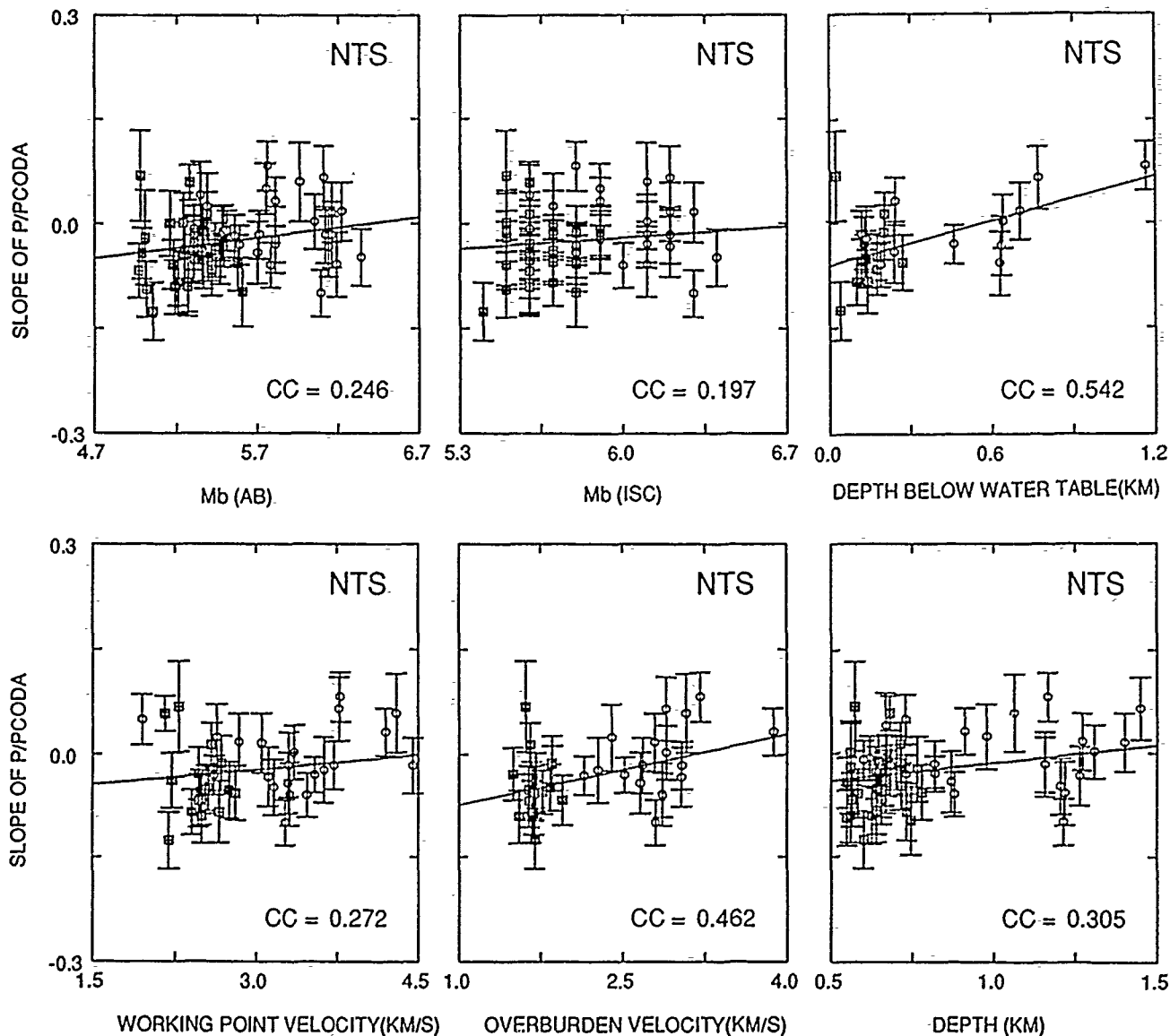


Figure 7. A summary of correlations for NTS event-averaged *PIP* coda spectral ratio slopes as functions of known source properties. The correlation coefficient for each comparison is indicated. The error bars on the slopes indicate the formal uncertainty in the signal/noise weighted regressions. Yucca Flat events are indicated with squares and Pahute Mesa events with circles. The spectral ratios show some increase in slope with increasing overburden velocity as well as with distance from the water table. The other comparisons suggest a slight increase in slope with increasing size and burial depth. The correlation with overburden velocity has the same sign as the single station analysis of Gupta and Blandford (1987) and Figure 1, but the trend is weaker.

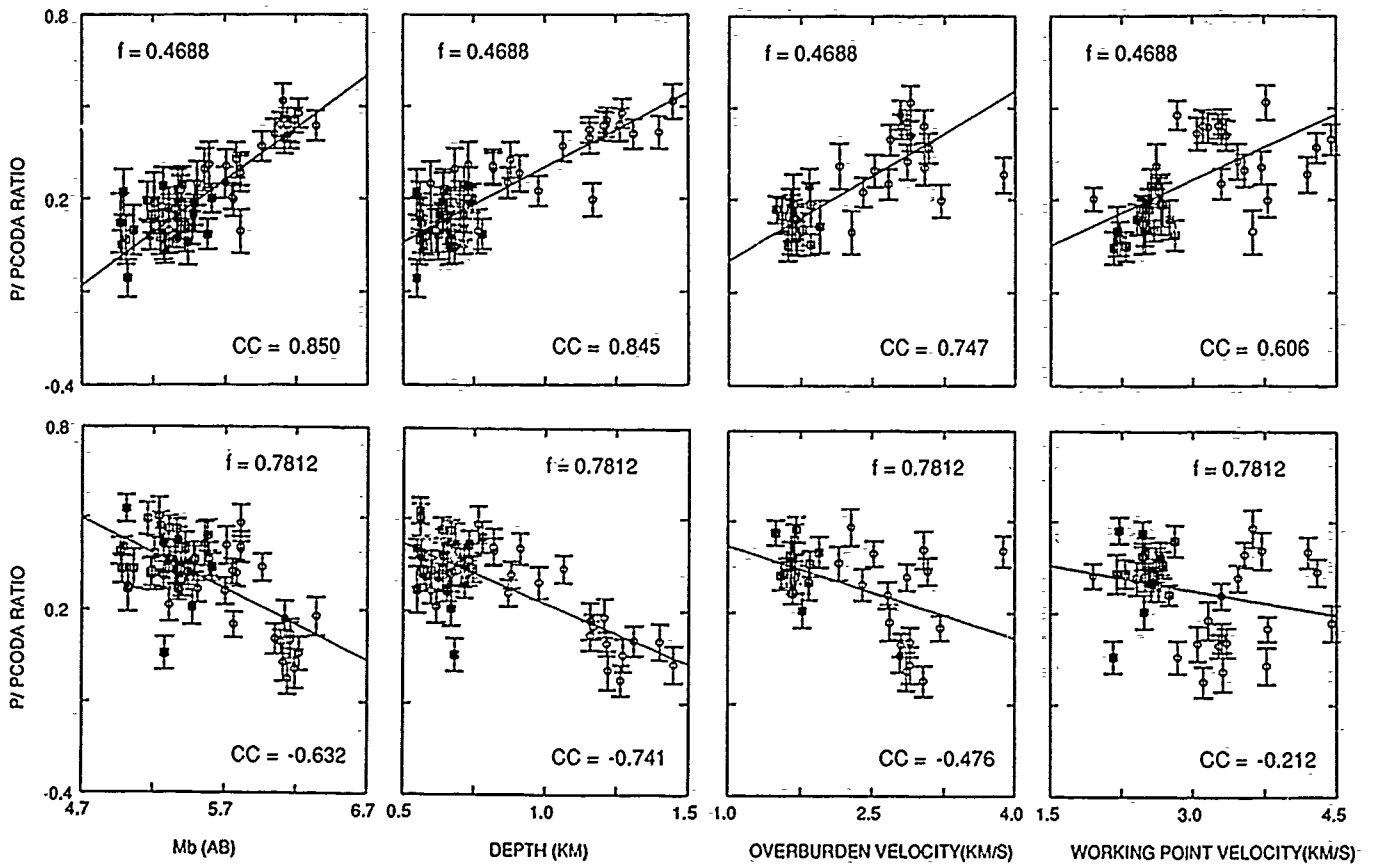


Figure 8. Variation of single frequency *PIP* coda spectral ratios for NTS events with source properties for frequencies of 0.4688 Hz (top row) and 0.7812 Hz (bottom row). Fairly systematic increases are observed at the lower frequency, with deeper, larger events having enhanced ratios. The higher frequency values show a reduction of the ratio attributable to interference with the *pP* pulse which contaminates this spectral range for the larger events.

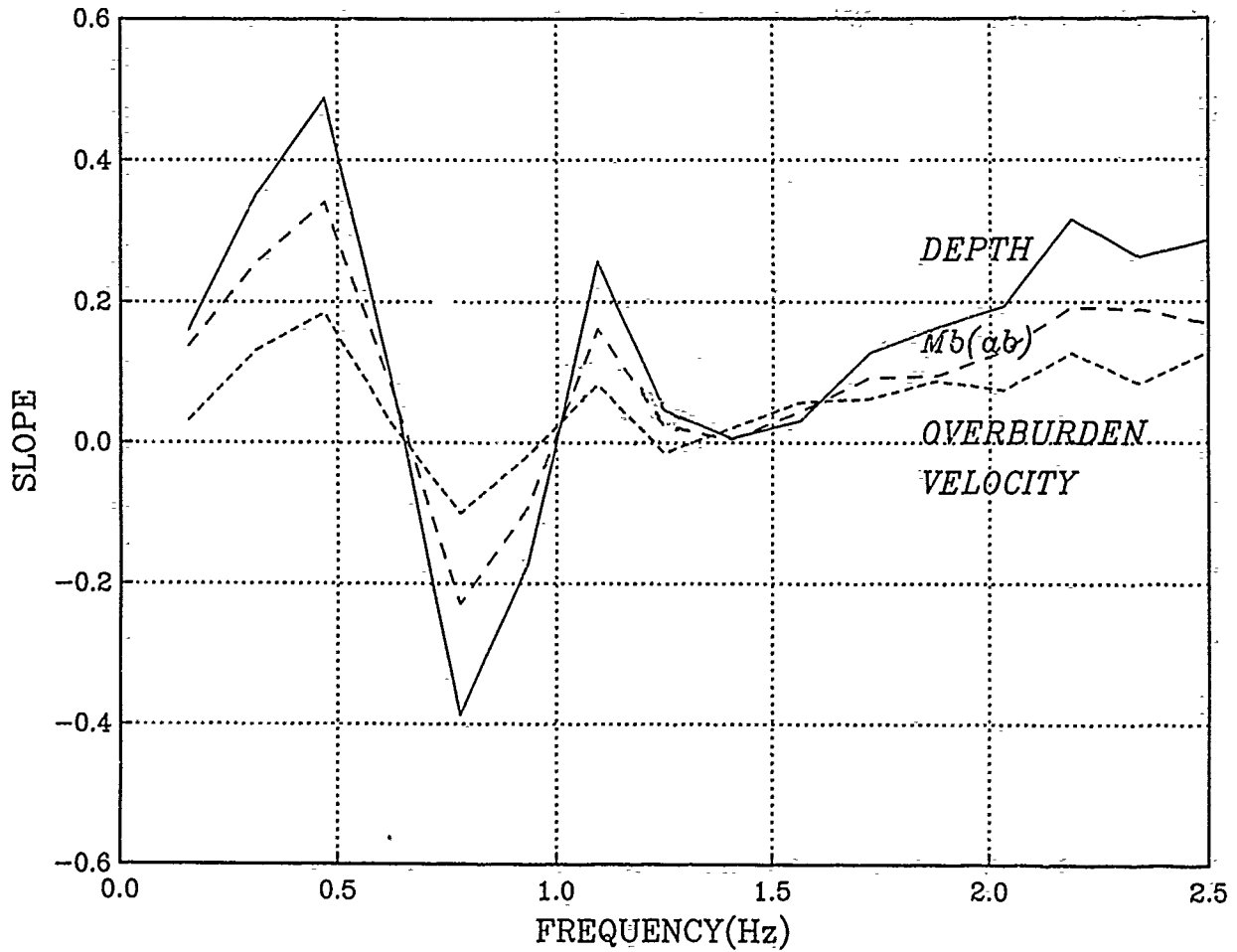


Figure 9. A summary plot of the slopes of individual frequency P/P coda spectral ratios versus depth, $m_b(ab)$ and overburden velocity for the NTS events. At each frequency, the spectral ratios were regressed on the associated source parameter, as in Figure 8. The reversal of slopes near 0.8 Hz is caused by the interference of pP in the P spectra for the larger events.

NOVAYA ZEMLYA EVENT-AVERAGED SPECTRA

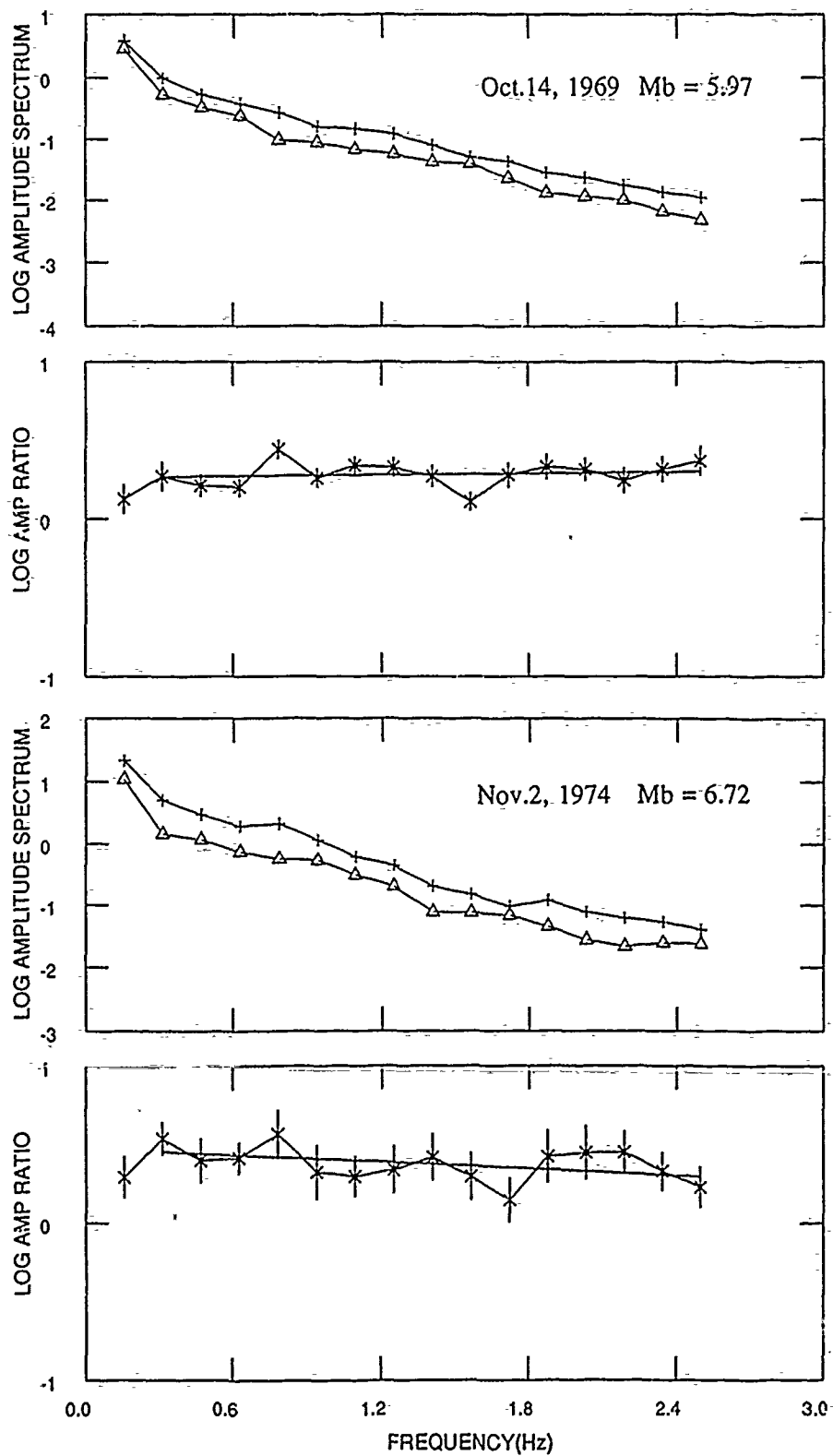


Figure 10. Results similar to those in Figures 5 and 6, but for two Novaya Zemlya events. The P spectra show very little modulation that can be attributed to pP , and the spectral ratios are relatively smooth. As for the Pahute Mesa events in Figure 5, the larger Novaya Zemlya events have larger spectral ratios. In addition, there is a tendency for the spectral ratio slopes to vary with magnitude, but the slope decreases rather than increases.

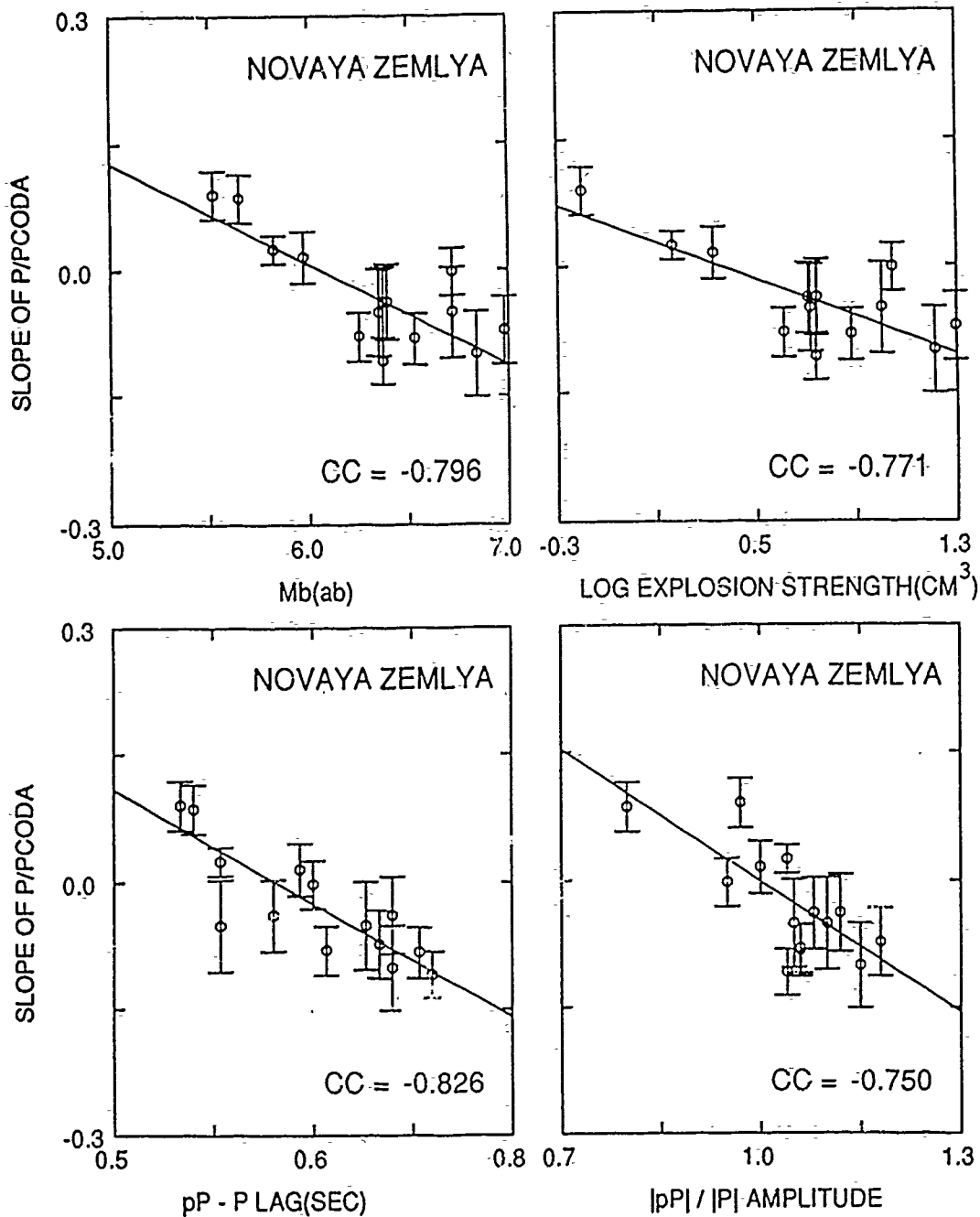


Figure 11. A summary of correlations for Novaya Zemlya test site event-averaged P/P coda spectral ratio slopes as functions of teleseismically measured event parameters from Burger et al., 1986. The correlation coefficient for each comparison is indicated. The ratios decrease systematically with increasing source size as measured by first-cycle magnitude ($m_b(ab)$) and $\log(\text{explosion strength})$ from waveform intercorrelation. There is also a systematic decrease with increasing apparent pP lag time and increasing apparent pP amplitude.

P/PCODA - MAGNITUDE

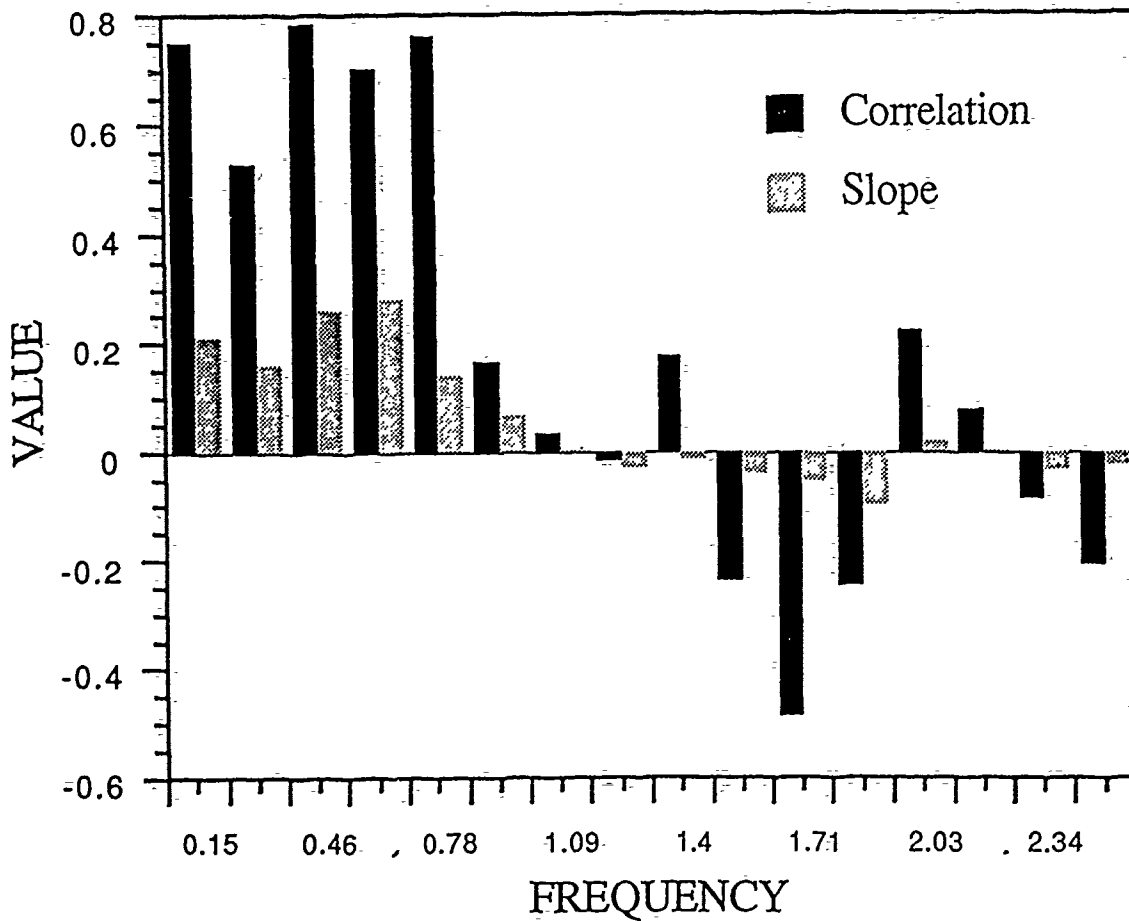


Figure 12. A summary of the slopes and correlations of individual frequency *PIP* coda spectral ratios versus $m_b(ab)$ for the Novaya Zemlya events. At each frequency, the spectral ratios were regressed on magnitude. The lower frequencies exhibit positive slopes with high correlation coefficients, indicating a systematic increase in *PIP* coda ratio with magnitude. The free-surface interference may eliminate this trend at frequencies above 1 Hz.

Chapter 2

The Teleseismic Manifestation of pP: Problems and Paradoxes

by

Thorne Lay

Abstract

Energy radiated upward from underground nuclear explosions has a complex interaction with the free surface that strongly influences the seismic wavefields recorded at teleseismic and regional distances. This interaction, differing from that for earthquakes primarily due to the much higher strains and strain rates involved, is essential to understand for both explosion yield estimation and event discrimination. Reflection of explosion P wave energy from the free surface, which produces the pP phase, involves frequency-dependent, non-linear processes that are intimately linked to surface spallation. Attempts to characterize the teleseismic pP arrival using a variety of time series analysis procedures have yielded seemingly inconsistent results, which can be attributed to a combination of limited bandwidth, neglected frequency dependence, and unresolved trade-offs with source time function, receiver and attenuation effects. Recovery of broadband ground displacement, now viable with modern instrumentation, is resulting in more robust characterizations of the pP and spallation arrivals; however, the intrinsic trade-offs with source parameters and attenuation remain. Numerical procedures to account for the non-linear interactions, surface topographic effects, and shallow crustal heterogeneity are enabling a more complete modeling of the free surface interaction.

INTRODUCTION

Seismic waves from underground nuclear explosions provide a basis for identifying and estimating the yield of such tests, critical components of nuclear treaty monitoring procedures, as well as for interrogating the deep interior structure of Earth. The characteristics of underground tests that are most distinctive relative to natural earthquakes are the shallow burial depths of explosions and the (ideally) spherical symmetry of the initial radiation from the source. The proximity to the surface and symmetry of radiation leads to strong interference effects between the downgoing P wave energy, and the compressional wave reflected off of the surface (pP), which arrives within a second afterward. The free surface reflection reverses the sense of motion of pP relative to P, producing destructive interference between these signals at longer wavelengths, which in turn provides many of the defining characteristics of seismic signals from explosions. It has thus been a long standing problem to fully characterize the pP reflection and its complexity.

Understanding the pP surface reflection from nuclear explosions requires consideration of seismic wave interaction with the free surface above the source. The upgoing compressional wave produced by an underground nuclear explosion can produce remarkable accelerations and ground velocities at the free surface. For example, the <5Mt explosion CANNIKIN produced surface vertical accelerations varying from 17 to 3.2 g at

horizontal ranges of 0.3 to 3.4 km from the shotpoint, and corresponding peak ground velocities of from 946 to 233 cm/s [Burdick et al., 1984b]. The initial compressional pulse of acceleration in these close-in recordings (Figure 1a) is followed by a ballistic interval characterized by -1 g acceleration that is terminated by high frequency pulses as the airborne material impacts (i.e. slapdown). This complex surface interaction involves a zone of spallation, in which rock failure occurs on surfaces at depth when the downgoing tensional stress wave resulting from reflection at the free surface (pP) exceeds the sum of the upward compressional stress, the lithostatic stress, and the tensile strength of the rock. Spallation is commonly observed [Springer, 1974], and may involve several discrete surfaces of parting at depth [Eisler et al., 1966].

The initial vertical peak ground velocities within the spall zone can actually be well explained by elastic theory [Burdick et al., 1985], which suggests significant rock strength under compression; however, the subsequent tensional spallation phenomenon clearly involves anelastic and nonlinear processes. At distances slightly beyond the spall zone, the surface vertical velocity recordings involve much smaller peak velocities, and the entire P waveform can be well-modeled using elastic wave propagation theory (Figure 1b). In these signals the major arrivals are the P wave turning below the source and the pP reflection from the free surface (the downward spike in the synthetic and observed waveforms in Figure 1b). For these records the pP reflection point is several kilometers horizontally from the shotpoint, and the distributed spall source does not appear to produce a coherent high frequency arrival, which allows the successful elastic modeling. At regional distances, there is evidence for corresponding pPn arrivals [Burdick et al., 1989], and it does appear that spall contributes to Pn and Lg phases [Taylor and Randall, 1989]. At teleseismic distances, the pP arrival will more directly sample the zone just above the shotpoint, where the downgoing pP will encounter the disturbed medium around the explosion cavity, and where spallation is most pronounced and can potentially constructively interfere to give coherent teleseismic arrivals.

The upgoing P energy from a nuclear explosion is partitioned into pP, pS, spallation and slapdown phases, as well as surface wave excitation and anelastic effects. The upgoing radiation itself may deviate from an isotropic wavefront if there is significant pre-stress in the vicinity of the source, or if an earthquake is triggered by the explosion; effects which are considered elsewhere in this issue. Understanding the pP phase is required for constraining the source depth, for appraising any bias on the body wave magnitude resulting from constructive or destructive interference, and for assessing how upgoing energy is partitioned in the seismic wavefield, which may reveal source region properties [Gupta and Blandford, 1987]. Systematic differences in pP delay times between source

regions may also provide a means for characterizing the source medium, which is critical for yield estimation. The question that thus arises is what is the teleseismic manifestation of pP? This article will review the seismological investigations of teleseismic pP for underground explosions to synthesize our understanding of this complex free surface interaction.

Throughout the following discussion of teleseismic investigations of the pP phase, it is useful to keep in mind the linear filter representation of a teleseismic signal spectrum:

$$U(\omega) = E(\omega) I(\omega) Q(\omega) G(\omega)$$

where ω is angular frequency, $U(\omega)$ is the far field P wave displacement spectrum, $E(\omega)$ is the far-field explosion source spectrum (generally assumed to not vary with take-off angle from the source, although departure from spherically symmetric radiation has sometimes been suggested), $I(\omega)$ is the instrument response, $Q(\omega)$ is the attenuation operator, and $G(\omega)$ is the total Earth propagation response. The Earth response for teleseismic signals is often approximated by:

$$G(\omega) = S(\omega) R(\omega)/r_0$$

where $S(\omega)$ is the source region transfer function, including the direct P arrival, pP, crustal reverberations near the source, and any secondary arrivals associated with spall; $R(\omega)$ is the receiver region transfer function including crustal reverberations beneath the receiver; and r_0 is a geometric spreading term. The transfer functions are expected to correspond to time domain spike trains for teleseismic distances, to the extent that crustal structure can be approximated by a set of horizontal layers. Of course, some distortion due to frequency dependent reflection coefficients accompanying non-linear effects or complex scattering structures may actually be required. It is critical to recognize the complete tradeoff that exists between the multiplicative filters. Any attempt to estimate $S(\omega)$ is subject to limitations in our knowledge of $E(\omega)$, $R(\omega)$ and $Q(\omega)$. All existing methodologies for estimating pP behavior, whether frequency domain or time domain, involve assumptions about one or more of these parameters, and much of the inconsistency in published pP characteristics reflects differing assumptions underlying, and sometimes obscured by, the processing.

LONG PERIOD CONSTRAINTS ON pP CHARACTERISTICS

There has been twenty years of extensive research on teleseismic P waves from underground explosions focused on quantifying the pP arrival, but unlike the situation for earthquakes, relatively little progress has been made by analyzing long period body waves. Usually, when considering long period body waves, simple assumptions about propagation effects are adequate to determine gross properties of the source. Ideally, a purely isotropic explosion should produce a teleseismic P wave comprised of only a direct

compressional P phase, and a slightly delayed dilatational pP phase. Given the shallow burial depths of all explosions, the time between pP and direct P, τ_0 , should be only 1 s or less, and at teleseismic distances the elastic pP surface reflection coefficient, α , should be close to -1.0. In this ideal case, we can assume $S(t) = \delta(t) + \alpha \delta(t - \tau_0)$. The destructive interference of these two arrivals should greatly reduce the amplitude and increase the dominant frequency content of the P waves recorded on long period instruments (10-15 s pendulum periods) relative to earthquake signals, which tend to have deeper sources and strong additional sP arrivals.

P arrivals on long-period WWSSN instruments for large explosions (Figure 2) are in fact very distinctive from P waves from earthquakes with comparable m_b . The explosion arrivals are low amplitude, resemble differentiated instrument responses, and are depleted in low frequency content relative to earthquake signals, which serves as the basis for discrimination procedures for large events [Molnar, 1971; Wyss et al., 1971; Hasegawa, 1972; Helmberger and Harkrider, 1972; Shumway and Blandford, 1978; Burdick and Helmberger, 1979; Burdick et al, 1984a]. In the frequency domain this is manifested as a peaking of the explosion P wave spectra at periods near 2-3 s for megaton size shots, with a rapid decrease in spectral levels at longer periods.

Peaking of the explosion spectra is readily explained by interference with a strong pP arrival, if we assume that the source time function (the time history of pressure applied on the source elastic radius) for long period radiation is essentially a step-function. If the pP arrival has an elastic reflection, the teleseismic P spectrum will be modulated by a factor of $(1 + \alpha^2 + 2\alpha \cos \omega \tau_0)^{1/2}$, where ω is angular frequency. For $\alpha = -1$, and $\tau_0 = 1.0$ s this modulation factor will have a maximum value at a period of about 2 s. For a step source time function, the far field spectrum (given by the derivative of the source time function convolved with the modulation term) is directly proportional to this modulating factor, and hence, proportional to ω at low frequencies. The spectrum is thus expected to drop off at long periods from the peak near 2 s, as is observed.

However, peaking of the teleseismic explosion P wave spectra may also be attributed to overshoot of the source time function, which requires the pressure on the boundary of the elastic zone surrounding the explosion cavity to be more impulsive than step-like [Molnar, 1971; Wyss et al., 1971; Müller, 1973]. Overshoot of the source function has been suggested in many studies of near-field and even teleseismic data, and cannot be dismissed as a possibility. This remains a fundamental trade-off between $S(\omega)$ and $E(\omega)$. Some progress has been made by combining body wave and surface wave constraints on the broadband source spectral content, but difficulties remain in independently determining overshoot of the source function [Lay et al., 1984]. It is likely that both overshoot and pP

interference contribute to the depletion of long period energy in teleseismic P waves. Regardless of the precise mechanisms for the drop off in long-period spectral levels, the net result is that most explosion P wave observations are made using high frequency instrumentation. Thus, the rest of this review will concentrate on pP results obtained using short-period and broadband seismograms.

HIGH FREQUENCY pP ANALYSIS PROCEDURES

This review of teleseismic short period P wave analyses is organized to roughly parallel the history of technique development and application. We will first consider procedures that utilize only the amplitude or power spectra, then time-domain waveform and differential waveform modeling procedures, and finally the variety of deconvolution techniques which are presently giving the most useful results. At their core, all methodologies exploit the spectral interference produced by multiple arrivals in the signal, but they vary widely with respect to assumptions about the source radiation, attenuation, and Earth transfer functions.

Power Spectrum Techniques

The underlying assumption for most amplitude or power spectrum procedures is that the pP and any other secondary arrivals are delayed, undistorted echos of the direct P arrival with relative arrival times and amplitudes to be determined. For the two arrival approximation described in the previous section, the displacement power spectrum will have the modulation factor $[1 + \alpha^2 + 2\alpha \cos(\omega\tau_0)]$, which for negative values of α (as expected for pP) predicts that spectral nulls will occur at frequencies of $f_n = n/\tau_0$, $n=0,1,2,3,\dots$, while positive values of α (as might be associated with slapdown) predict spectral nulls at frequencies $f_n = [(2n + 1)/2]/\tau_0$. Identification of spectral nulls and their frequency spacing is thus an obvious procedure by which to attempt to characterize the pP arrival.

For some events, such as CANNIKIN (Figure 3) the strong spectral scalloping can be well matched by a three arrival spike train, where the third spike has the same polarity as direct P and can be attributed to a slapdown arrival [Bakun and Johnson, 1973]. This modeling of the amplitude spectrum requires a parameterization of the source time function and attenuation filter. These spectra were fit with pP arrival values of α ranging from -0.4 to -0.71 and τ values from 1.12 to 1.18 s, and slapdown arrival values of α ranging from 0.67 to 0.85 with delays of 1.92 to 1.94 s. Time-domain comparisons based on the spectral fitting are shown on the right, indicating that omission of the phase spectra in the modeling has not led to significant loss of timing information. Note that the primary spectral scallop is well matched, but even the three source model provides a marginal fit to the higher frequency spectra. This, in part, stems from the simplified version of $S(t)$ used,

in which crustal reverberations near the source are ignored, as well as from ignoring receiver complexity.

An extension of the direct power spectral modeling technique that reduces the potential error from incorrect attenuation assumptions and unknown receiver complexity, involves ratioing the spectra from two nearby events recorded at a common station (Figure 4), and stacking the ratios from various stations to enhance the signal to noise ratio [King et al., 1972]. Assuming perfect cancellation of the attenuation, instrument, and receiver effects, the stacked ratios for events i and j give the following:

$$U_i(\omega)/U_j(\omega) = [E_i(\omega)S_i(\omega)]/[E_j(\omega)S_j(\omega)]$$

The ratios can then be modeled assuming spike trains for the two events simultaneously, with differences in the source functions explicitly being inverted for as well. The procedure clearly works best if the source functions and depths are very different, otherwise the information about each parameter is lost in the ratioing procedure. Any common attributes of the source such as overshoot tend to be lost as well.

Numerous applications of these power spectrum techniques have been performed [e.g. Cohen, 1970, 1975; King et al., 1972, 1974; Kulhanek, 1971; Bakun and Johnson, 1973; Flinn et al., 1973; Shumway and Blandford, 1978], with it being quickly recognized that the implied pP delay times and amplitudes were inconsistent with the known overburden velocities and elastic free surface reflection coefficients. Systematically, the pP delay time is longer than expected and the amplitude is smaller. The presence of a clear third arrival for the two large Amchitka explosions (MILROW and CANNIKIN) led to the idea that the missing pP energy was being converted into the even more delayed 'slapdown' arrival.

The most recent amplitude spectrum procedure is that of Murphy et al. [1989] and Murphy [1989], which attempts to achieve a separation of $E(\omega)$ and $R(\omega)$ by using a suite of events recorded by a suite of stations. A linear regression model is used to simultaneously determine average station correction factors and station-corrected, network averaged P wave spectra, under the constraint that the station correction factors at each frequency sum to zero. The procedure is to compute the spectral amplitude in a sequence of frequency bands, ω_k , by using narrowband filters for station j from event i . Then the regression models minimize residual error, $e_{ij}(\omega_k)$, in a least squares sense for the instrument corrected spectra:

$$\log U_{ij}(\omega_k) = \log[E_i(\omega_k)S_i(\omega_k)Q(\omega_k)] + \log R_j(\omega_k) + e_{ij}(\omega_k)$$

where the station correction factors, $R_j(\omega_k)$, describe the systematic, frequency-dependent departures at station j from the average propagation effects (such as average $Q(\omega_k)$) of the network. Once the receiver effects are separated, corrections for attenuation and modulation effects associated with $S_i(\omega_k)$ are removed to obtain $E_i(\omega_k)$. Examples of this

procedure for NTS events are shown in Figure 5, and it is again apparent that low pP amplitudes (A) are obtained, along with large pP delay times relative to the expected values of 0.6-0.9 s. This procedure does not eliminate the problems arising from tradeoffs between the assumed attenuation and source models, but does should help to statistically remove the station influence. Assuming that the station terms sum to zero projects any common effects onto the source model, so a large number of observations must be used in this technique. If pP does not have the same time dependence as P, or if other phases arrive within the time interval encompassed by P and pP, both the timing and amplitude estimates for pP can be biased, as is true of all modeling procedures. If there is significant variation in the pP timing between stations the spectral nulls in the network averaged spectra could be smeared out, leading to an underestimate of true pP amplitude.

Given the tendency for spectral modeling procedures to result in anomalously low amplitude pP phases which are delayed beyond the elastic predictions, one must question the model assumptions used in the various spectral scalloping procedures. While it is quite reasonable to anticipate that some pP energy has been lost to the spallation process, and the downgoing pP reflection will encounter a very disrupted medium, which may have lower average P velocities than the initial overburden, it is certainly not clear that the resultant pP waveform will any longer resemble a simple echo of the direct P arrival. Remember that this is a fundamental assumption in all of the spectral fitting procedures. While we will return repeatedly to this question, it is instructive to consider Figure 6. Two-dimensional finite difference calculations that attempt to account for nonlinear pP reflection processes consistently predict a frequency dependent pP reflection coefficient that is significantly smaller than the elastic value [Bache 1982]. Even small departures from elastic theory will obscure spectral nulls that the techniques described above are designed to find. The resulting time domain waveforms for the two calculations in Figure 6 are virtually identical, which suggests the difficulties to be encountered in the next section where waveform modeling procedures are described.

Waveform Modeling Techniques

A significant disadvantage of the power spectrum procedures is that they all require spectral carpentry on the signal, involving windowing, tapering, and transforming the signal. The degree of spectral scalloping is window dependent, thus high resolution of the pP parameters is difficult to obtain. As a result, many studies have attempted to model the time domain waveforms directly, exploiting the phase information to emphasize the time window of the pP arrival. The synthetics in Figure 7 suggest the potential time domain resolution of pP parameters that could be obtained by comparison with observations, while Figure 8 demonstrates that time domain information does clearly contain gross information

about different test site pP properties. Complete waveform modeling comes with the cost of having to specify many parameters including the transfer functions at the source and receiver, the source model, and the attenuation model, as well as requiring a measure of waveform fit that is sensitive to the pP parameters [e.g. Carpenter, 1966; Hasegawa and Whitham, 1969; Hasegawa, 1971; Bache et al., 1975; Bache et al, 1979; Burdick and Helmberger, 1979; Lundquist et al., 1980; Helmberger and Hadley, 1981; Burdick et al, 1984a; Mellman et al., 1985].

These waveform modeling studies differ primarily in the degree to which they utilize independent constraints on one or more of the various filters required to synthesize the time domain waveform. For example, Hasegawa [1971] and Mellman et al. [1985] utilize detailed crustal transfer functions to account for $R(\omega)$, while Helmberger and Hadley [1981] and Burdick et al. [1984a] constrain the source spectrum, $E(\omega)$, by modeling near-field records, and constrain $Q(\omega)$ by matching absolute amplitudes of teleseismic signals. Figure 9 shows synthetic and observed waveforms for event CANNIKIN from Burdick et al. [1984a], where the pP parameters were selected by matching the general shape of the P waveforms for a large set of stations, allowing for variation in attenuation between stations. No explicit accounting for receiver effects was involved in this analysis since a global set of stations was utilized. The pP delay times inferred from this modeling are very compatible with spectral analysis results; however, the pP amplitudes are closer to the elastic prediction for this time domain modeling. It is not clear whether this inconsistency is a result of inadequate parameterization of the time domain modeling or biases in the spectral carpentry procedures.

Time domain modeling of the entire waveform is, of course, also subject to many trade-offs in the pP parameterization. Figure 10 shows a calculation by Cormier [1982], in which virtually identical waveforms are produced by trading off frequency dependence of the source model, the attenuation operator, and the pP reflection coefficient. In this case, only spectral analysis could differentiate between the models. Recognition of these strong trade-offs led to the development of higher resolution time domain techniques, which strive to remove receiver and propagation effects from the problem by determining inter-event transfer functions that exploit the differential waveform information [Filson and Frasier, 1972; Mellman and Kaufman, 1981].

The most extensively developed of the relative waveform procedures is called intercorrelation [Lay et al., 1984, 1985; Lay, 1985; Burger et al., 1986]. In this procedure, seismograms from a given station for two events at the same test site are equalized by parameterizing $S(t)$ for each event as a spike train, and correcting for differences in the source functions arising from yield scaling. Figure 11 illustrates the

convolution of each observed trace with $E(t)*S(t)$ for the other event. The propagation effects in the mantle and near the receiver, along with the instrument response, are intrinsically accounted for by this procedure. The principal parameters are the spike train sequence, here chosen to involve only the P and pP arrivals, with the pP amplitude and delay time to be determined by making the intercorrelated seismograms as similar as possible. The choice of source function is not as important as for direct forward modeling, because it is the difference in source function between events which influences the equalization. The major limitation of this procedure is again in the specification of a spike train for the source region transfer function, along with the fact that the optimization of spike parameters is only viable with three or fewer spikes in each $S(t)$.

In practice, the intercorrelation procedure is applied to a large set of stations simultaneously for two or more events. Typical results are shown in Figure 12, where three spike versions of $S(t)$ have been used to equalize MILROW and CANNIKIN waveforms. These spike trains are shown after convolution with the respective source functions in the traces labeled M_S and C_S . Note that the second spike, pP is comparable in size to the third, upward, spike, which corresponds to the 'slapdown' arrival. In this study [Lay et al., 1984], the source functions were independently constrained by near-field modeling, to try to minimize the trade-offs with pP parameters. While the preferred pP delay times are in very close agreement with spectral results, especially those obtained by the network averaging techniques such as the spectral magnitude method of Murphy et al. [1989], the amplitudes tend to be closer to elastic than in other methods. Unfortunately there is a tradeoff with the third spike amplitude. The intercorrelation technique is intrinsically most sensitive to differences in pP parameters between the events, so it is possible that the baseline pP amplitudes are biased high; however, the resulting source models do provide good matches to the observed waveforms.

An important characteristic of the intercorrelation method for determining pP parameters is that it intrinsically emphasizes the lower frequencies in the waveforms, because of the convolutional smoothing. Thus, it is reasonable to interpret the resulting pP parameters as being appropriate for the longer periods, with frequency dependence of the pP reflection coefficient likely to give smaller pP amplitudes in procedures which emphasize the higher frequencies. This is supported by Figure 13, which compares spectral ratios of source models obtained by intercorrelation with spectral ratios of actual data [Der et al. 1987b]. While the lowest frequency spectral peak and null are in reasonable agreement, the higher frequency observations do not show the regular beating predicted by the results obtained for spike trains. This particular comparison is somewhat misleading, because it compares event averaged results with single sensor results, and because a long window of 25.6 s

was used to compute the spectral ratios. The intercorrelation results only apply to the first 5 s of the waveform, and it is well known that later P coda shows less scalloping [Lynnes and Lay, 1988] than the early P waveform. Nonetheless, it appears that the spike-train approximation is simply too restrictive to adequately model the pP phase at high frequency by either time or frequency domain techniques.

Deconvolution Procedures

Ideally, one would like to make as few assumptions about $S(\omega)$ as possible, for a frequency dependent pP reflection could require a very complex parameterization. A variety of deconvolution procedures have been utilized to characterize pP, several of which involve very few assumptions about $S(\omega)$, although trade-offs with receiver, source function, and attenuation uncertainties remain. At the heart of most deconvolution procedures is the idea of bandwidth extension, usually accomplished by removing bandlimiting filters such as instrument response. Signal bandwidth is critical to a complete interpretation of the pP arrival in either the time or frequency domains. Frasier [1972], Burdick and Helmberger [1979], Lyman et al. [1986], Douglas et al. [1987] and Stewart [1988] have used time or frequency domain deconvolution to remove the instrument and assumed attenuation effects from teleseismic explosion P waves. The hope is that the resulting signal is not overwhelmed by $R(\omega)$, so that $E(\omega) S(\omega)$ can be isolated. When array data are available, initial stacking of the signals can reduce the effects of heterogeneity in $R(\omega)$, but does not eliminate any common effects.

Examples of the deconvolution of array data are shown in Figure 14, where short period recordings have been deconvolved to first remove the instrument response, and then an attenuation filter. Ideally, the final trace should be $E(\omega) S(\omega)$, with little effect from $R(\omega)$. It is interesting to compare these functions with the intercorrelation results from Figure 12. In general, the close agreement of the results, particularly if the different array deconvolutions were further stacked to better suppress $R(\omega)$, supports the simple three spike version of $S(\omega)$ adopted in the intercorrelation procedure. However, it is clear that the pP phase does have some complexities, notably broadening, which suggest a frequency dependent arrival.

To further characterize the details of $S(\omega)$, the broadband seismogram can be deconvolved by an assumed source model, $E(\omega)$. Extracting the source wavelet can be done by a variety of procedures, one of which is shown in Figure 15, where L1 deconvolution of the source wavelet (along with instrument and attenuation) has been performed by linear programming, with the constraint that the resulting $S(\omega)$ has a minimum number of spikes [Mellman et al., 1985]. Note the complex transfer function which is obtained, which is a combination of source and receiver effects. This procedure is

only as reliable as the choice of $E(\omega)$ and $Q(\omega)$. Autocorrelation and matched filtering are other procedures for characterizing the source and receiver spike trains [Cohen, 1970; Flinn et al, 1973, Douglas et al, 1972]. Another procedure for extracting the propagational impulse train is homomorphic deconvolution [Cohen, 1970; Bakun and Johnson, 1973]. Results of applying this procedure to remove instrument, source and attenuation effects for MILROW and CANNIKIN are shown in Figure 16. Note that the pP and 'slapdown' phases are very similar to the results in Figures 12 and 14.

The latest deconvolutional approach, which involves few assumptions about $S(\omega)$, and explicitly strives to eliminate $R(\omega)$ involves multi-channel maximum likelihood iterative deconvolution of a suite of events recorded at an array of stations [Der et al., 1983, 1987a,b, 1989; Shumway and Der, 1985]. This procedure initiates by estimating each source term $E(\omega)S(\omega)$ by stacking over the suite of observations for an event, then using the average source terms to deconvolve each observation and stack the various observations for a given station. The estimated station terms are then deconvolved from the data, and the procedure is repeated until convergence. In most applications $Q(\omega)$ and $E(\omega)$ are specified. The effective separation of source and receiver terms hinges upon variations in the source terms from event to event. Any common features in the spectra between events can be placed either at the source or at the receivers, with this procedure tending to attribute common terms to the receiver functions.

Application of the iterative deconvolution to several events from the Degelen test site (Figure 17) illustrates the resulting source functions for joint and separate analysis of several arrays. No $E(\omega)$ was deconvolved in this case. Thus, these functions presumably represent $E(\omega) S(\omega)$ alone, to the degree the receiver effects have been successfully removed. Note that the joint deconvolution is greatly simplified relative to the separate array results. This requires either variations in the source radiation with take-off angle and azimuth or incomplete suppression of receiver effects in the separate deconvolutions. If one accepts the assumptions, one can infer that these events have very small pP arrivals, unless they are in some way obscured by the source function and interference with the direct P arrival. The small amplitude of pP may be associated with cratering of the surface for these events. Deconvolution procedures of this type are essential for investigation of events that may involve cratering, which will have a particularly complex surface interaction [Gupta et al., 1985].

Figure 18 illustrates the effect of specifying a source model for $E(\omega)$, and deconvolving it in the multi-channel procedure. The Von Seggern-Blandford (VSB) source model is only one of several parameterized models that can be used, so there is still a direct trade-off with the source model. Overshoot of the source model can strongly affect the ground

displacement overshoot, which is used to estimate the parameters of the pP arrival. Figure 19 illustrates the effect of using a frequency independent attenuation model (constant t^*) versus a frequency dependent attenuation model ($t^*(f)$). While the effects can be subtle, as for INLET, they can also be significant for the pP parameters as for STILTON.

The deconvolutions for Pahute Mesa events in Figure 19 indicate little overshoot of the ground motion (small pP arrivals), and indeed Der et al. [1989] assign pP an amplitude of zero for these events. Intercorrelation for these events has suggested nearly elastic pP amplitudes [Lay, 1985], and the spectral stacking results of Murphy [1989] give intermediate values for pP amplitudes, but almost the same delay times as for intercorrelation. Can frequency dependence of pP reconcile these inconsistencies? The situation actually becomes more confused when Figure 20 is considered. This shows determinations of the broadband source functions $[E(t)*S(t)]$ for four large Pahute Mesa events determined by the separate deconvolution procedures of Lyman et al. [1986], and Der et al. [1987a]. The results are from the same data at the EKA array, but the results of Lyman et al. [1985] exhibit strong overshoots, consistent with significant pP arrivals, whereas the multi-channel deconvolutions suggest no pP arrival at all. The latter results have higher frequency content as well.

The path from NTS to EKA is known to be in a direction of strong defocussing [Lynnes and Lay, 1988], and the bandwidth of the signals is further limited by attenuation. As a consequence of the limited bandwidth, many of the ground displacements are very similar, despite the differences in source function and burial depth. It appears that these common features between events have been assigned to the receivers in the multi-station deconvolutions, which may or may not be correct. In addition, the techniques emphasize the longer period content in very different ways, with the multi-channel procedure placing higher weight on the higher frequency spectra. Truly reliable separation of the receiver functions appears to require more dramatic differences between the depths and source functions in the population of sources than are commonly observed for a set of explosions at a given test site.

It is also possible that the difference in passband of the deconvolutions combined with a frequency dependent pP arrival is primarily responsible for the inconsistent results for NTS events. Figure 21 shows several bandpass filtered versions of a synthetic ground displacement which has a pP reflection that depends on frequency [Der et al., 1989]. Note that the bandwidth influences the strength of the apparent pP arrival. Thus, it may actually be possible to reconcile all of the pP determinations for the Pahute Mesa events by recognizing the varying frequency sensitivity of the techniques, and invoking a physically reasonable frequency dependence for the pP reflection process. Even when very

broadband source functions are available, care must be taken in interpreting the pP parameters due to the uncertainty in the source time function, as well as the interference effect between P and pP. This is illustrated in Figure 22, which shows errors in pP lag time resulting from the limited bandwidth of the synthetic pulses. Also note how very short time delays can lead to a rapid variation in peak to peak amplitude, which could bias magnitude measurements for small, shallow events.

pP AND SPALL REPRESENTATIONS

Thus far, we have emphasized the empirical analyses of pP parameters, and found frequent indication of additional arrivals that appear to be from the source region. What is the precise physics by which pP and spall processes are linked, and how does it affect the teleseismic manifestation of pP? This is a poorly understood topic, perhaps because of the many difficulties encountered in quantifying the pP arrival alone, as described above. Nonetheless, it is well recognized on physical grounds that spall and pP must be intimately linked, and a simple three-spike model is inadequate to represent the process [Day et al., 1983]. Burdick et al. [1984] proposed a phenomenological model for the coupled pP and spall process which can explain some of the anomalous properties of pP, such as its apparent delay and additional arrivals. Their model, constructed to conserve momentum is shown in Figure 23, where the spall process is initiated by the pP arrival, and produces both downgoing and upgoing waves during both spall opening and closing. The initial downgoing spall arrival will destructively interfere with the pP arrival, resulting in an apparent delay of the surface interaction. The spall source can be viewed as a tensional crack or a distributed source over a conical surface, for computational purposes. Utilizing a model of this type, synthetic seismograms can be constructed which are quite consistent with the results of intercorrelation and spectral methods for the Amchitka events, as shown in Figure 24. While clearly a simplification of the non-linear spallation process, this type of approach provides a parameterization of the complete free surface interaction that can be used to synthesize signals at all distance ranges [Burdick et al., 1984]. Further development of parameterized free surface interaction models is required to enable a more complete interpretation of the source functions that are being obtained by deconvolution procedures.

CURRENT NUMERICAL MODELING PROCEDURES

Along with the many developments in pP waveform analysis, there have been substantial advances in numerical modeling procedures that are revealing the physics of the free surface interaction and its teleseismic manifestation. An informative example is provided by the implementation of the Kirchhoff-Helmholtz wave theory to assess frequency dependent pP reflection from the free surface [Scott and Helmburger, 1983]. Figure 25

shows the result of a spatially varying pP reflection coefficient, decreasing in amplitude just above the shot point. The three-dimensional wave theory predicts a pP reflection which will be delayed and decreased in amplitude in proportion to the anomalous zone of low reflection, which physically may correspond to the spall zone. This model can qualitatively account for the anomalous delay, decreased amplitude and frequency dependence of the actual pP observations. Accounting for the missing energy requires more complete modeling procedures, such as the two-dimensional non-linear finite-difference calculations of McLaughlin et al. [1988], in which an attempt is made to include all of the physics of the actual spallation and pP reflection process. These axisymmetric calculations tend to actually underpredict the pP arrival, so it is clear that all of the pertinent physics has not yet been included, and possibly the assumption of axisymmetry is inadequate to explain actual pP reflection processes.

Numerical modeling procedures are also useful for addressing heterogeneity in the shallow crustal velocity structure in the vicinity of the shotpoint. Even elastic finite difference calculations for complex regions such as the Yucca Flat Test Site at NTS exhibit very complex P coda, initiating with the pP arrival [Figure 26] [Stead and HelMBERGER, 1988; McLaughlin et al, 1986]. In this calculation [Stead and HelMBERGER, 1988] of teleseismic waveforms, a hybrid two-dimensional finite difference and Kirchhoff-Helmholtz procedure was used to account for the shallow crustal reflections and wave conversions near the source. This level of modeling is critical for appraising the complexity apparent in source function deconvolutions like those in Figure 20. When the source coda is as strong as in Figure 26, methods invoking simple assumptions of 2 or 3 spike source functions will clearly give erroneous results for pP. Another situation in which numerical modeling is necessary, is when there is significant surface topography near the test site (a common occurrence). Figure 27 shows two dimensional finite-difference calculations for a line source [McLaughlin et al., 1987], that illustrate how the upgoing explosive wavefield can be disrupted by topography. Future evaluation of three dimensional effects and broadband data will help to assess whether the pP phase actually has significant azimuthal variations, as suggested by Figure 17.

DISCUSSION AND CONCLUSIONS

The current level of understanding of the teleseismic pP phase from underground nuclear explosions is far from complete. This review has illustrated the diversity of procedures and results which have been obtained over the past twenty years of seismological investigations. There is general agreement that the actual pP phase is influenced by frequency dependent reflection, with longer period energy having higher reflection coefficients. The estimated delay of pP phase may be biased when the phase is assumed to

be a reflected impulse, and all estimation of pP parameters are influenced by the bandwidth of the technique being used as well as the assumptions about the frequency content. As a general rule, many of the contradictory pP parameters in the literature could be reconciled by specifying the frequency band most emphasized in the processing, and the greatest stability appears to accompany the largest bandwidth procedures.

Given the direct trade-offs between source and propagation effects for teleseismic signals, especially when frequency dependence is involved, it appears that the most reasonable approach to analyzing the pP phase is simple broadband ground motion restitution. This involves removing the instrument response effects to extend the bandwidth of the signal. The resulting signals can then be interpreted for a variety of assumed attenuation and source models, and stacked to suppress receiver effects. The latter processing should always acknowledge the direct trade-offs that exist, and should fully explore assumptions about the source before placing any weight on the resulting interpretations of the pP parameters, depth, coupling, etc.. Spectral factoring to separate source and receiver transfer functions tends to emphasize high frequency content, and is unstable with respect to partitioning of common spectral characteristics.

There is a need for more numerical analysis of the pP-spall process, as interpretation of the broadband ground motions requires a parametric description of this energy partitioning. In addition, continued development of numerical models to elucidate the complexity of pP and subsequent coda arising from complex near-source structure and surface topography is very important. The numerical studies performed to date suggest that even the elastic processes accompanying the pP reflection are very complex, and possibly azimuthally variable.

Acknowledgments. Thanks to Steve Taylor and Howard Patton for organizing a very stimulating symposium on nuclear explosions processes. John Vidale provide helpful comments on the manuscript. This research was supported by the W. M. Keck Foundation and the Defense Advanced Research Projects Agency and was monitored by the Geophysics Laboratory under Contract F19628-89-K-0011. This is contribution No. 99 of the Institute of Tectonics and C. F. Richter Seismological Laboratory.

REFERENCES

- Bache, T. C., Estimating the yield of underground nuclear explosions, *Bull. Seism. Soc. Am.*, 72, S131-S168, 1982.
- Bache, T. C., T. R. Blake, J. T. Cherry, T. G. Barker, D. G. Lambert, J. M. Savino, and N. Rimer, An explanation of the relative amplitudes of the teleseismic body waves generated by explosions in different test areas at NTS, *S-Cubed Technical Report, DNA 3958F*, La Jolla, California, 1975.
- Bache, T. C., S. M. Day, and J. M. Savino, Automated magnitude measures, earthquake source monitoring, VFM discriminant testing and summary of current research, *Tech. Report SSS-R-79-3933*, S-Cubed, La Jolla, California, 1979.
- Bakun, W. H., and L. R. Johnson, The deconvolution of teleseismic P waves from explosions MILROW and CANNIKIN, *Geophys. J. R. astr. Soc.*, 34, 321-342, 1973.
- Burdick, L. J., and D. V. Helmberger, Time functions appropriate for nuclear explosions, *Bull. Seism. Soc. Am.*, 69, 957-973, 1979.
- Burdick, L. J., J. S. Barker, D. V. Helmberger, and D. G. Harkrider, Linear elastic waveform modeling in the inelastic region of underground nuclear explosions, in *The Vela Program*, Ed. A. Kerr, Executive Graphic Services, Washington, D.C., 130-138, 1985.
- Burdick, L. J., T. Lay, D. V. Helmberger, and D. G. Harkrider, Implications of records from the spall zone of the Amchitka tests to nonlinear losses in the source region and to elastic radiation by spall, *Tech. Report, WCCP-R-84-03*, Woodward-Clyde Consultants, Pasadena, CA 1984b.
- Burdick, L. J., T. Wallace, and T. Lay, Modeling near-field and teleseismic observations from the Amchitka test site, *J. Geophys. Res.*, 89, 4373-4388, 1984a.
- Burger, R. W., T. Lay and L. J. Burdick, Estimating the relative yields of the Novaya Zemlya tests by waveform intercorrelation, *Geophys. J. R. astr. Soc.*, 87, 775-800, 1986.
- Carpenter, E. W., A quantitative evaluation of teleseismic explosion records, *Proc. R. Soc., A*, 290, 396-407, 1966.
- Cohen, T. J., Source depth determinations using spectral, pseudo-autocorrelation and cepstral analysis, *Geophys. J. R. astr. Soc.*, 20, 223-231, 1970.
- Cohen, T. J., Ps and pP phases from seven Pahute Mesa events, *Bull. Seism. Soc. Am.*, 65, 1029-1032, 1975.
- Cormier, V. F., The effect of attenuation on seismic body waves, *Bull. Seism. Soc. Am.*, 72, S169-S200, 1982.

- Day, S. M., N. Rimer, and J. T. Cherry, Surface waves from underground explosions with spall: analysis of elastic and nonlinear source models, *Bull. Seism. Soc. Am.*, 73, 247-264, 1983.
- Der, Z. A., A. C. Lees, W. W. Chan, R. H. Shumway, K. L. McLaughlin, E. Smart, T. W. McElfresh, and M. E. Marshall, Maximum likelihood multichannel deconvolution of P waves at seismic arrays, *Tech. Report, TGAL-87-3*, Teledyne Geotech, Alexandria, VA, 1987a.
- Der, Z. A., A. C. Lees, K. L. McLaughlin, and R. H. Shumway, Multichannel deconvolution of teleseismic short period P waves at seismic arrays and three component stations, *Geophys. J. R. astr. Soc.*, in press, 1989.
- Der, Z. A., R. H. Shumway, and A. C. Lees, Multichannel deconvolution of P waves at seismic arrays, *Bull. Seism. Soc., Am.*, 77, 195-211, 1987b.
- Der, Z. A., R. H. Shumway, L. M. Anderson, T. W. McElfresh, and J. A. Burnett, Analysis of estimators of pP times and amplitudes, *Tech. Report TGAL-TR-83-8*, Teledyne Geotech, Alexandria, VA, 1983.
- Douglas, A., P. D. Marshall, and J. B. Young, The P waves from the Amchitka Island explosions, *Geophys. J. R. astr. Soc.*, 90, 101-117, 1987.
- Douglas, A., D. J. Corbishley, C. Blamey, and P. D. Marshall, Estimating the firing depth of underground explosions, *Nature*, 237, 26-28, 1972.
- Eisler, J. D., F. Chilton, and F. M. Sauer, Multiple subsurface spalling by underground nuclear explosions, *J. Geophys. Res.*, 71, 3923-3927, 1966.
- Filson, J., and C. W. Frasier, Multisite estimation of explosive source parameters, *J. Geophys. Res.*, 77, 2045-2061, 1972.
- Flinn, E. A., T. J. Cohen, and D. W. McCowan, Detection and analysis of multiple seismic events, *Bull. Seism. Soc. Am.*, 63, 1921-1936, 1973.
- Frasier, C. W., Observations of pP in the short period phases of NTS explosions recorded at Norway, *Geophys. J. R. astr. Soc.*, 31, 99-109, 1972.
- Gupta, I. N., and R. R. Blandford, A study of P waves from Nevada test site explosions: near-source information from teleseismic observations?, *Bull. Seism. Soc. Am.*, 77, 1041-1056, 1987.
- Gupta, I. N., K. L. McLaughlin, and R. A. Wagner, Analysis of regional data from cratering and non-cratering nuclear explosions: *Tech. Report, TGAL-85-5*, Teledyne Geotech, Alexandria, VA, 1988.
- Hasegawa, H. S., Analysis of teleseismic signals from underground nuclear explosions originating in four geological environments, *Geophys. J. R. astr. Soc.*, 24, 365-381, 1971.

- Hasegawa, H. S., Analysis of amplitude spectra of P waves from earthquakes and underground explosions, *J. Geophys. Res.*, **77**, 3081-3096, 1972.
- Hasegawa, H. S., and K. Whitham, Theoretical response of a seismograph at Yellowknife, Northwest Territories, to an underground explosion at Nevada test site, *Canadian J. Earth Sci.*, **6**, 517-520, 1969.
- Helmberger, D. V., and D. M. Hadley, Seismic source functions and attenuation from local and teleseismic observations of the NTS events JORUM and HANDLEY, *Bull. Seism. Soc. Am.*, **71**, 51-67, 1981.
- Helmberger, D. V., and D. G. Harkrider, Seismic source description of underground explosions and a depth discriminate, *Geophys. J. R. astr. Soc.*, **31**, 45-66, 1972.
- King, C.-Y., A. M. Abo-Zena, and J. N. Murdock, Teleseismic source parameters of the LONGSHOT, MILROW and CANNIKIN nuclear explosions, *J. Geophys. Res.*, **79**, 712-718, 1974.
- King, C.-Y., W. H. Bakun, and J. N. Murdock, Source parameters of nuclear explosions MILROW and LONGSHOT from teleseismic P waves, *Geophys. J. R. astr. Soc.*, **31**, 27-44, 1972.
- Kulhanek, O., P wave amplitude spectra of Nevada underground nuclear explosions, *Pure Appl. Geophys.* **88**, 121-136, 1971.
- Lay, T., Estimating explosion yield by analytical waveform comparison, *Geophys. J. R. astr. Soc.*, **82**, 1-31, 1985.
- Lay, T., L. J. Burdick, and D. V. Helmberger, Estimating the yields of the Amchitka tests by waveform intercorrelation, *Geophys. J. R. astr. Soc.*, **78**, 181-207, 1984.
- Lay, T., L. J. Burdick, D. V. Helmberger, and C. G. Arvesen, Estimating seismic yield and defining distinct test sites using complete waveform information, in *The Vela Program*, ed. A. Kerr, Executive Graphic Services, Washington, D.C., 597-610, 1985.
- Lay, T., D. V. Helmberger, and D. G. Harkrider, Source models and yield-scaling relations for underground nuclear explosions at Amchitka Island, *Bull. Seism. Soc. Am.*, **74**, 843-862, 1984.
- Lay, T., and J. L. Welc, Analysis of near-source contributions to early P-wave coda for underground explosions. I. Waveform complexity, *Bull. Seism. Soc. Am.*, **77**, 1017-1040, 1987.
- Lundquist, G. M., G. R. Mellman, and D. M. Hadley, Relative receiver functions for three different array concepts, *Tech. Report SGI-R-80-021*, Sierra Geophysics, Inc., Redmond, Washington, 1980.

- Lyman, N. S., A. Douglas, P. D. Marshall, and J. B. Young, P seismograms recorded at Eskdalemuir, Scotland from explosions in Nevada, USA, *Tech. Report, AWRE Report No. O 10/86*, 1986.
- Lynnes, C. S., and T. Lay, Observations of teleseismic P wave coda for underground explosions, *Pure Appl. Geophys.*, 128, 231-249, 1988.
- McLaughlin, K. L., T. G. Barker, S. M. Day, B. Shkoller, and J. L. Stevens, Effects of depths of burial and tectonic strain release on regional and teleseismic explosions waveforms, *Tech. Report, SSS-R-88-9844*, S-Cubed, La Jolla, CA, 1988.
- Mellman, G. R., and S. K. Kaufman, Relative waveform inversion, *Tech. Report, SGI-R-81-048*, Sierra Geophysics, Redmond, WA, 1981.
- Mellman, G. R., S. K. Kaufman, and W. C. Tucker, Depth corrections for yield estimation of underground nuclear explosions, in *The Vela Program*, Ed. A. Kerr, Executive Graphics Services, Washington, D.C., 741-747, 1985.
- Molnar, P., P-wave spectra from underground nuclear explosions, *Geophys. J. R. astr. Soc.*, 23, 273-287, 1971.
- Müller, G., Seismic moment and long-period radiation of underground nuclear explosions, *Bull. Seism. Soc. Am.*, 63, 847-857, 1973.
- Murphy, J. R., Network-averaged teleseismic P wave spectra for underground explosions, Part II. Source characteristics of Pahute Mesa explosions, *Bull. Seism. Soc. Am.*, 79, 156-171, 1989.
- Murphy, J. R., B. W. Barker, and A. O'Donnell, Network averaged teleseismic P wave spectra for underground explosions, Part I. Definitions and examples, *Bull. Seism. Soc. Am.*, 79, 141-155, 1989.
- Scott, P., and D. Helmberger, Applications of the Kirchhoff-Helmholtz integral to problems in seismology, *Geophys. J. R. astr. Soc.*, 72, 237-254, 1983.
- Shumway, R. H., and R. R. Blandford, On detecting and estimating multiple arrivals from underground nuclear explosions, *Tech. Report, SDAC-TR-77-8*, Teledyne Geotech, Alexandria, VA, 1978.
- Shumway, R. H., and Z. A. Der, Deconvolution of multiple time series, *Technometrics*, 27, 385-393, 1985.
- Springer, D. L., Secondary sources of seismic waves from underground nuclear explosions, *Bull. Seism. Soc., Am.*, 64, 581-594, 1974.
- Stead, R. J., and D. V. Helmberger, Numerical-analytical interfacing in two dimensions with applications to modeling NTS seismograms, *Pure Appl. Geophys.*, 128, 157-193, 1988.

- Stewart, R. C., P wave seismograms from underground explosions at the Shagan River test site recorded at four arrays, *Tech. Report, AWRE Report No. O 4/88*, 1988.
- Taylor, S. R., and G. E. Randall, The effects of spall on regional seismograms, *Geophys. Res. Lett.*, 16, 211-214, 1989.
- Wyss, M., T. C. Hanks, and R. C. Liebermann, Comparison of P-wave spectra of underground explosions and earthquakes, *J. Geophys. Res.*, 76, 2716-2729, 1971.

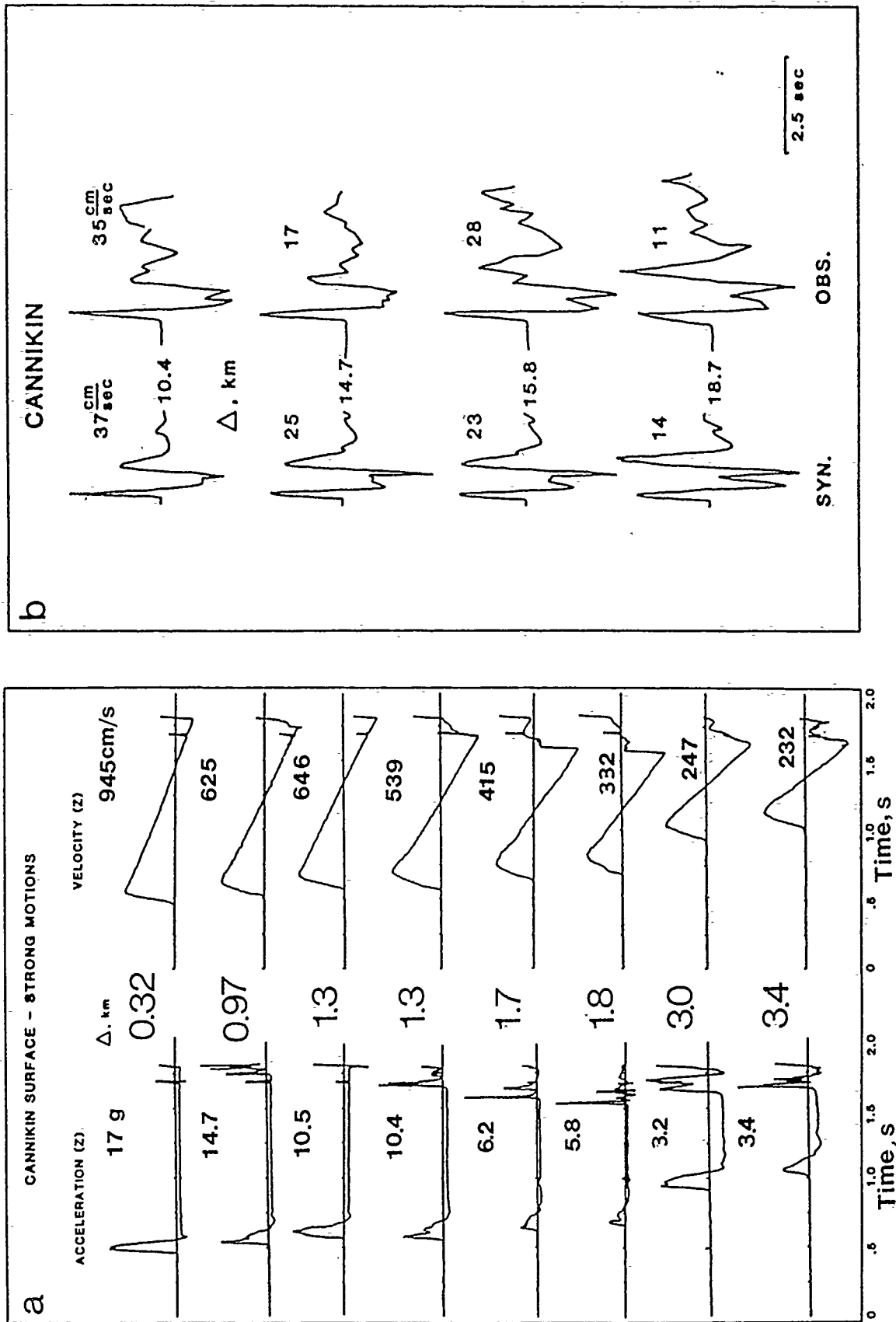


Figure 1. a) Surface vertical accelerations and velocity recordings from the spill zone for CANNIKIN. b) Surface vertical velocity synthetics and observations for CANNIKIN from distances beyond the spill zone. [From Burdick et al., 1984b].

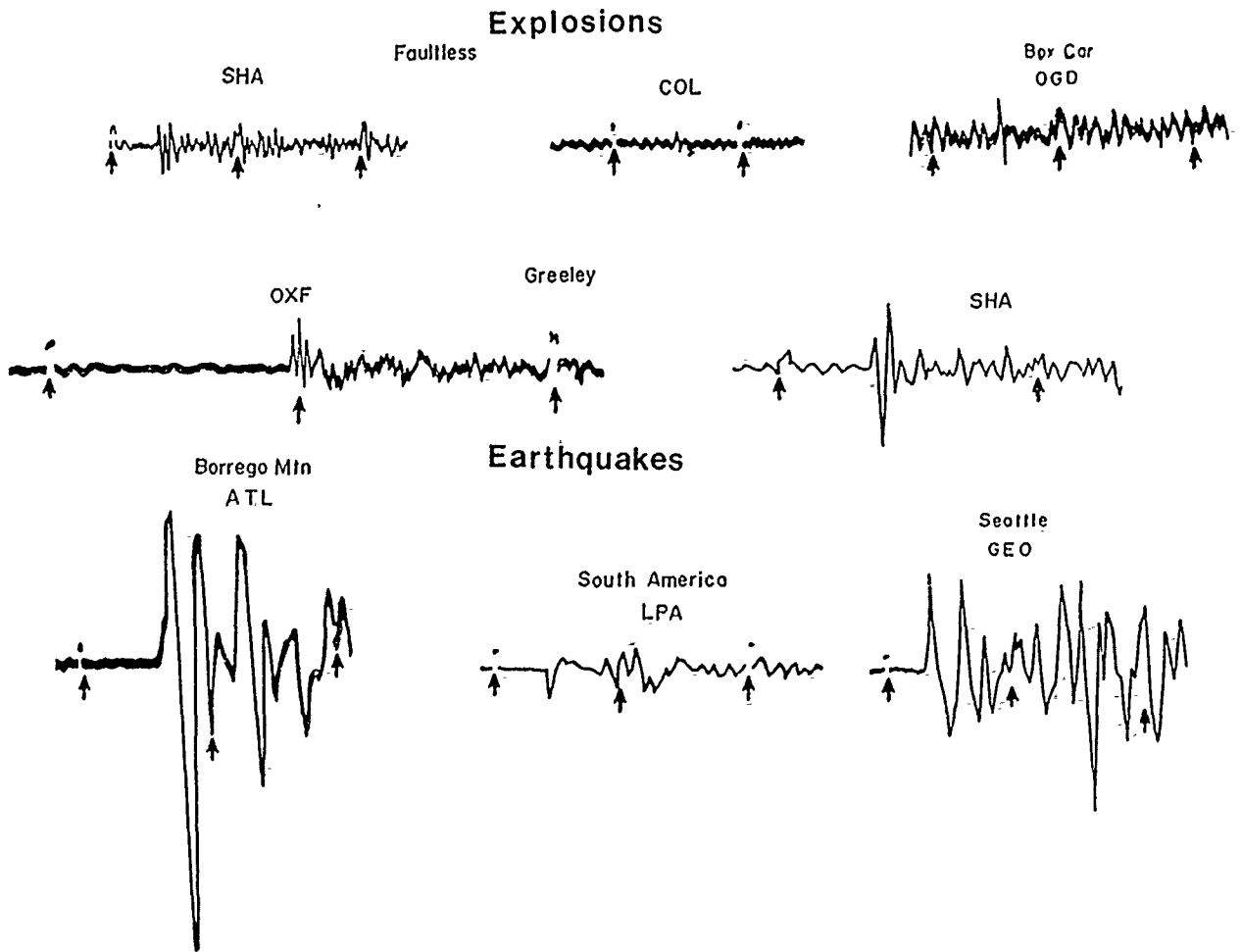


Figure 2. Comparison of WWSSN long period P recordings for three NTS events; GREELEY, BOXCAR, and FAULTLESS, and three earthquakes; Borrego Mountain, California (April 9, 1968); Peru (April 13, 1963), and Seattle (April 29, 1965), all having $m_b=6.2-6.5$. Arrows indicate minute marks. Note the high frequency character of the P arrivals for the explosions relative to the earthquakes. [From Molnar, 1971].

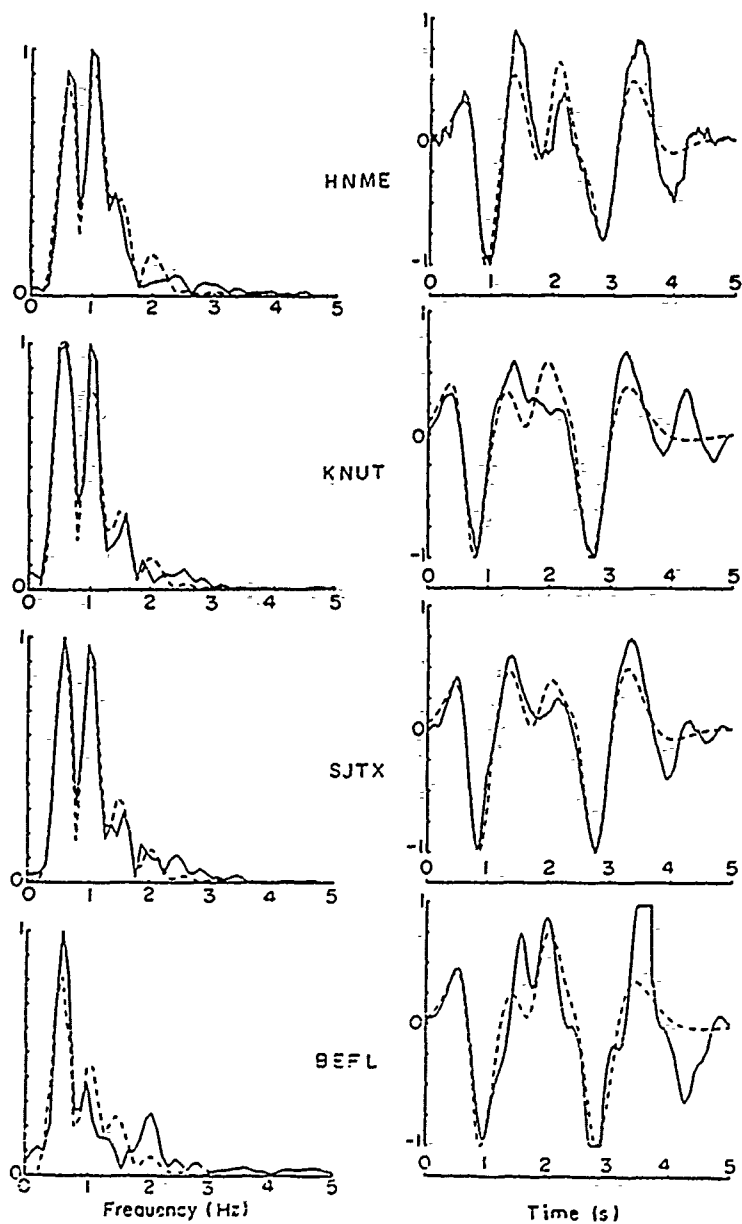


Figure 3. Observed spectral modulus (solid line) and least squares fit of a three spike model (dashed line) for CANNIKIN are shown on the left. The corresponding time domain traces are shown on the right. [From Bakun and Johnson, 1973].

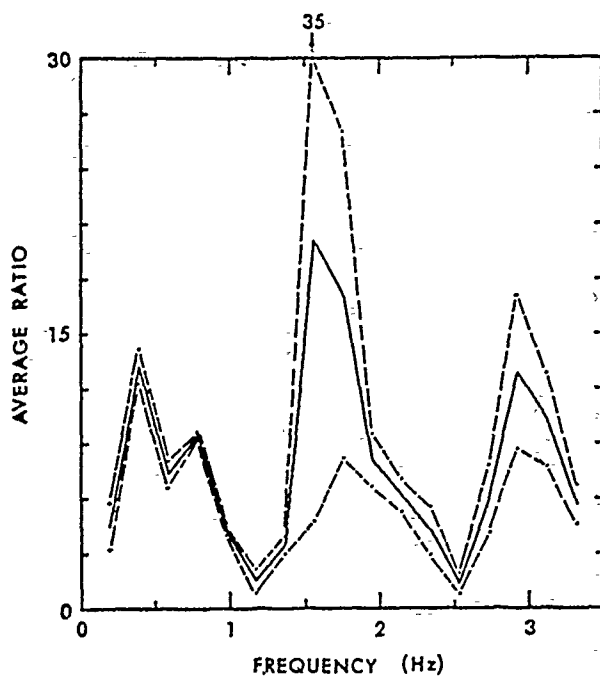


Figure 4. Average spectral ratio of MILROW/LONGSHOT using stations KNUT, RKON, LCNM, and HNME. The dashed lines indicate the standard deviation of the average. The time window was 5 s. [From King et al., 1972].

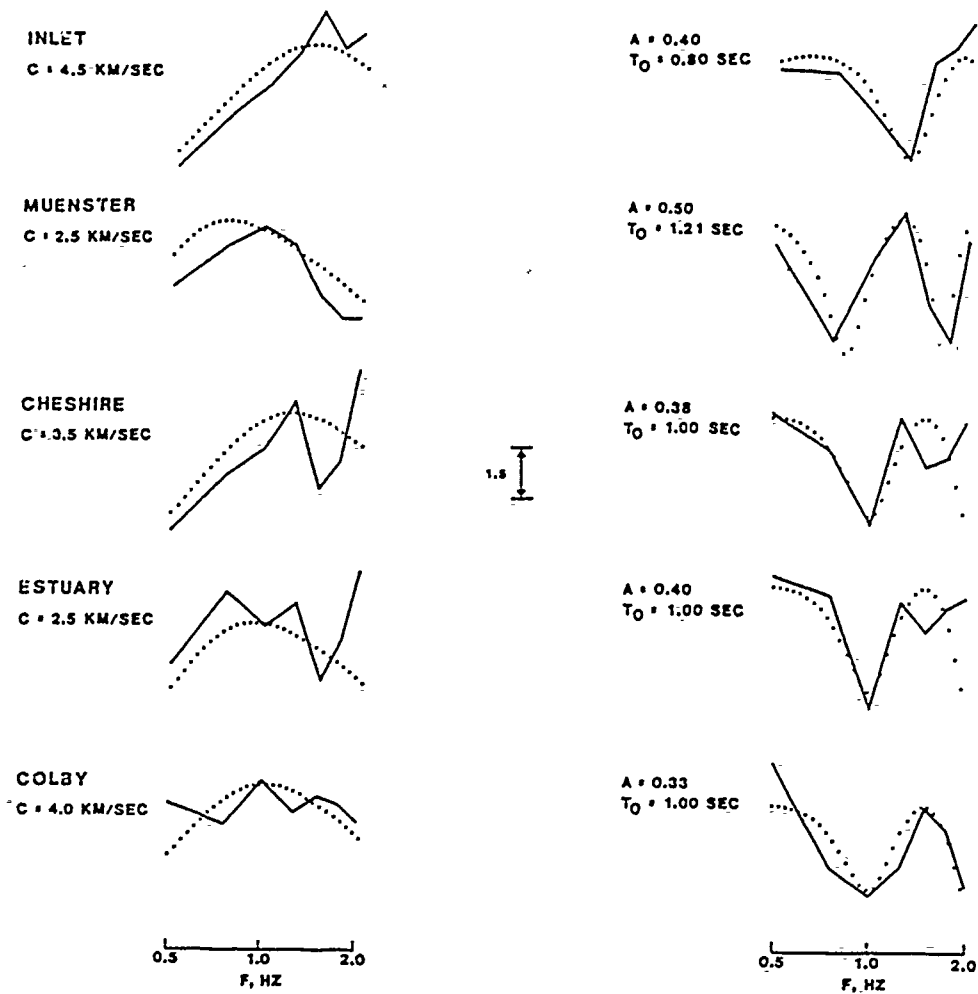


Figure 5. Comparison of normalized observed (solid) and theoretical (dotted) network-averaged P wave spectra for Pahute Mesa explosions. The spectra on the left are corrected for pP and attenuation, while those on the right show the fitting of optimum pP amplitude (A) and relative delay time (τ_0). The source spectra involve a yield and source depth scaled model. [From Murphy, 1989].

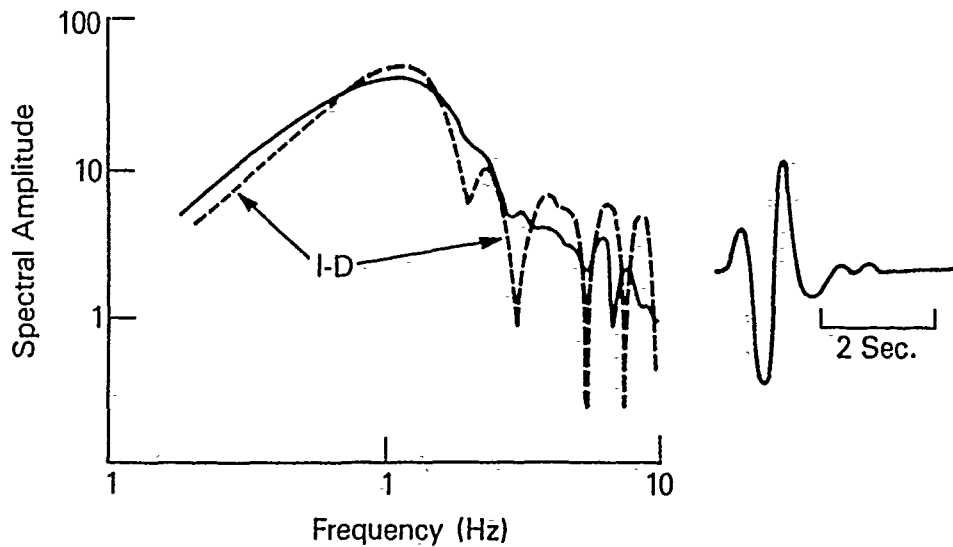


Figure 6. Far-field displacement spectra for a one-dimensional finite difference model with elastic pP reflection processes, and a two-dimensional model with non-linear pP reflection process. The source was a 20 kt explosion at a depth of 1000 m in a geology like that at the PILED RIVER site. Note that the scalloping of the spectra is very different, with the elastic pP arrival producing strong spectral nulls, while the non-linear model does not. The synthetic teleseismic P wave (including a KS36000 instrument response) is virtually identical for the two sources, and is shown at the right. [Bache, 1982].

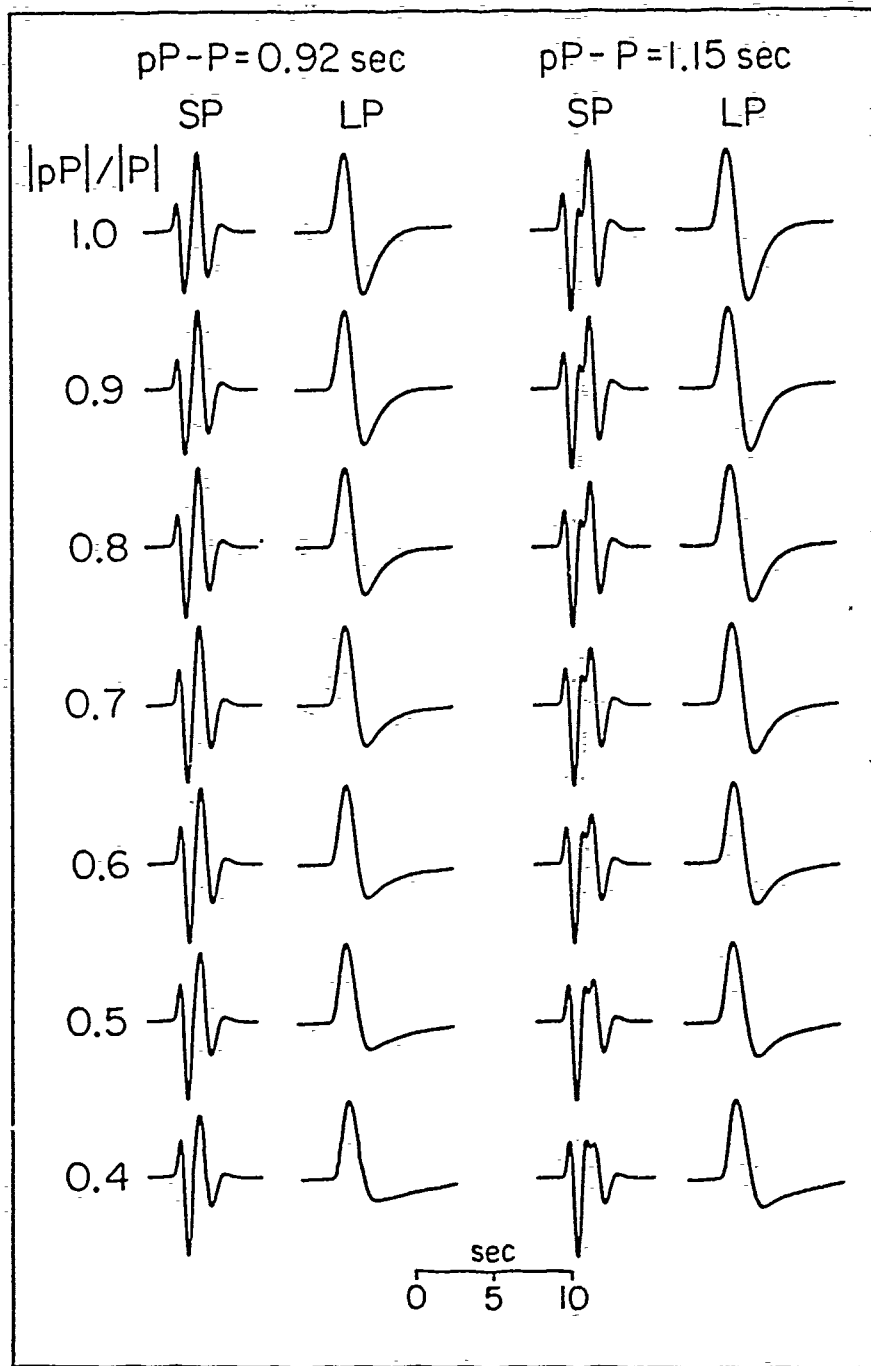


Figure 7. Synthetic short period and long period explosion signals for a common source model and attenuation function, but with varying pP lag time and relative amplitude. [From Burdick et al., 1984a].

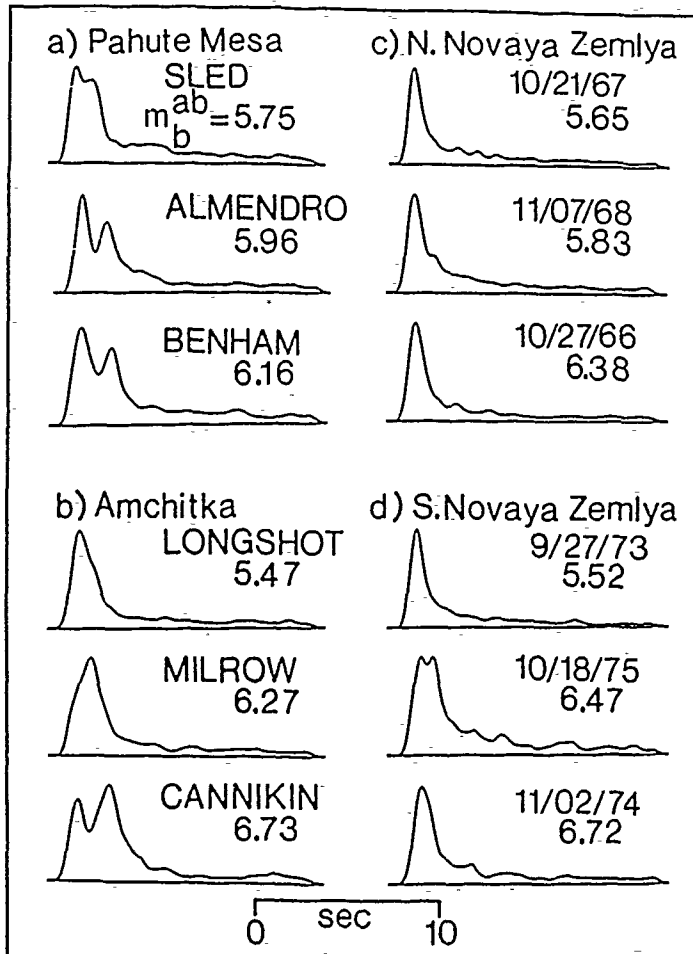


Figure 8. Stacked envelopes of WWSSN short period recordings for explosions in several different test sites. The complexity of the main peak for Pahute Mesa events indicates the delayed pP and strong spall arrivals for this test site relative to the Novaya Zemlya sites. Detailed consideration of the individual seismograms can ideally quantify the associated pP parameters, which then reflect the emplacement medium. [Lay and Welc, 1987].

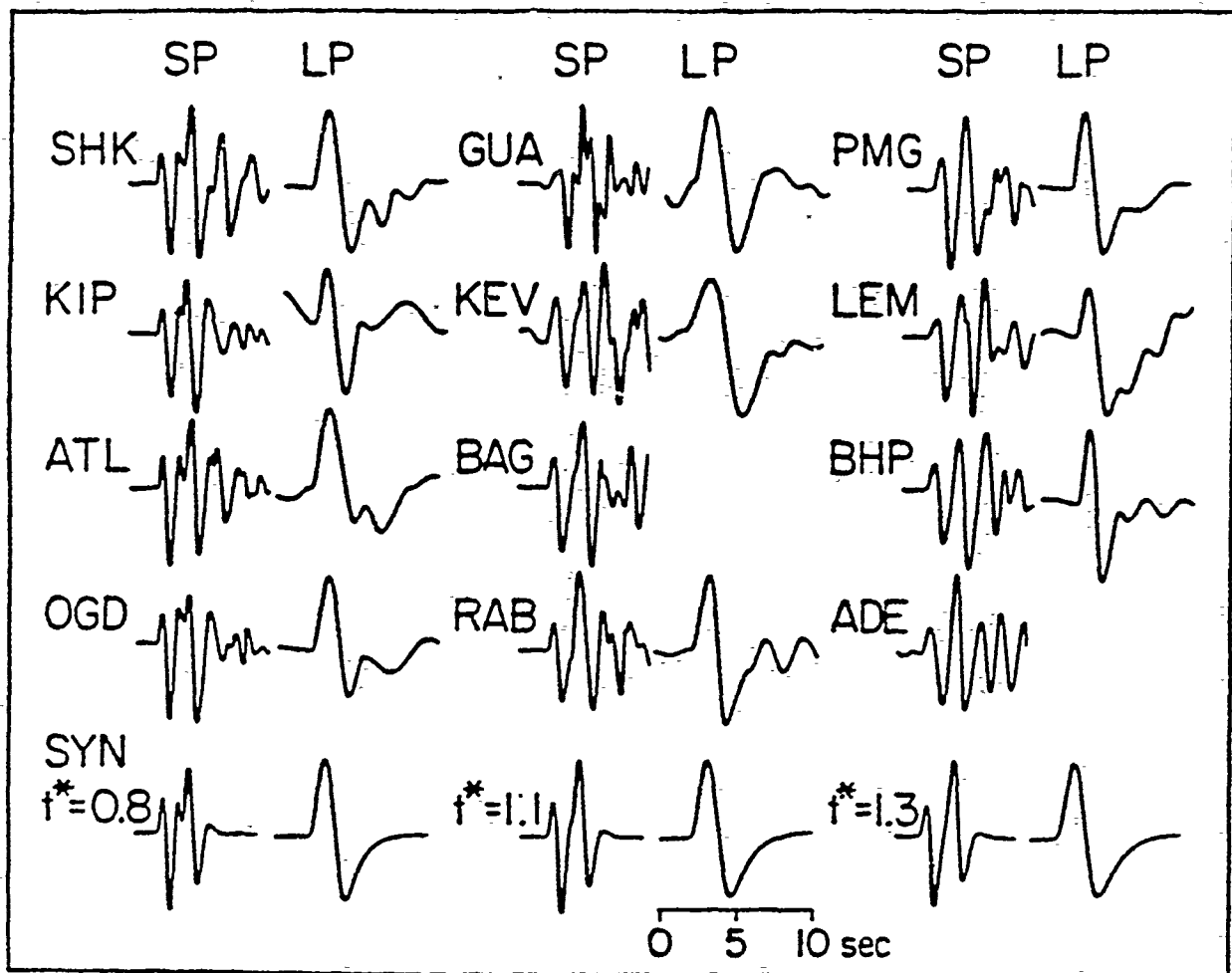


Figure 9. Comparison of observed short and long period P waves for CANNIKIN with synthetics for a range of attenuation parameters (t^*). The synthetics were generated using a near-field source model, $\alpha = -.9$, and $\tau_0 = 1.15$ s. [From Burdick et al., 1984a].

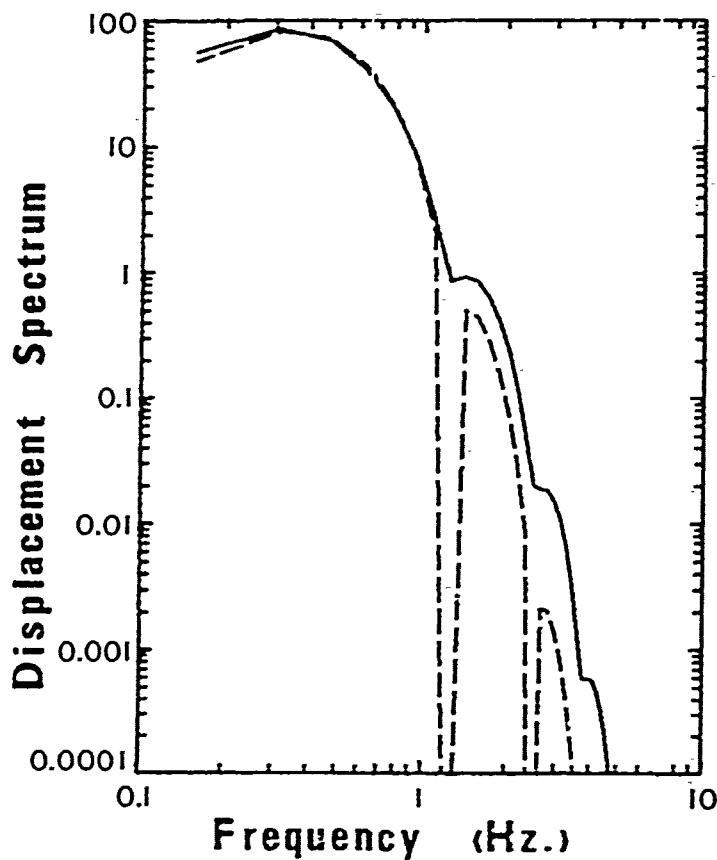
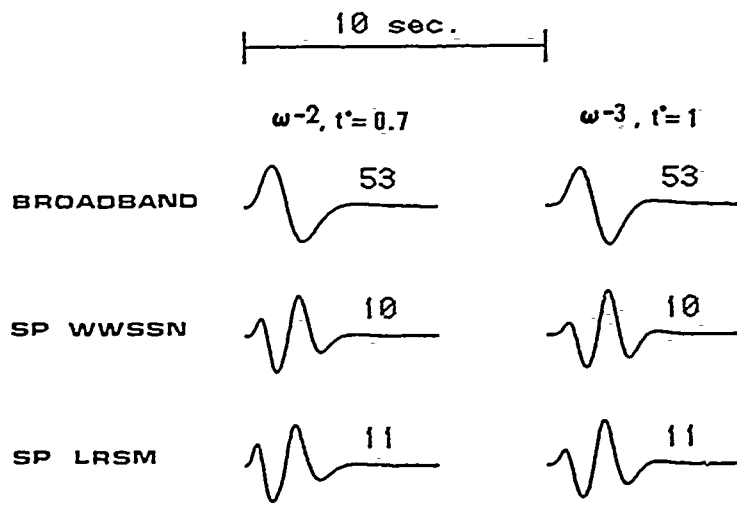


Figure 10. Synthetic seismograms and amplitude spectra for two models for event MILROW, which illustrate the trade-offs between parameters. The synthetics on the left and the solid line spectra are for an ω^{-2} source model, with $t^*=0.7$ s, and a pP reflection coefficient modified from the elastic model by a factor $F=0.5+0.5\exp[-(\omega/2\pi)^2]$. The synthetics on the right, and the dashed spectra are for an ω^{-3} source model, with $t^*=1.0$ s, and an elastic pP reflection coefficient. [From Cormier, 1982].

ADE-OBSERVED SOURCE INTERCORRELATION

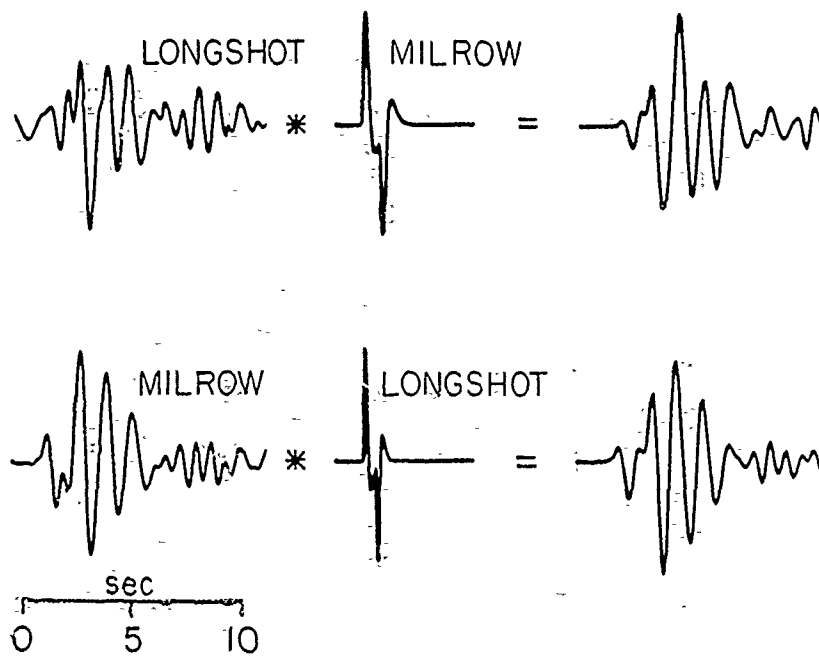


Figure 11. Example of intercorrelation of seismograms recorded at WWSSN station ADE for Anchitka events MILROW and LONGSHOT. The observations are each convolved with $E(t) * S(t)$ for the other event to equalize the waveforms. $S(t)$ in this case involves just the P and pP arrivals, with the pP parameters being adjusted to optimize the equalized waveform agreement. [From Lay et al., 1984].

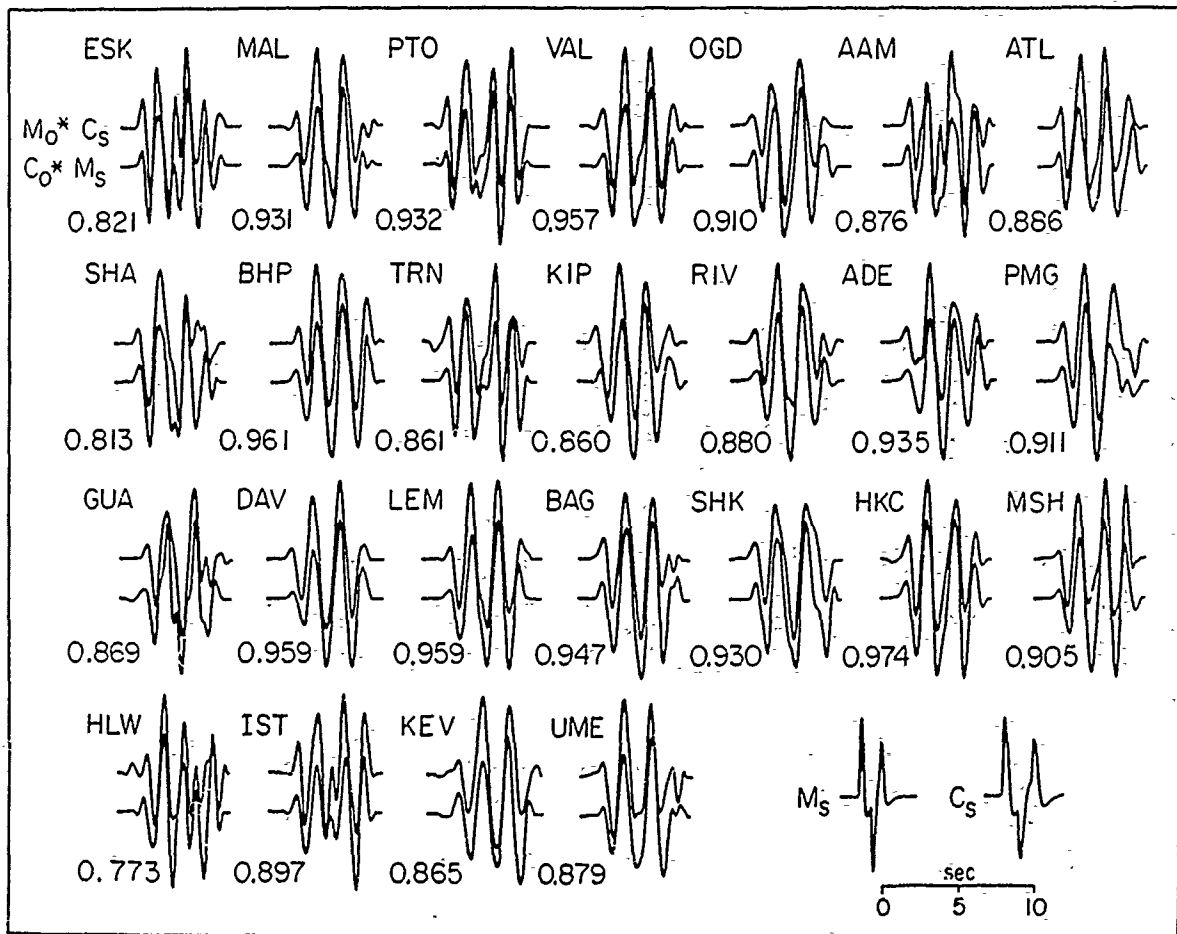


Figure 12. Equalized waveforms for the optimal MILROW:CANNIKIN intercorrelation for $S(t)$ with three spikes for each event. In this case the source functions were determined by modeling near-field records. The top trace in each pair is a MILROW observation convolved with the CANNIKIN $E(t)*S(t)$, which is shown below (C_S), and the lower trace is the CANNIKIN observation at the same station convolved with the MILROW $E(t)*S(t)$, which is also shown below (M_S). [From Lay et al., 1984].

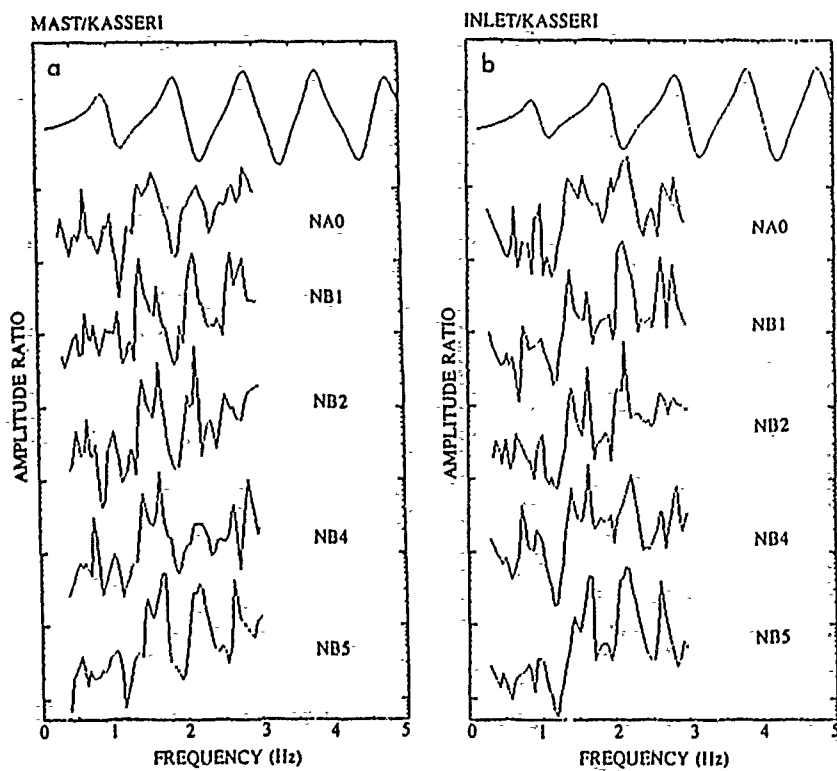


Figure 13. Comparison of spectral ratios for pairs of Pahute Mesa events at NORSAR channels with predicted ratios from intercorrelation results [Der et al., 1979b]. Note the poor agreement at frequencies above 1 Hz.

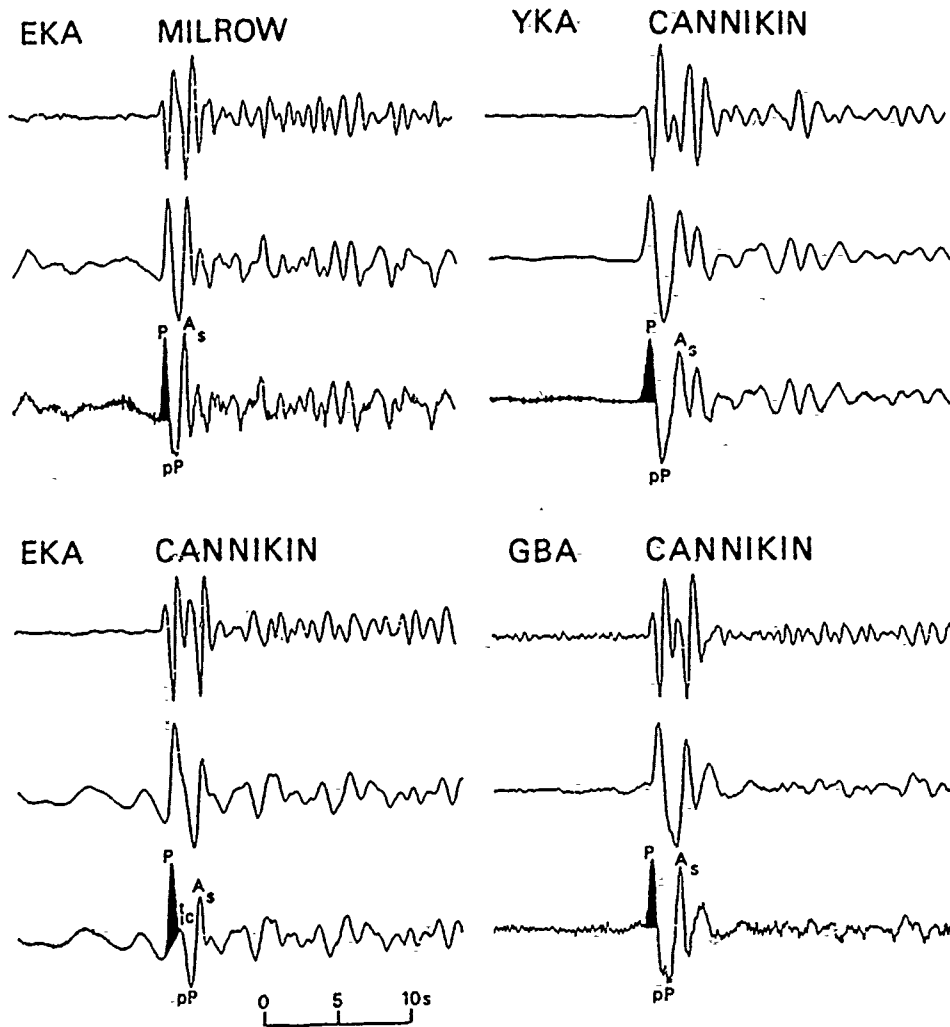


Figure 14. Short period and derived broadband recordings for MILROW and CANNIKIN, from four UK array beams. In each case the top trace is the short period event beam, the second trace is deconvolved ground motion, and the third trace is the ground motion corrected for attenuation assuming $t^*=0.15$. A_s corresponds to the third arrival which has positive polarity. [From Douglas et al., 1987].

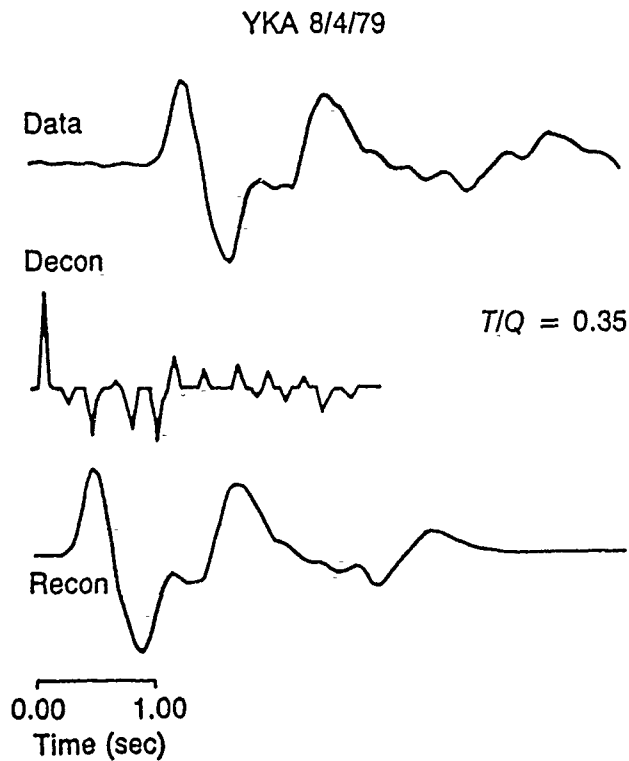


Figure 15. An example of L1 deconvolution of YKA broadband displacement data for a Shagan River event of 8/4/79. The deconvolved wavelet used has a $t^*=0.35$ and a von Seggern-Blandford time function. The resulting spike train is shown in the middle, and a reconstituted waveform is shown at the bottom. [From Mellman et al., 1985].

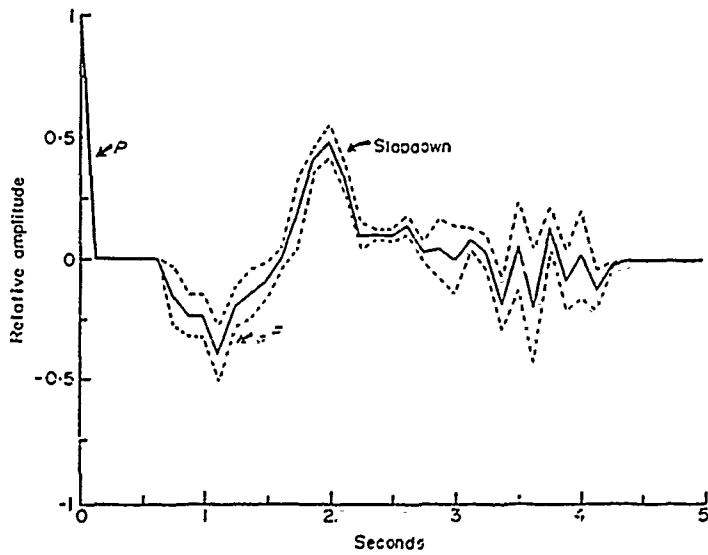
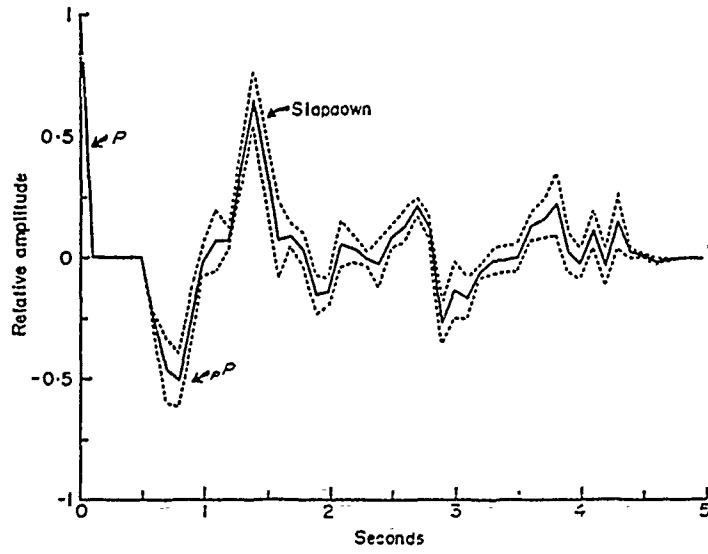


Figure 16. Mean impulse trains (solid lines) and standard deviation (dashed lines) obtained by averaging 4 impulse trains deconvolved from LRSM recordings for MILROW (top) and CANNIKIN (bottom). [From Bakun and Johnson, 1973].

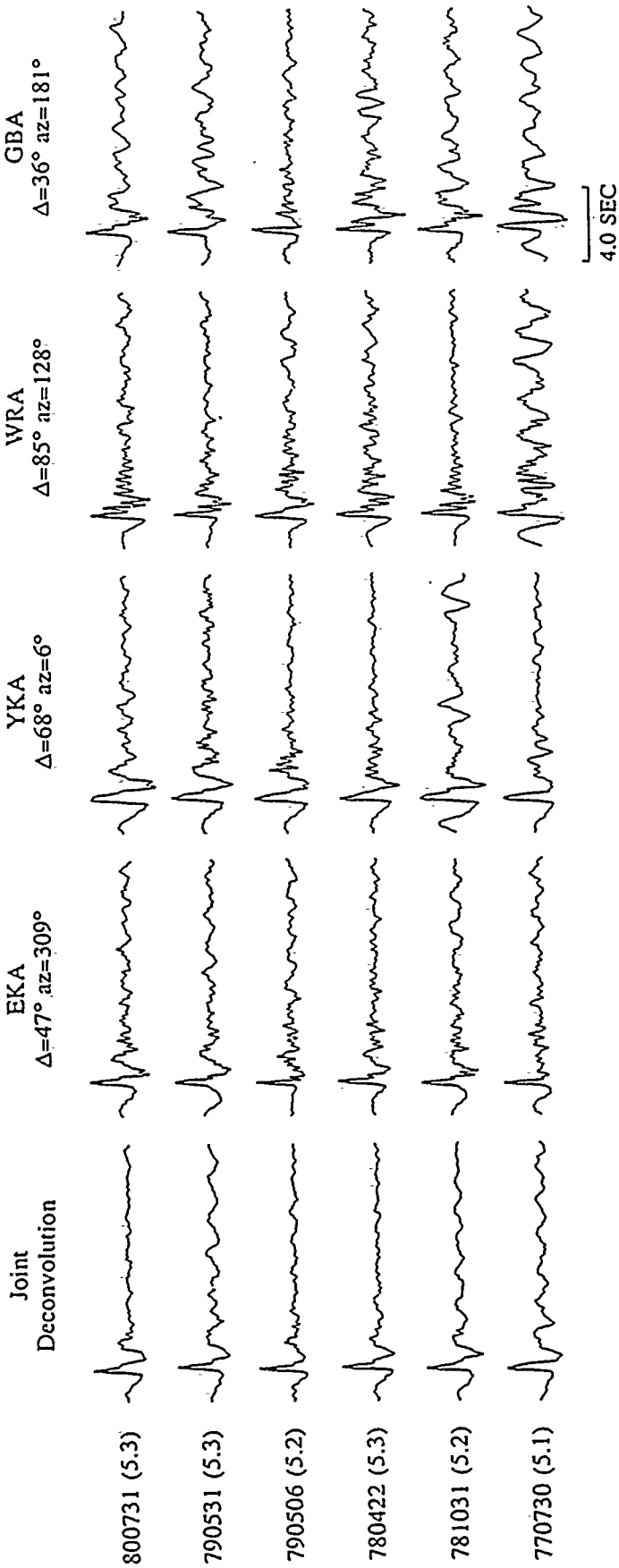


Figure 17. Source functions obtained by combined and individual array multi-channel deconvolutions for events at the Degelen test site [Der et al., 1987a] These functions should represent $E(t)*S(t)$ alone.

Deconvolved Source Functions
 EEKTS Events Recorded at EKA

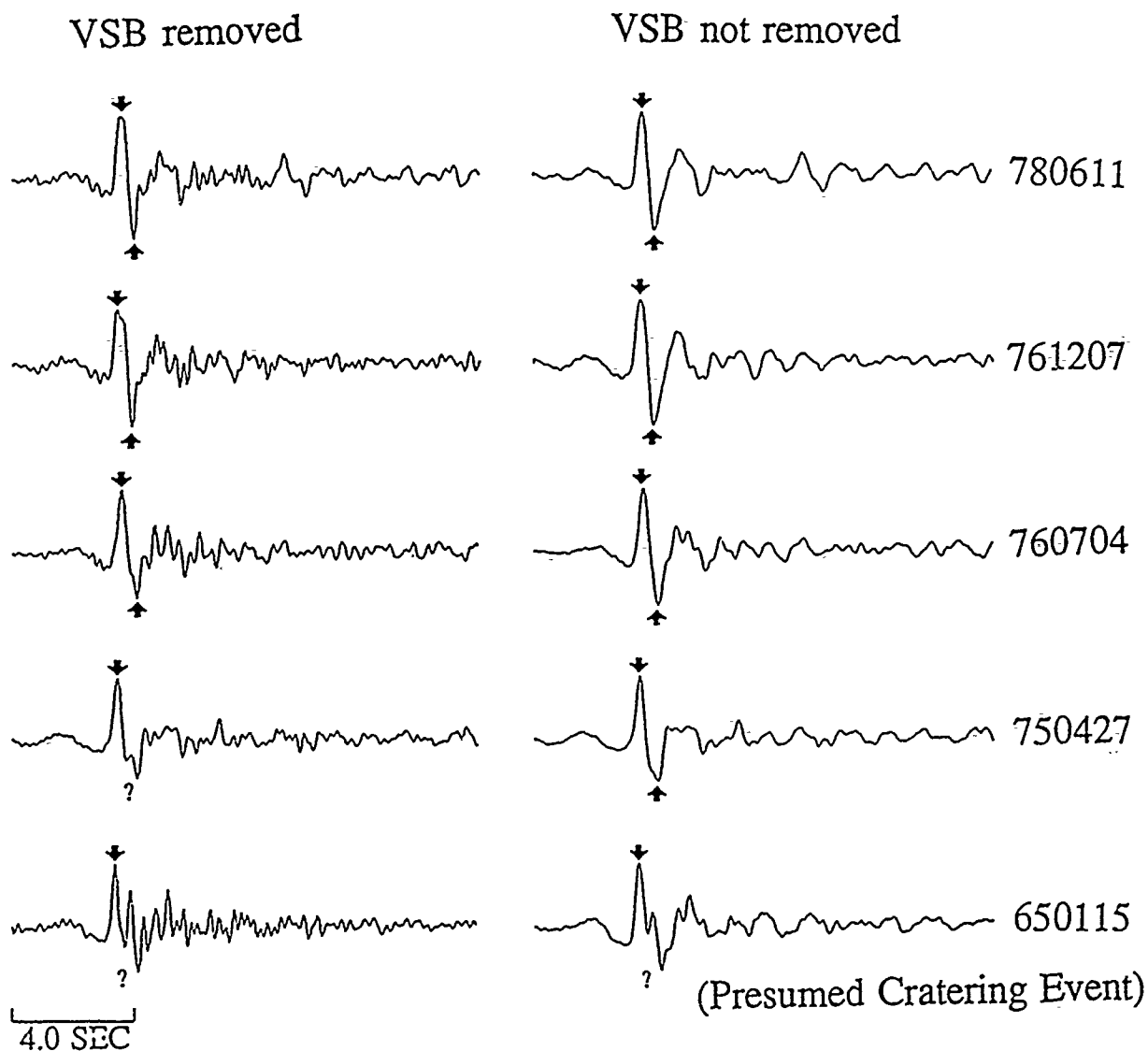


Figure 18. Source functions obtained by multi-channel deconvolution of East Kazakh explosions when the explosion source is removed, leaving $S(t)$ (left), and when it is not removed, leaving $E(t)*S(t)$ [Der et al., 1987a].

Deconvolved Source-Time Functions
NTS Events Recorded at NORSAR

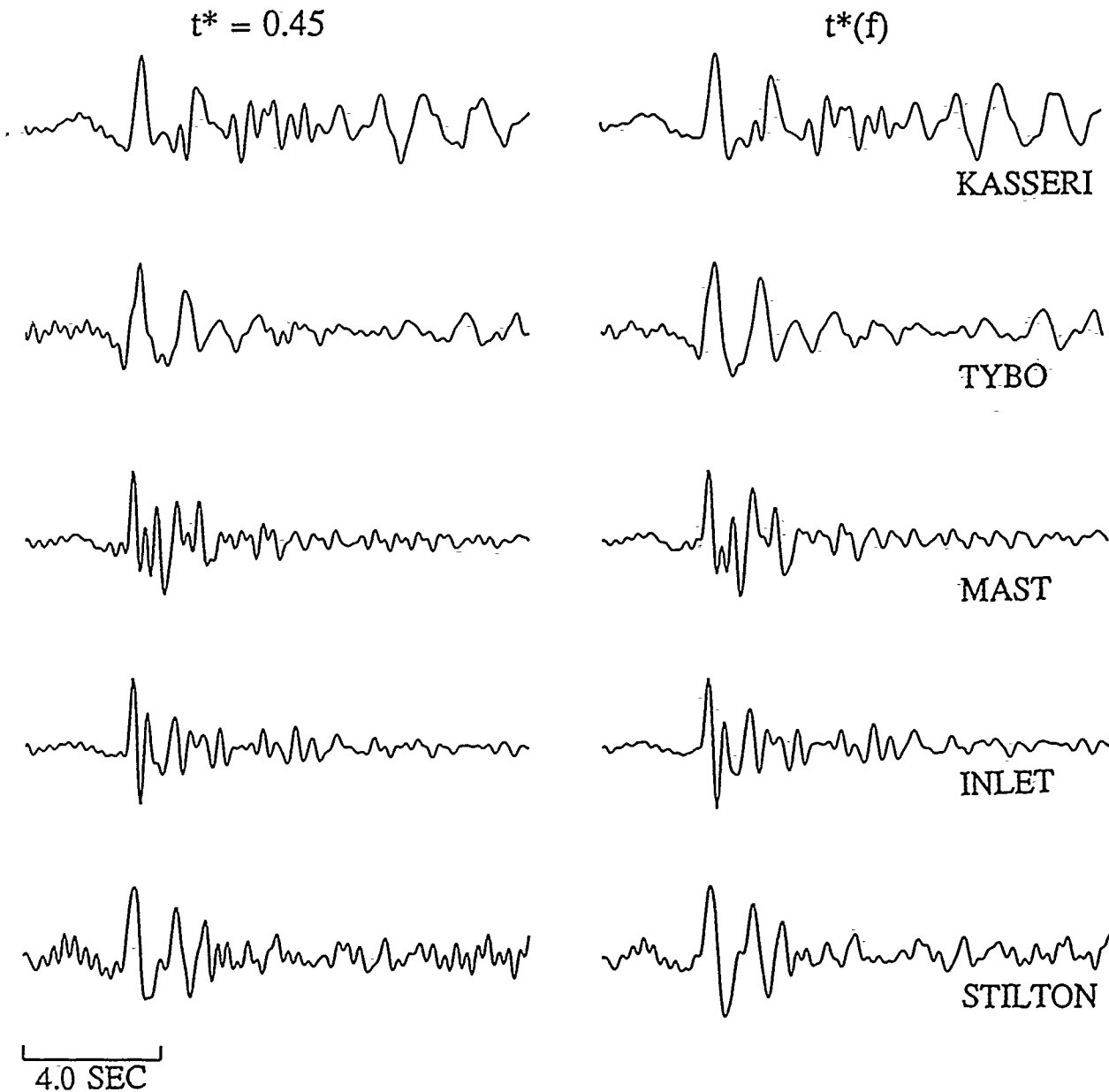


Figure 19. Source functions obtained by multi-channel deconvolution of Pahute Mesa (NTS) events for frequency independent attenuation (left) and frequency dependent attenuation (right) models [Der et al., 1987a].

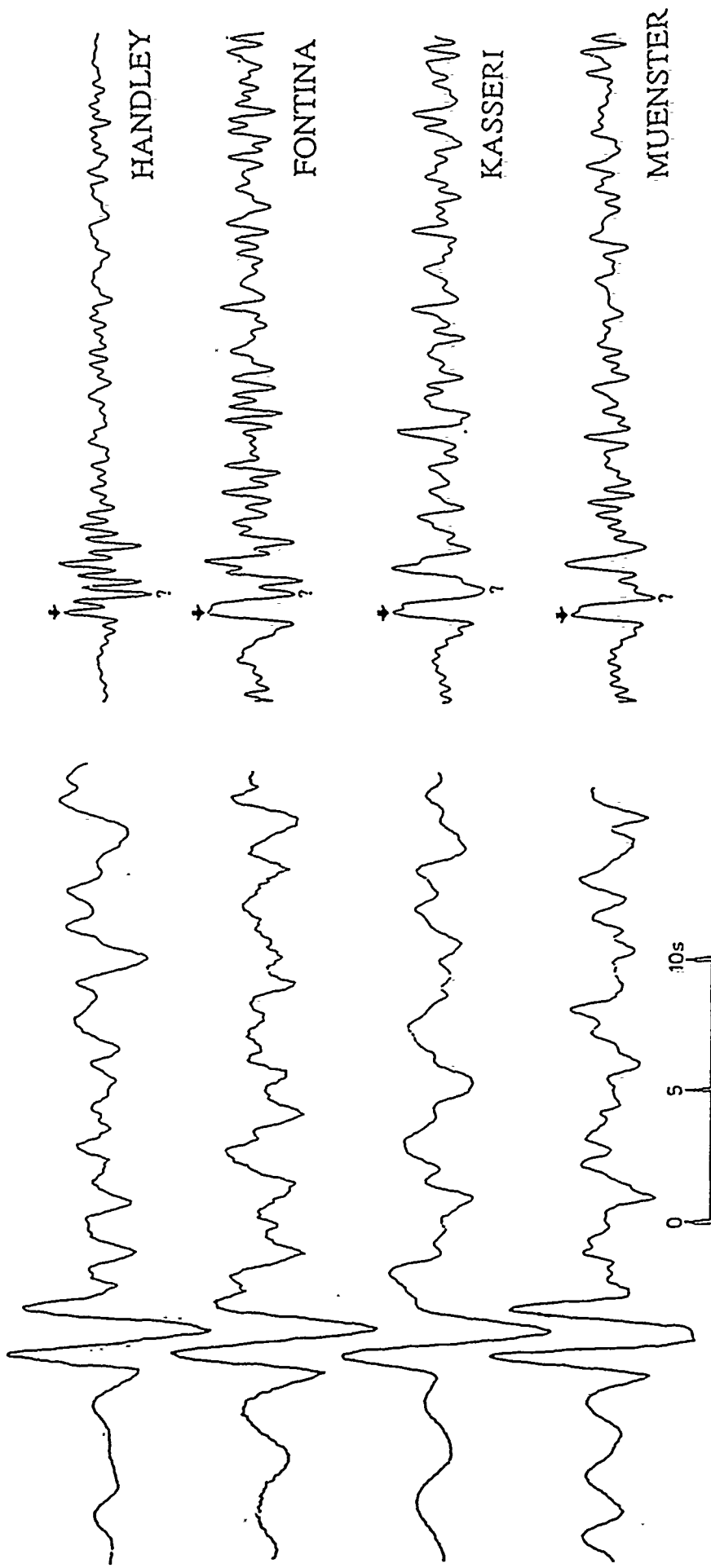


Figure 20. Comparison of source functions $[E(t)*S(t)]$ obtained by the ground motion restitution method of Lyman et al. [1986] (left) and the multi-channel deconvolution method of Der et al. [1987a] for four Pahute Mesa events recorded by the EKA array. The former method places greater weight on recovering the long period component, and does not factor out frequency dependent receiver effects.

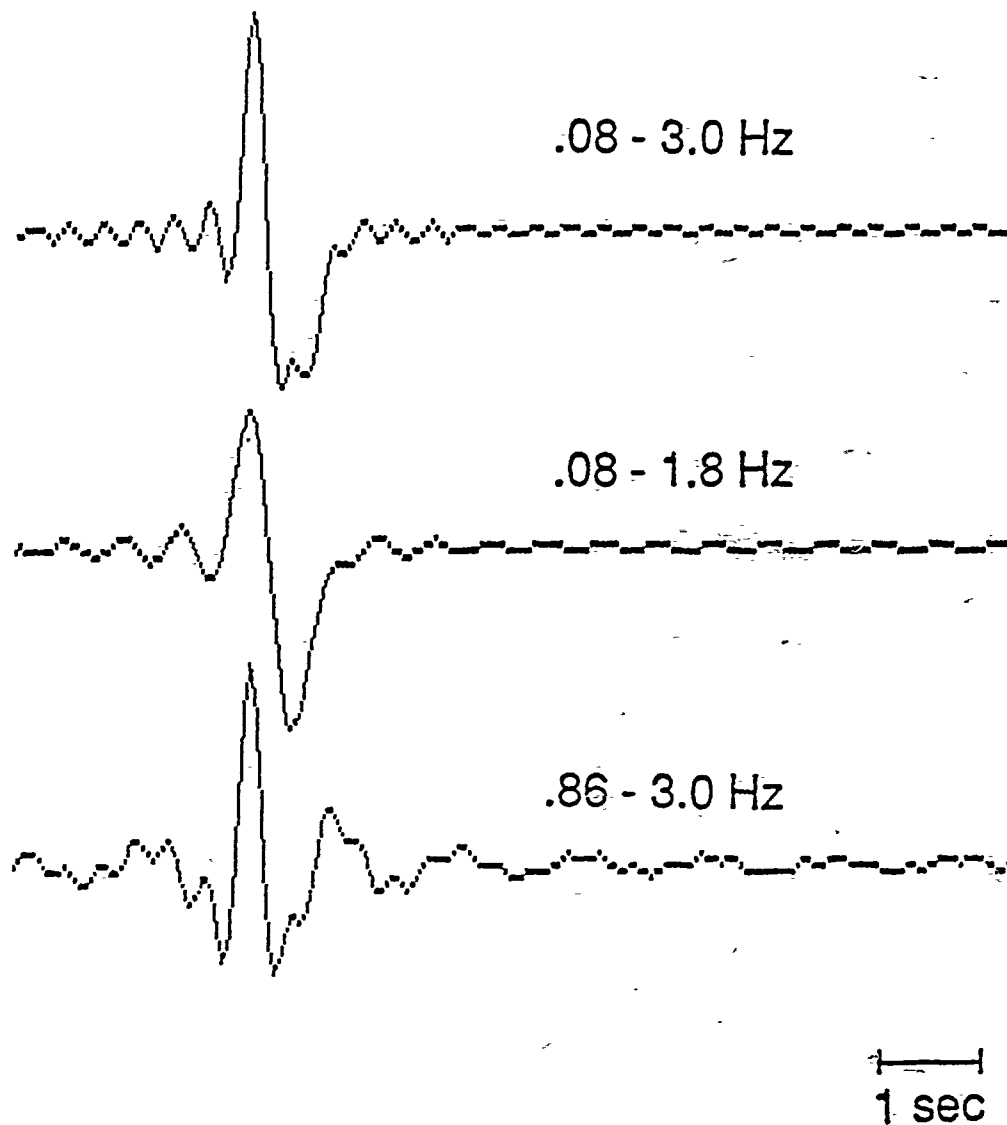


Figure 21. Bandpass filtered synthetic seismograms for an explosion signal with P and pP arrivals, with a frequency dependent pP reflection coefficient. Note how the apparent pP amplitude, indicated by the overshoot, differs depending on the frequency band of the trace. [Der et al., 1989].

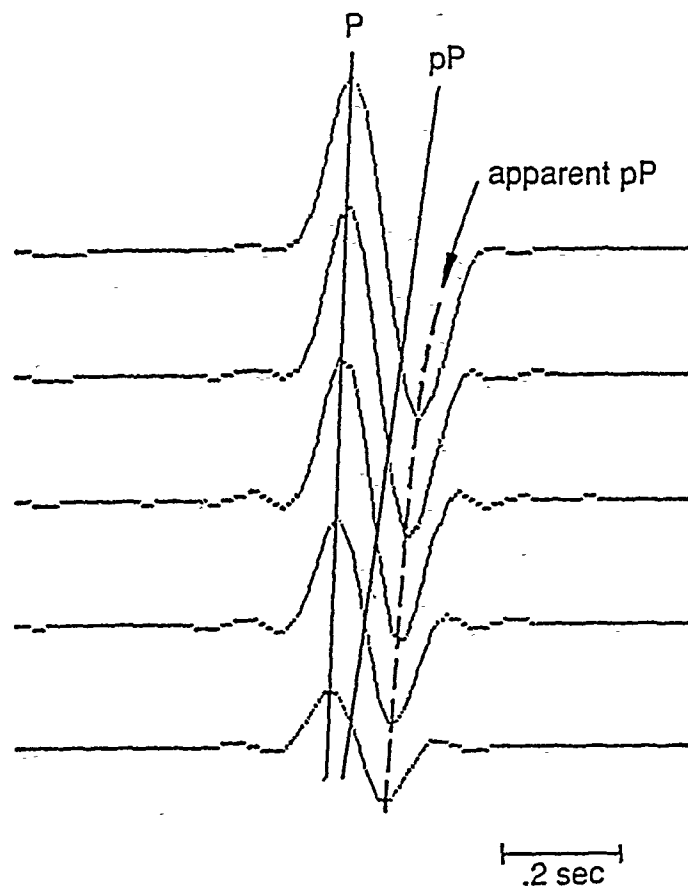
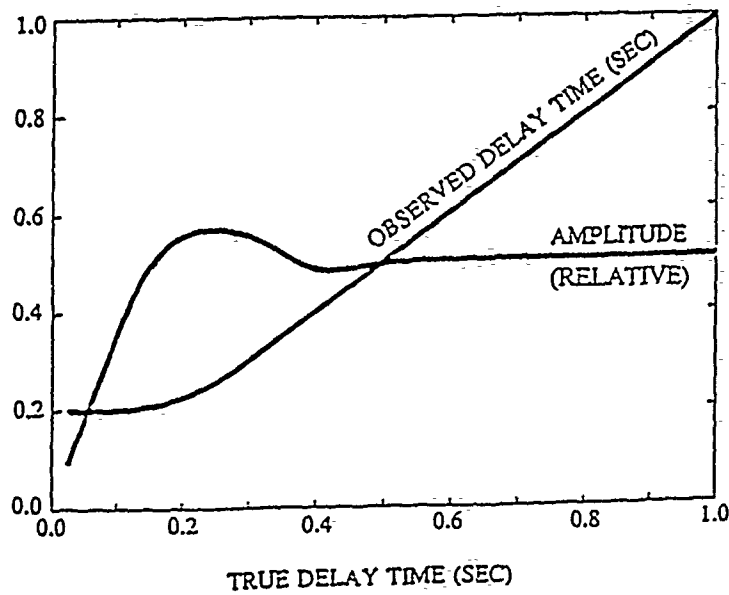


Figure 22. Demonstration of the biasing effect in pP lag time measurement for very short lag times with bandlimited data. The actual pP arrival times are shown by the solid line labeled pP, while the times inferred from the trough overestimate the true time. The effect on the peak to peak amplitude of the broadband data is shown at the top as a function of pP lag time as well. [Der et al., 1989].

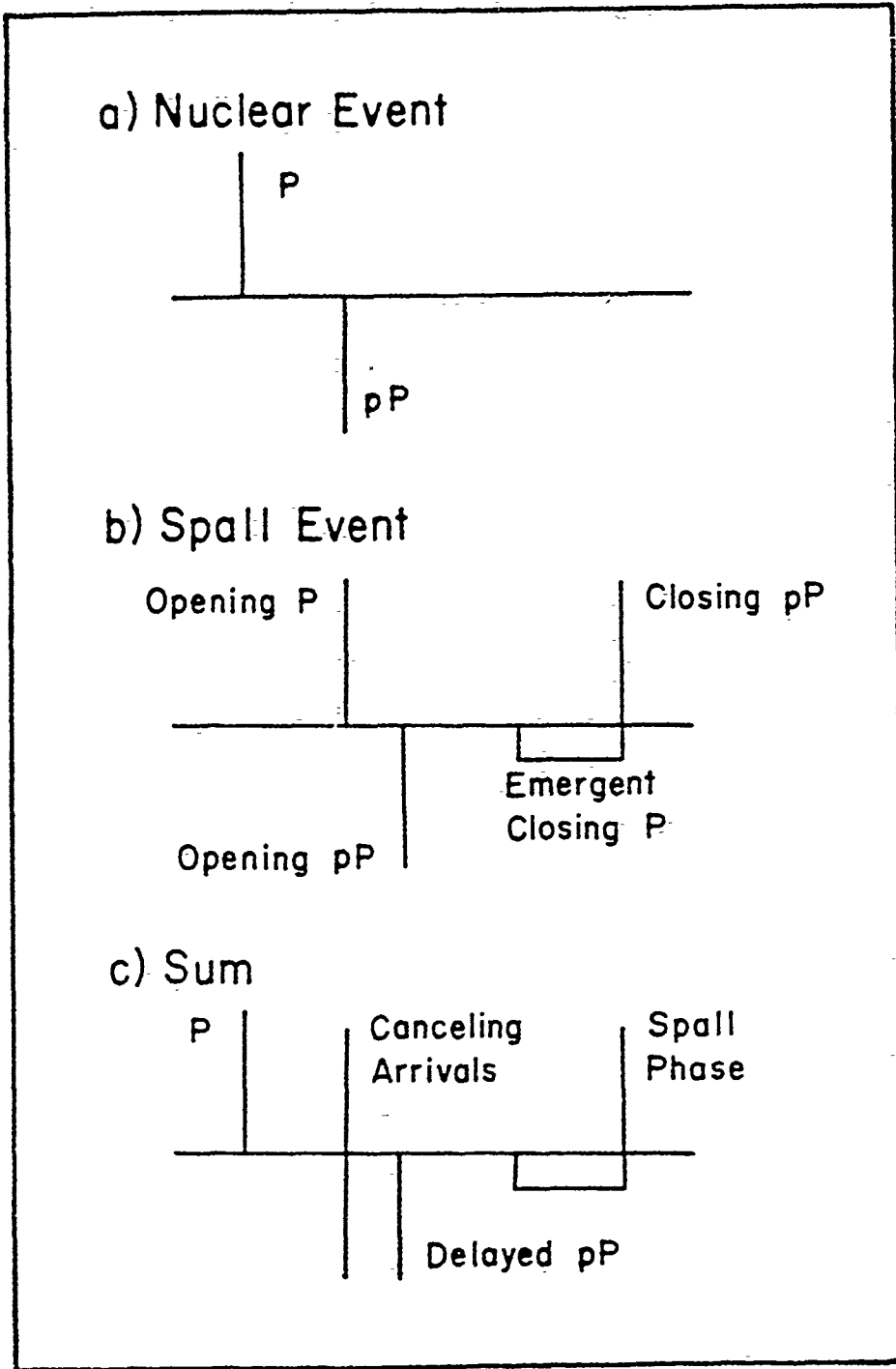


Figure 23. A simple, momentum conserving, phenomenological model for the coupled pP and spallation process. Opening and closing of the spall source, taken as either a tensional crack or a conical distributed surface, leads to additional arrivals at teleseismic distances. The spall opening arrival destructively interferes with pP, leading to anomalously late inferred pP arrival. The geometry of the closure process can concentrate the corresponding pP energy, producing the frequently observed teleseismic 'slapdown' phase. [From Burdick et al., 1984b].

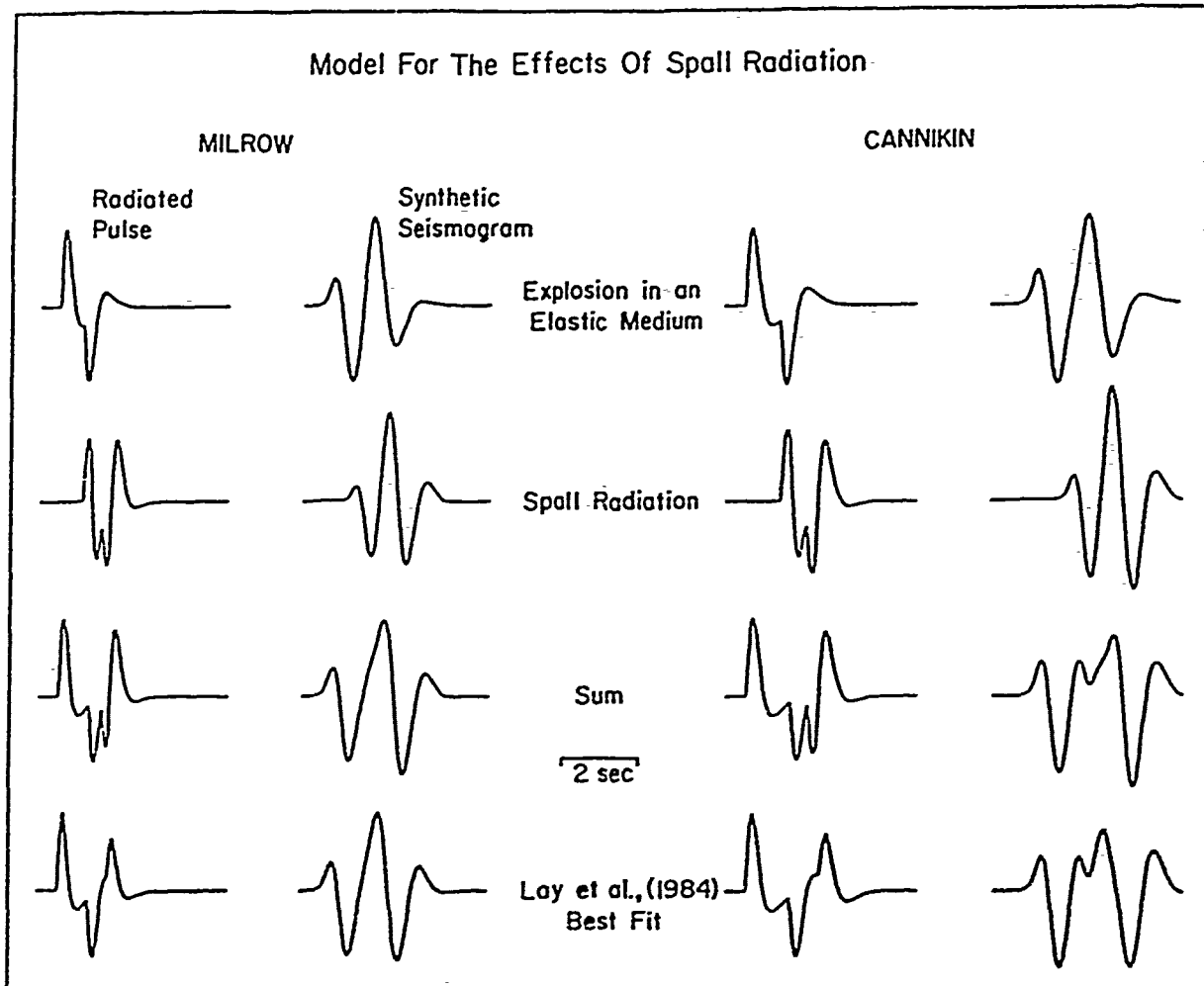
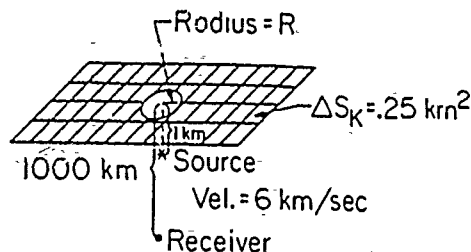


Figure 24. Application of the spall model in Figure 23 to the MILROW and CANNIKIN events. The predicted source functions and synthetic short period seismograms for the model are compared with the results of intercorrelation analysis of the actual data by Lay et al. [1984]. [From Burdick et al., 1984b].

$$x \leq R: \text{Refl. Coeff.} = \cos\left(\frac{\pi x}{2R}\right) - i$$

$$x > R: \text{Refl. Coeff.} = -1$$



WWSSN SYNTHETICS

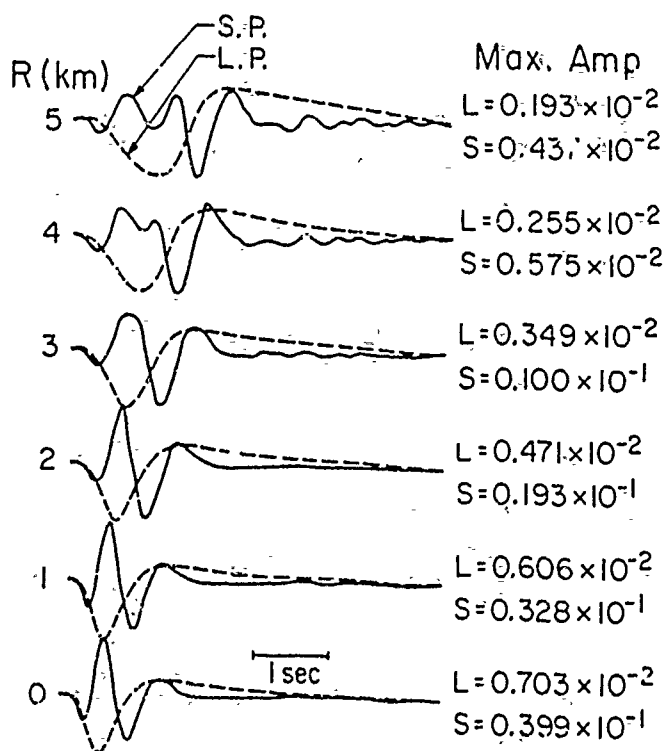


Figure 25. Simulation of a frequency dependent pP reflection from a free surface with spatially varying reflection coefficient using the Kirchhoff-Helmholtz approach. The short period and long period synthetics for varying radius of the anomalous reflecting zone are shown at the bottom. Note the systematic delay of the peak energy as the weakly reflecting region grows, and the rapid decrease in the amplitude of the short period reflection. [From Scott and Helmberger, 1983].

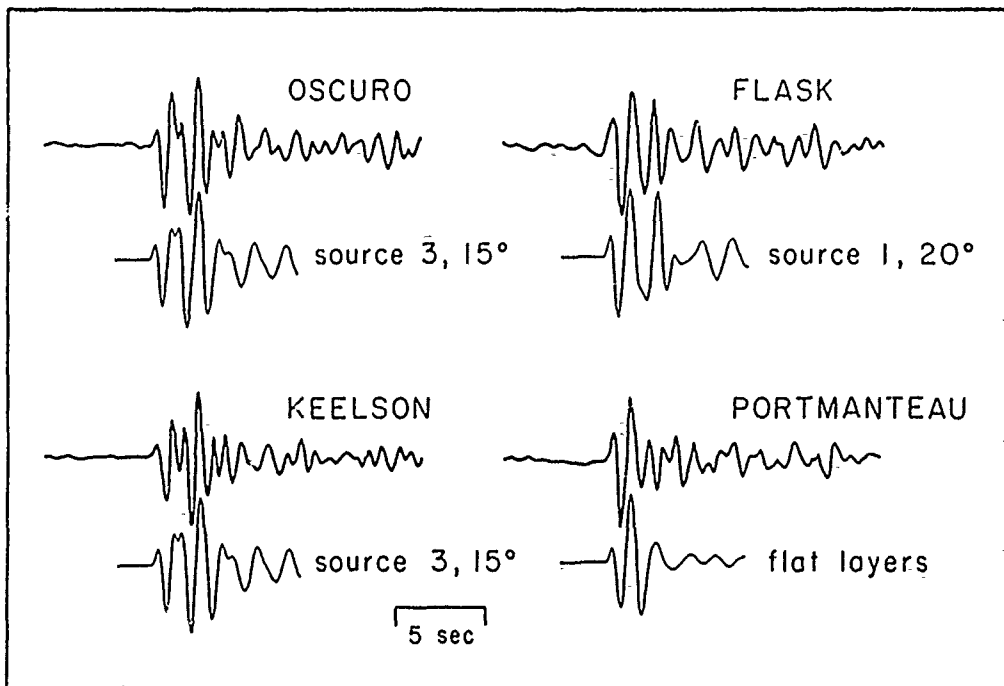


Figure 26. Results of a hybrid finite-difference-Kirchhoff method used to model explosions in the complex crustal structure at the Yucca Flat test site, compared with teleseismic observations at station MAT. Complexity of the basic interactions strongly affect the early part of the waveform where pP arrives, as well as the later coda. [From Stead and Helmberger, 1988].

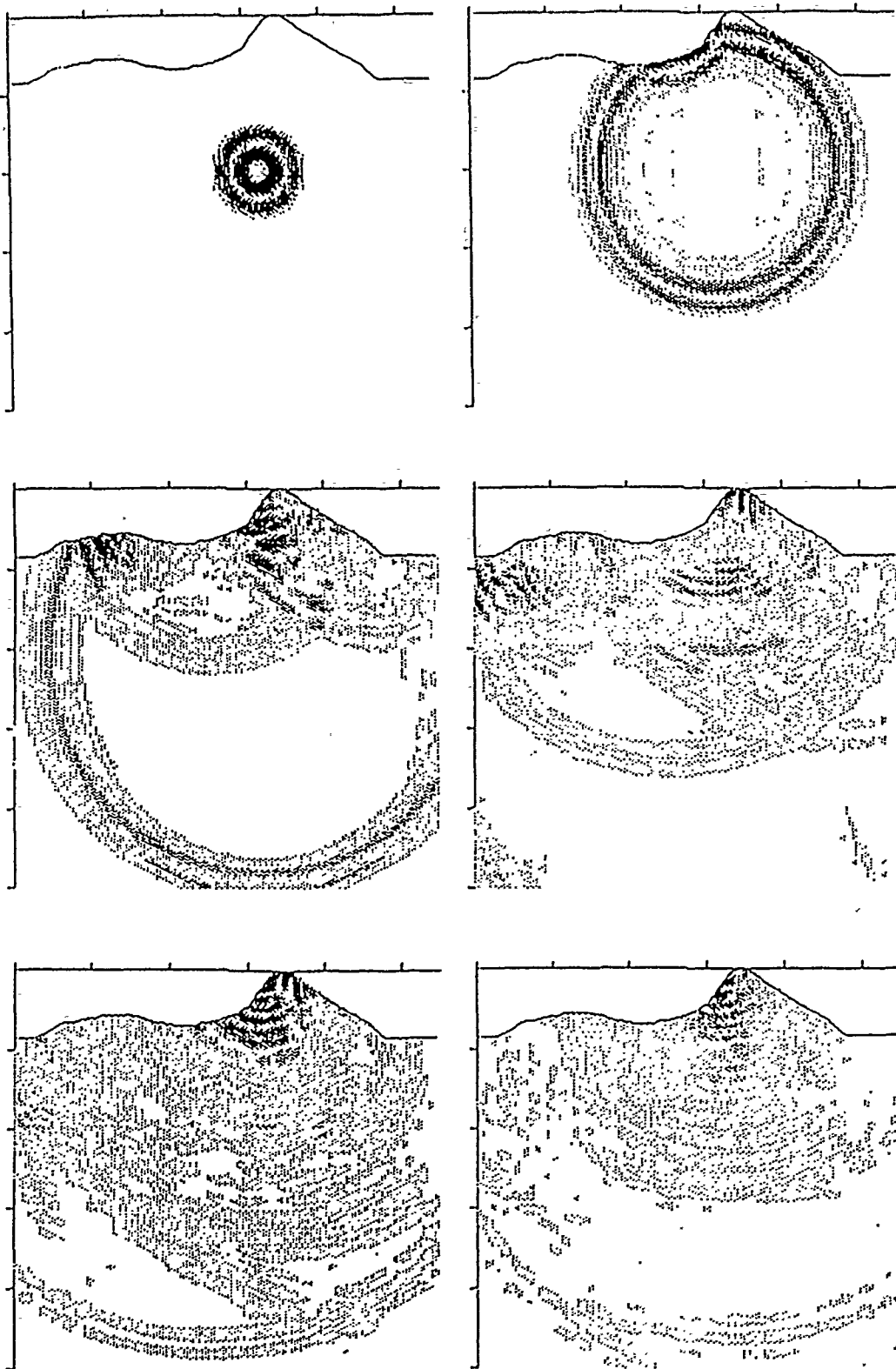


Figure 27. Two-dimensional finite difference calculations in different time slices for the explosion wavefield produced in a region of significant surface topography. Note the complexity of the pP reflection. [From McLaughlin et al, 1987].

Chapter 3
Nuclear Testing and Seismology
by
Thorne Lay

NUCLEAR TESTING AND SEISMOLOGY

T. Lay

University of California, Santa Cruz

- I. Introduction
- II. Seismic Waves from Underground Explosions
- III. Explosion Detection and Discrimination
- IV. Explosion Yield Estimation
- V. Nuclear Test Monitoring and the Earth System

GLOSSARY

Containment:	The procedures involved in designing underground nuclear tests to prevent release of radioactive material to the surface of the Earth.
Decoupling:	Reduction in seismic wave amplitudes for an explosion of a given yield produced by detonation in a pre-existing cavity.
Hydrodynamic Methods:	Procedures for estimating the yield of an explosion by recording the near-source shockwave in the ground surrounding the explosion.
Radiation Pattern:	The variation in amplitude and sense of motion over the surface of a seismic wave as it leaves the source.
Spall:	The parting of surface rocks above a buried explosion, produced when the tensional stress exceeds the rock strength. The rocks fly into the air during the ballistic period, followed by impact, or 'slapdown'.
Tectonic Release:	Release of earthquake-like seismic radiation produced by underground explosions, which may involve either a triggered fault, or relaxation of prestress in the rock around the shotpoint.
Yield:	A measure of the energy released in an underground explosion, usually expressed in kilotons (kt), with 1 kt = 10^{12} calories, or about 1000 tons of TNT.

Underground nuclear explosions produce seismic waves that propagate throughout the Earth, resulting in surface vibrations that can be detected by sensitive ground motion

sensors and used to locate the event. Seismic waves from explosions have characteristics that are distinctive from those of naturally occurring sources, such as fault motions, allowing all but the smallest explosions to be identified. The amplitude of the seismic waves provides a means for determining the yield of underground explosions as well. Thus, seismology, the study of seismic waves in the Earth, plays a vital role in monitoring and enforcing nuclear testing treaties, and seismic waves from nuclear tests have helped to reveal the internal structure of the planet.

I. INTRODUCTION

Detonation of an underground nuclear explosion produces elastic waves that transmit through the Earth's interior. These waves spread outward from the source, reflecting off of and transmitting across internal boundaries in the planet, with the wave motions eventually reaching the surface at different distances. The surface motions can be detected by seismographs, which are instruments that record the ground motion at a fixed location on the Earth's surface as a function of time. The seismic waves, along with procedures for their analysis developed in the field of seismology, provide a means for locating the source, for discriminating explosions from earthquakes, and for estimating the energy release, or yield, of the explosive device. Thus, seismology has played a critical role in the monitoring of global nuclear testing ever since the first underground nuclear explosion, RAINIER, was detonated in 1957. In addition, the seismic waves from explosions can be analyzed to reveal the deep structure in the Earth, from the crust to the core.

In 1963 the Limited Test Ban Treaty (LTBT) banned atmospheric, oceanic, and deep space testing of nuclear devices by all of its 116 signatory nations. This drove all nuclear testing by the United States and Soviet Union underground, greatly reducing the radioactive contamination of the Earth's atmosphere and surface that had initiated with the Trinity explosion in 1945. Figure 1 illustrates the history of nuclear testing programs. The great majority of explosions in the past 27 years have been conducted underground. The constraint of contained underground testing intrinsically imposes a limitation on the maximum size of nuclear devices that can be detonated, with the largest underground explosion (CANNIKIN, conducted by the U.S. in 1971), being a full order of magnitude smaller in yield [measured by kilotons (kt)] than the largest atmospheric test (Figure 2).

However, the devices that can be exploded underground are still vastly larger than the Hiroshima bomb, which has allowed the development of many new weapons systems.

Underground nuclear testing motivated the development of seismological techniques and instrumentation for monitoring foreign testing programs. The need to detect and locate events on a global basis brought about global deployments of standardized seismic instruments beginning in the 1960's and continuing today. These instruments include high quality observatories distributed around the world as well as localized dense arrays of stations for which the seismic signals can be stacked to enhance signal-to-noise properties. In addition, the need to distinguish earthquakes from explosions prompted the development and deployment of seismic sensors with very broadband sensitivity to ground motions, along with wide-spread deployment of sensors capable of recording three-component, rather than only vertical, ground motions. Many techniques have been developed to discriminate large explosions and earthquakes, and ongoing research is directed at discriminating small nuclear explosions from small earthquakes or chemical explosives used in quarry blasting.

With the signing of the Threshold Test Ban Treaty (TTBT) and the Peaceful Nuclear Explosions Treaty, both of which went into effect in 1976, the superpowers agreed to limit the maximum size of individual underground explosions to 150 kt (see Figure 2). Establishing compliance with this yield restriction has provided the additional task for seismology of reliably estimating the explosive yield of underground explosions. Increasing the accuracy of seismic yield estimation has required more than a decade of improvements in our detailed knowledge of how seismic waves are produced by explosions in different materials, and how they transmit through the Earth from different source regions. Until recently, the uncertainties in yield estimates have been substantial, and as a result, the 1976 treaties have not been ratified by the U.S. Senate as of July 1990, because it has been felt that they can not be adequately monitored. This perspective is now undergoing reassessment in the light of recent demonstrations of the accuracy of seismic yield estimates.

The technical requirements associated with nuclear test treaty monitoring have spurred on many fundamental advances in our knowledge of Earth structure and dynamics. The many seismic instruments deployed to record explosions have collected vast amounts of earthquake data, that have played a critical role in formulation of the theory of plate

tectonics. The seismic waves from both earthquakes and explosions have also been used to reveal the detailed seismic velocity structure of the planetary interior, from the variable thickness of the crust to the depth to the inner core, which, in turn, has been improved explosion monitoring capabilities.

The enforcement of existing test limitation treaties, and the negotiation of future, even more restrictive treaties, will depend heavily on the capabilities of seismology. Recent breakthroughs in the exchange of data between the superpowers, and the deployment of U.S. seismometers within the Soviet Union, have improved the seismological monitoring of very small explosions, reducing the technical obstacles to a very low threshold or a comprehensive (total) test ban. There is not yet a consensus in the seismological community as to the lowest yield for which seismic monitoring can presently be performed at high confidence levels, but estimates range from 1 to 30 kt, depending on various treaty evasion scenarios. The policy issue of whether further testing limitations are in the national interests of various superpowers is a complex topic which will not be addressed here, but enforcing any such measures will certainly depend heavily on the basic aspects of nuclear explosions seismology described below.

II. SEISMIC WAVES FROM UNDERGROUND EXPLOSIONS

The material properties of the Earth are such that any transient source of deformational energy, either natural or man-made, can excite propagating elastic disturbances, or seismic waves, in the interior. Sudden sliding of a buried fault releases stored deformational energy in the rock around the fault, producing waves that spread spherically away from the source, eventually shaking the surface as an earthquake. Small explosions, and heavy vibrating trucks are used in the oil industry to excite seismic waves which travel downward and reflect off of rock layers in the crust, thereby revealing the crustal structures that may contain oil or gas. Underground nuclear explosions suddenly create a cavity in the ground filled with hot gasses which apply a spherically symmetric pressure pulse to the rock. The sudden application of the pressure force excites seismic waves, which transmit through the interior. In addition to these sources, there are many other processes which generate seismic waves, such as wind, tides, landslides, traffic, and magma motions in volcanoes. The resulting vibrations establish a background noise level, which is highly variable from place to place, against which the motions from a distant nuclear explosion must be detected.

For an elastic body, there are two fundamental types of wave disturbances that travel within the medium; P waves and S waves. The particle motions associated with these body waves are shown in Figure 3. P waves travel fastest, about 6 km/s in the crust and more than 8 km/s in the upper mantle. They involve volumetric compression and dilatation in the direction of propagation as the P wave passes by, while the slower S waves (with velocities of about 4 to 5 km/s) produce shearing motion in a direction perpendicular to the propagation direction. The relative degree to which P and S waves are excited, and their sense of initial motion depends on the type of source producing the waves. When P and S waves interact with the Earth's free surface and the low velocity layers near the surface, they can produce traveling surface disturbances called Rayleigh and Love waves, which propagate with velocities of about 3 to 4 km/s. Rayleigh waves travel slower than both S waves and Love waves, and involve elliptical ground motions which are strongest on the vertical component. Love waves result from horizontally polarized S waves that reverberate in low velocity near-surface layers. Both types of surface wave are dispersive, with different frequency components traveling at different phase velocities controlled by the variation of material properties with depth, and their amplitudes are usually larger than the body waves because the energy is distributed over a two-dimensionally expanding wavefront rather than a spherical wavefront.

The radiation of body and surface waves from a source depends on the strain geometry and time history of forces at the source. An explosion involves primarily outward compressional motion, with spherical symmetry (Figure 4). Thus, explosions preferentially generate P wave energy, distributed over an expanding compressional wavefront, with S waves ideally arising only by conversions of P wave energy at the Earth's surface or at internal boundaries. Rayleigh waves with a symmetric initial radiation pattern are produced as well, but Love waves are not produced by a symmetric explosion, since there is no sense of horizontal shearing motion at the source. In reality, departures from spherical symmetry of the cavity, crustal structure heterogeneity, and triggered release of tectonic stress on nearby faults or in the rock around the cavity can produce both S wave radiation and Love waves from an explosion source.

Earthquakes produced by shearing motion of crustal masses on faults (Figure 4) intrinsically generate relatively strong S waves, including transverse horizontal motions that generate Love waves. Shallow earthquakes are much more efficient at generating strong

surface waves than are underground explosions. The asymmetry in strain due to shear fault sources causes the P and Rayleigh wave radiation patterns to have quadrupolar variation in initial motion distributed over the corresponding wavefronts, with alternating first motions toward or away from the source. Given a good distribution of recording stations, the fault orientation can be determined from the systematic variation of body and surface wave motions with respect to the fault, after correcting for any propagation effects.

The theory of elastodynamics is used in seismology to understand the excitation and propagation of waves in an elastic material. If the material properties of the medium are known, it is possible to compute the wavefield that will be excited by internal or external force systems. An underground explosion can be modeled as a uniform pressure applied to a cavity in the medium, or alternatively, as a system of three orthogonal dipole forces (Figure 4) in a homogeneous medium. Figure 5 shows observed surface ground motion recordings from close-in distances for a large underground explosion, along with synthetic motions comprised of an initial high frequency P wave arrival, followed by a longer period Rayleigh wave. Matching observed waveforms with synthetic seismograms provides a means for characterizing the source; usually a parametric representation of the pressure function time history is adopted for the modeling. Application of modeling procedures to events with a wide range of yields has led to the development of scaling laws that describe how the frequency spectrum of explosion or earthquake radiation varies with strength of the source.

Examples of theoretical amplitude spectra for such 'seismic source models' are shown in Figure 6. These spectra indicate the relative amplitude of source radiation for different frequency seismic vibrations. The low frequency explosion strength increases in direct proportion to the yield, for a homogeneous medium, and there may be an overshoot, or peaking, of the source spectrum preceding the high frequency drop-off in spectral amplitude. The overshoot may result from peaking of the pressure function in the source cavity followed by partial rebound of the cavity or dissipation of gas pressure. There is uncertainty in the precise nature of high frequency radiation from explosions, as indicated by the differences between the two explosion source models shown in Figure 6. Earthquake spectra do not show significant peaking, and may have different 'corner' frequencies (the frequency where the high frequency decrease in spectral level begins) than for explosions with the same long period spectral levels. Differences in these source

spectra, combined with differences in radiation pattern and propagation effects result in diagnostic signal characteristics that can be used to identify underground explosions.

Seismology uses a variety of measures of seismic waves to characterize the sources, with the most common being magnitude scales. These are logarithmic scales based on the amplitude of ground motion at a particular frequency for a given wavetype. The observed values are equalized to a common distance by correcting for geometric spreading of the wavefield as well as for anelastic losses that result from frictional heating as the wave travels through the rock. Two magnitude scales are particularly common for explosions, the body wave magnitude, m_b , based on the amplitude of 1 s period P wave signals at teleseismic distances (more than 3000 km from the source), and the surface wave magnitude, M_s , based on 20 s period Rayleigh waves. Figure 6 indicates that M_s is likely to directly reflect the event yield, while m_b may be affected by overshoot as well as by variations in the source corner frequency. A 1 kt explosion produces an m_b of about 4.0 ± 0.3 , while the approximately 4400 kt explosion, CANNIKIN produced an m_b of about 6.9, along with an M_s of about 5.7. The number of observations available for estimating a magnitude clearly decreases for the smaller events. For example, it is difficult to measure M_s values of less than about 3.5 (yield of about 10 kt) due to the very low Rayleigh wave amplitudes. Magnitudes are intrinsically relative amplitude measures, with the significance of the absolute level of the magnitude depending on calibration with respect to independent measurement of the associated source energy release.

Both empirical and theoretical investigations of nuclear explosion source functions have shown that the coupling of energy into the seismic wavefield varies with the source emplacement medium. This is illustrated by the variation in source spectra for a given yield event shown in Figure 7. Of the total energy release in an underground explosion, only from 0.1 to 1% is converted into seismic wave energy, with the remainder being converted to heat and deformation of the explosion cavity and surrounding rock. The percentage of seismic wave energy relative to the total energy is called the seismic efficiency. Generally, harder, more competent rocks have a higher seismic efficiency, as well as producing a greater proportion of high frequency seismic energy. This becomes an important issue for seismic yield determination, as independent information on the rock types at a suspected explosion source site must be available if accurate yields are to be determined. For some materials, such as salt or alluvium, the medium profoundly reduces the seismic radiation

causing much larger events to produce the same magnitude as a smaller event in harder rock. While numerical models of coupling variations among different rock types are quite successful, actual detonations in a variety of media have been performed to quantify the coupling effects.

III. EXPLOSION DETECTION AND DISCRIMINATION

Monitoring of global nuclear testing requires automated procedures for detecting and locating all major sources of seismic waves, and for distinguishing between earthquakes and nuclear explosions. Seismic waves spread in all directions from a source, but the amplitude of the ground vibrations decreases with distance due to geometric spreading of the fixed amount of energy being distributed over the expanding wavefront, as well as due to anelastic losses associated with the imperfect elasticity of Earth materials. Given the many sources of background noise in the ground motions at any given site, all stations have a detection threshold below which they do not provide useful data. At least four unambiguous arrival times with good distribution around the source are required to solve for the location and origin time of an event. Thus, there is a lower limit to the source size in a given region for which all events can be detected. There is an even higher minimum magnitude for having sufficient wavefield information to discriminate nuclear explosions from natural sources or quarry blasts.

Monitoring nuclear testing in a vast country like the Soviet Union is a major challenge. Figure 8 shows the widespread distribution of presumed underground nuclear tests that have been conducted in this region. The majority of tests have been located at the main test sites in Novaya Zemlya, Semipalatinsk, and Azgir, just as the majority of U.S. tests have been at the Nevada Test Site, but many other explosions, often involving large scale excavation applications of the Peaceful Nuclear Explosion program, have taken place at scattered locations across the country. Many of these areas lack background seismic activity, as shown in Figure 9, so almost any detected event may be suspected. However, for areas with frequent earthquake activity, which are the likely locations of any efforts to conduct clandestine testing, seismologists must locate all earthquakes as well as all explosions, and find ways to tell them apart.

Given a global network of seismic sensors, such as presently exists, it is believed that almost all events with m_b greater than 4.0 can be detected across the Soviet Union. To

significantly reduce this threshold, data from stations within the country are desirable. For a combined network of global and 30 internal Soviet stations, the event detection limit can be pushed down to an m_b of about 2.0 (Figure 10), which would provide detection for well-coupled events with yields that are only a fraction of 1 kt. The detection capability can also be improved by using seismic arrays, which suppress background noise by stacking the signals. Modern seismic arrays located at quiet sites outside of the Soviet Union can achieve detection thresholds as low as an m_b of 2.0, for extensive portions of the country. The primary motivation for lowering the detection threshold involves the possibility of decoupling an explosion by detonating it in a pre-existing cavity or in weak salt or alluvium, which can greatly reduce the amplitude of seismic waves that are generated. There are also difficult issues in discriminating very small explosions from other sources. There are more than 7500 globally distributed earthquakes each year with magnitudes greater than 4.0, and around 50,000 each year with magnitudes from 3 to 4, taxing any networks' ability to detect and locate all events.

Once an event is detected and located, it must be identified as an explosion or not, with high confidence. Unless the event is clearly at too large of a source depth to possibly be an explosion, or located under the ocean, this requires a diagnostic characteristic of the seismic wavefield. Even determining the source depth requires waveform information if the event is shallower than about 30 km, given limitations in depth determination using travel times alone. For large events, the discrimination procedure is rather straightforward, and primarily relies on the difference in excitation of surface waves and high frequency P waves between explosions and earthquakes. Figure 11 compares long period seismic recordings on a common scale for an earthquake and an explosion. The earthquake produced much stronger surface waves, a clear S wave, and a relatively long period P wave, compared with the explosion, despite the higher m_b of the latter event. Comparison of the m_b and M_s measurements can separate populations of earthquakes and explosions (Figure 12), with high confidence for all but the smaller events, for events large enough to produce measurable M_s .

The differences in source radiation patterns and source spectra between explosions and earthquakes can be exploited in a variety of other discrimination procedures. Observation of quadrupolar body and surface wave radiation (i.e. alternating motions toward or away from the source) can identify an earthquake, although care must be taken to account for

tectonic release effects triggered by an explosion. Tectonic release can produce signals that are very similar to an earthquake (Figure 12), as well as biasing the magnitudes that are measured for the event. The effects of tectonic release are usually assessed by analyzing the Love waves and azimuthal patterns in the Rayleigh waves. For some source regions, explosions are found to generate more high frequency body wave radiation than a comparable size earthquake, so frequency dependent body wave magnitude measurements have also been used for discrimination.

Discrimination becomes increasingly difficult for smaller events, mainly due to the low signals amplitudes and increased high frequency scattering effects on the seismic wavefield. Seismic observations at regional distances, out to 1500 km, are dominated by complex arrivals that reverberate in the crust, and propagation effects can obscure the source characteristics. Systematic differences in the spectral content of various regional phases are being examined in order to improve low yield discrimination capabilities. One area of progress is in distinguishing ripple-fire quarry blasts (which involve a sequence of explosions) from nuclear tests, using spectral modulations arising from lag between the quarry blast charges.

IV. EXPLOSION YIELD ESTIMATION

Seismic waves transmit through the Earth with predictable decreases in amplitudes and other fairly well understood propagation effects, which makes it possible to relate measured seismic magnitudes such as m_b or M_s to the strength of the explosion source as long as the absolute level is independently established. This is most reliably done by determining a magnitude-yield calibration curve, based on events with known yields in a uniform source medium. Nuclear devices are very complex, and often experimental, so the theoretical yield is typically not very reliable. Actual explosion yields can be accurately measured by several methods, including hydrodynamic techniques that record the shock wave velocity in the rock around the source, or by radiochemical techniques that involve drilling back into the source region and examining the radioactive products of the explosion. Some official yield estimates have been released by both the U.S. and the Soviet Union, and of course there are many classified determinations by both countries. These yields can be combined with the measured magnitudes to establish magnitude-yield calibration curves.

Once a magnitude-yield curve is determined for a given source region, the yield of a new event in that region can be estimated based on its magnitude, as shown in Figure 14. The data used to define the calibration curve always exhibit some scatter about the best fitting curve, which provides a statistical bound on the uncertainty in the yield estimate expected for the new event. The scatter is primarily the result of local scale variations in coupling, focussing and defocussing of the seismic radiation, and actual measurement uncertainty due to noise at the sensors and variation in the available seismic data set. For P waves, the amplitude variations due to shallow crustal structure variations can be very pronounced, even among closely spaced sensors (see Figure 15). This requires that the magnitude determination include a large number of observations with corrections for systematic station patterns. In addition to the seismological scatter, there is some uncertainty (<30%) in the yield determinations by the hydrodynamic and radiochemical procedures. For many years, seismic yield estimates were given a "factor of two" uncertainty, meaning that the assigned yield had a 95% chance of being within a factor of two of the actual yield. But this uncertainty factor was contingent upon the transportability of calibration curves between test sites, which was not clearly demonstrated to be valid.

The need for high confidence in yield estimation is indicated by Figure 16. The body wave magnitudes for Soviet underground tests are shown as a function of time. Note that the largest tests were conducted at the Novaya Zemlya test site prior to the Threshold Test Ban Treaty in 1976. After 1976, the largest magnitudes were less than 6.0 for several years, followed by an apparent increase in the maximum event magnitude to about 6.25. The obvious question is whether the 150 kt limit is at a magnitude of 6.0 or 6.25. If it is the former, the Soviet testing program would appear to be systematically violating the TTBT, as was the contention of the Reagan administration during the early 1980's. Furthermore, even an m_b value of 6.0 would correspond to an explosion with a yield above 300 kt at the Nevada Test Site. Lacking a calibration shot, or series of shots, at a Soviet test site, seismologists must determine what magnitude-yield curve to use to estimate yields for the Soviet explosions.

As shown earlier, the efficiency of seismic wave excitation is dependent on the properties of the source medium, so it is important to have information about the type of rock in which the explosion is detonated. This can often be determined from large scale geological features in the source area, which can be appraised by satellite imaging. To a

certain extent the source medium can also be inferred from the spectral characteristics of the seismic signals; harder rock source regions tend to more efficiently couple high frequency energy into the seismic wavefield. An additional consideration is the characteristics of the crust and upper mantle structure near the source region. If the upper mantle is anomalously hot, all of the downgoing P waves that are used to compute m_b , may be attenuated, resulting in low magnitudes (Figure 17) relative to the same yield explosions at other sites. Unless calibration events are available for the site, or the degree of attenuation is independently determined, this can lead to underestimating the yields when using the calibration curve for another site.

It is now widely accepted that the m_b -yield relation for the main Soviet test sites are significantly shifted relative to the curves for the Nevada Test Site, even after allowing for differences in source rock types. This is due to the strong attenuation experienced by the P waves as they traverse the mantle under the Nevada Test Site. As a result, the same size explosion, in the same rock type at the two sites will produce m_b values that are 0.3-0.4 magnitude units lower for the Nevada source region (Figure 17). This baseline shift in the m_b -yield curve has been strongly debated, and a variety of seismological procedures have been introduced to establish the precise value of the shift.

Comparison of different magnitude scales is one procedure for establishing the m_b -yield baseline shift between test sites. Figure 18 shows how a plot of M_s versus m_b suggests that an m_b shift of 0.35 magnitude units is required to bring Nevada explosion observations into general agreement with the data for the U.S. test site on Amchitka Island and the Novaya Zemlya data. Surface waves are less affected by the highly attenuating material in the upper mantle under the western United States, so M_s should not be shifted relative to other regions as much as m_b . Surface waves may be strongly affected by tectonic release, so care must be taken to avoid events with contaminated surface waves, or corrections must be applied to remove the effects of tectonic release for this procedure.

Other procedures, such as determining the degree of attenuation of the P wave spectrum can be used to estimate the variation of site effects on magnitudes. Of course, the most direct method is to accept at face value the released yields for foreign events, and to compare magnitude-yield curves between sites. This encounters many objections due to the unverifiable nature of the released yields. Ultimately direct calibration of the test site is

the most convincing way to establish the absolute baseline for the magnitude-yield relation, but this requires direct measurement of the yield on the foreign test site.

Direct calibration has been discussed for many years, but only became a reality with the Joint Verification Experiment in 1988. The JVE involved the detonation of one explosion in Nevada, and one in the Shagan River, U.S.S.R. test site, with hydrodynamic techniques being applied by both countries for both events. This remarkable exchange came only two years after the Soviet Union first permitted the deployment of U.S. operated seismic recording equipment in the Soviet Union. The magnitude-yield point for the JVE explosion can be used to set the baseline of a hard-rock yield scaling curve, which would be appropriate for the Shagan River test site. One such curve is shown in Figure 19, where the U.S. hard-rock data have been shifted to correspond to the expected Soviet site baseline. The break in slope of the m_b -yield curve is a natural result of the 1 Hz spectral scaling of explosion source functions, as shown in Figure 6, in combination with the effects of increasing burial depth with increasing yield and interference with reflections from the free surface. While the precise curve to use for yield prediction around 100 kt is ambiguous, the actual JVE point plots directly in the middle of the expected values, indicating how accurately the yield was estimated using only seismological means. Note that the 150 kt yield should have an m_b of about 6.2. Using an unbiased m_b -yield calibration curve results in the yield estimates for Soviet explosions shown in Figure 20, which suggests that there has not been a systematic violation of the TTBT. Full confidence in the yields over the entire magnitude range requires additional calibration events for a range of yields, but the seismic methods have been demonstrated to be remarkably accurate for yields above 10 kt, now that the differences between sites have been recognized and well determined.

Given the interest in negotiating more restrictive testing limitation treaties, it has become important to improve the yield estimation accuracy for very small events. Small events are best observed at near-by stations, a possibility given the recent deployment of U.S. stations within the Soviet Union. However, at regional distances less than 1500 km the character of the seismic wavefield is greatly complicated by crustal reverberations. The relative complexity of regional and teleseismic distance waveforms is illustrated by Figure 21. The P_n and S_n phases are apparent at regional distances, and correspond to body waves that travel along the crust-mantle boundary, while P_g and L_g are reflections and multiple

reverberations from crustal discontinuities. Compared with the simple P waveform at larger distances, it appears that regional phases might be less accurate for yield estimation, but actually this has not proven to be the case.

Given accurate geometric spreading and attenuation corrections, a seismic magnitude scale can be determined for almost any seismic phase, including those at regional distances. The L_g phase has proven particularly useful, for magnitudes based on this phase exhibit very little scatter when magnitude-yield curves are determined. Figure 22 shows the potential of regional phase magnitudes for yield estimation, for the Nevada Test Site. Just as for m_b , events in different source media (such as granite, compared to the normal NTS tuff), have a systematic shift, but for a uniform source medium the scatter versus yield is as small or smaller than for m_b .

One of the most promising applications of yield estimates from regional phases is to combine yield estimates from different data sets to obtain a unified seismic yield estimate, with lower overall factor of uncertainty. Figure 23 illustrates how statistically independent yield estimates from 3 different seismic phases can be merged to give reduced uncertainties in the yields. The success of this procedure hinges on the independence of the different seismic phases as well as on the relative precision of the various yield estimates. For very small events, m_b values may only be available from a limited number of seismic arrays, and the regional phases will provide the primary constraint on the yield estimate. Seismological research is now focussed on the problems of detecting, discriminating, and estimating the yield of very small explosions, including possible decoupled explosions, to provide the technical means for enforcing restrictive testing treaties.

V. NUCLEAR TEST MONITORING AND THE EARTH SYSTEM

The most beneficial aspect of underground nuclear testing for Earth System Science is that the need to monitor foreign test programs has brought about great advances in the field of seismology, which have in turn revealed much about the dynamic Earth system and the natural hazards it poses for humanity. In turn, seismology continues to provide the only reliable means for globally monitoring underground nuclear testing, and will continue to be a cornerstone in the verification of any future very limited test ban treaties. Since nuclear weapons pose one of the greatest threats to human existence, inhibiting the proliferation of such devices is desirable, and seismology provides an important tool for reducing testing

and detecting any new weapon development programs. While there is diminishing enthusiasm for the use of nuclear explosions for large scale excavation or other peaceful applications, seismologists have always exploited the precise knowledge of explosion location and timing to interrogate deep Earth structure using the explosion seismic waves. Thus, ironically, the most beneficial peaceful application of nuclear testing has been for improving our knowledge of the deep Earth system.

Acknowledgment. Preparation of this article was supported by the W. M. Keck Foundation and the Defense Advanced Research Projects Agency and was monitored by the Geophysics Laboratory under contract F19628-89-K-0011. Contribution number 103 of the Institute of Tectonics and C. F. Richter Seismological Laboratory.

BIBLIOGRAPHY

- Bolt, B. A. (1976). "Nuclear Explosions and Earthquakes The Parted Veil", W. H. Freeman and Co..
- Dahlman, O. and H. Israelson (1977). "Monitoring Underground Nuclear Explosions", Elsevier, Amsterdam.
- Evernden, J. F., and G. E. Marsh (1987). "Yields of US and Soviet nuclear tests", Physics Today, August, 37-44.
- Kerr, A. U., editor (1985). "The VELA Program A Twenty-Five Year Review of Basic Research", Executive Graphic Services, Washington, D.C..
- Krepon, M., and M. Umberger, eds. (1988). "Verification and Compliance A Problem-Solving Approach", Macmillan Press LTD, London.
- Richards, P. G. (1989). "Seismic Monitoring of Nuclear Explosions", in The Encyclopedia of Solid Earth Geophysics, ed. D. E. James, Van Nostrand Reinhold Co., New York.
- Sykes, L. R., and J. F. Evernden (1982). "The verification of a comprehensive nuclear test ban", Scientific American, 247, 47-55.
- U. S. Congress, Office of Technology Assessment (1988). "Seismic Verification of Nuclear Testing Treaties" OTA-ISC-361, U. S. Government Printing Office, Washington, D. C..

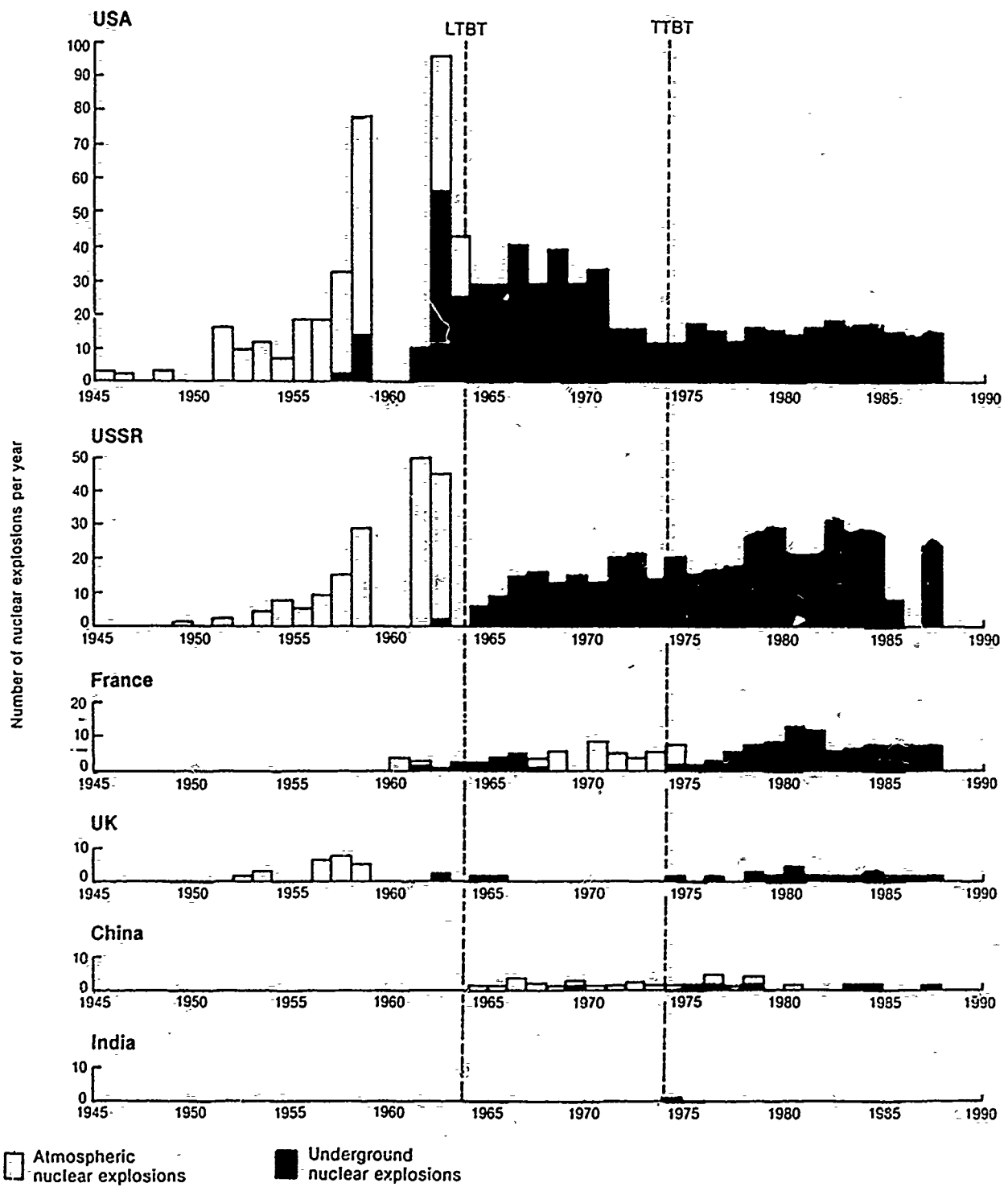


Fig. 1. Nuclear Testing during the period July 16, 1945 to December 31, 1987.

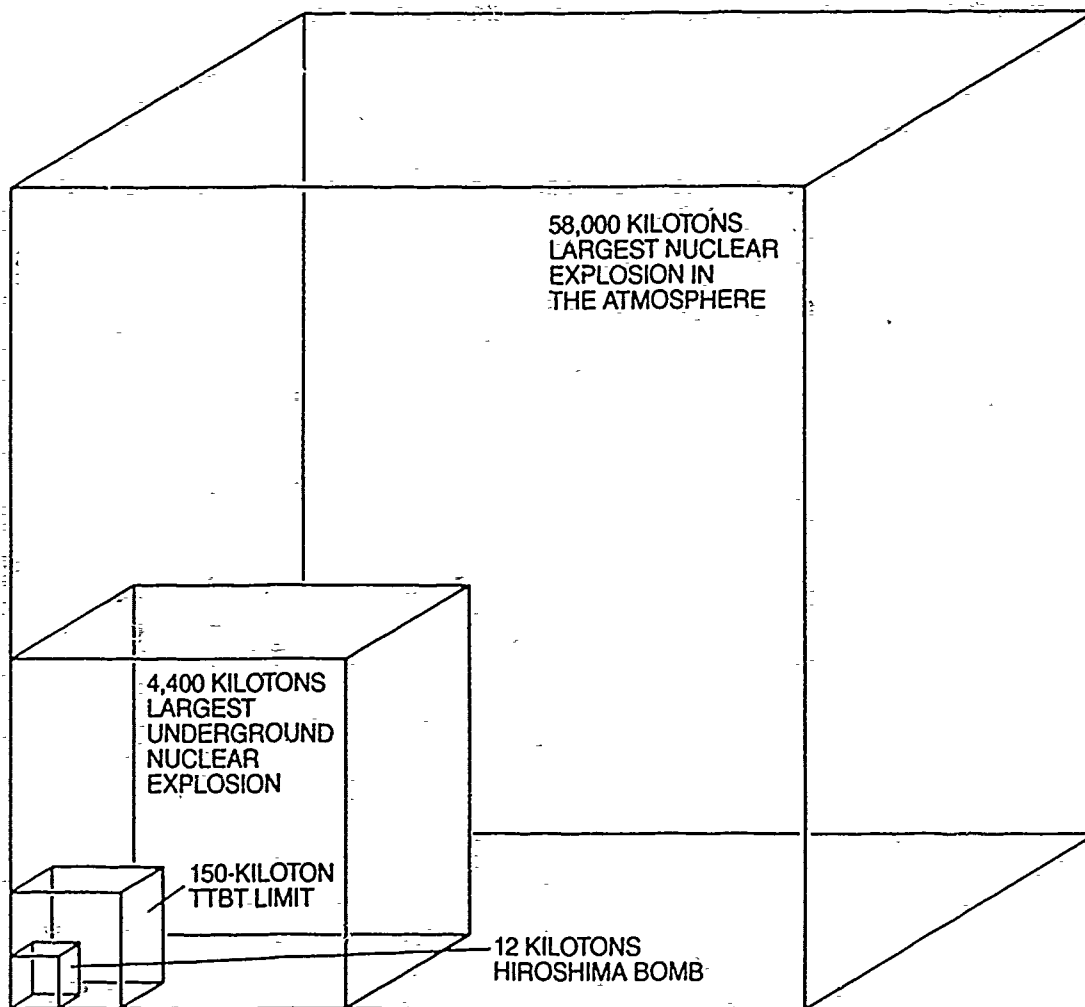


Fig. 2. Illustration of the variation in explosive energy of various nuclear devices. The volume of the boxes are proportional to the relative yield, with the largest box corresponding to a Soviet atmospheric test in 1961; the next smaller box corresponds to the U.S. test CANNIKIN conducted in 1971 on Amchitka Island; the 150-kiloton box corresponds to the testing limit set by the Threshold Test Ban Treaty (TTBT); and the smallest box represents the Hiroshima bomb. One kiloton is equal to the release of 10^{12} calories of energy, approximately equivalent to the energy in 1,000 tons of TNT.

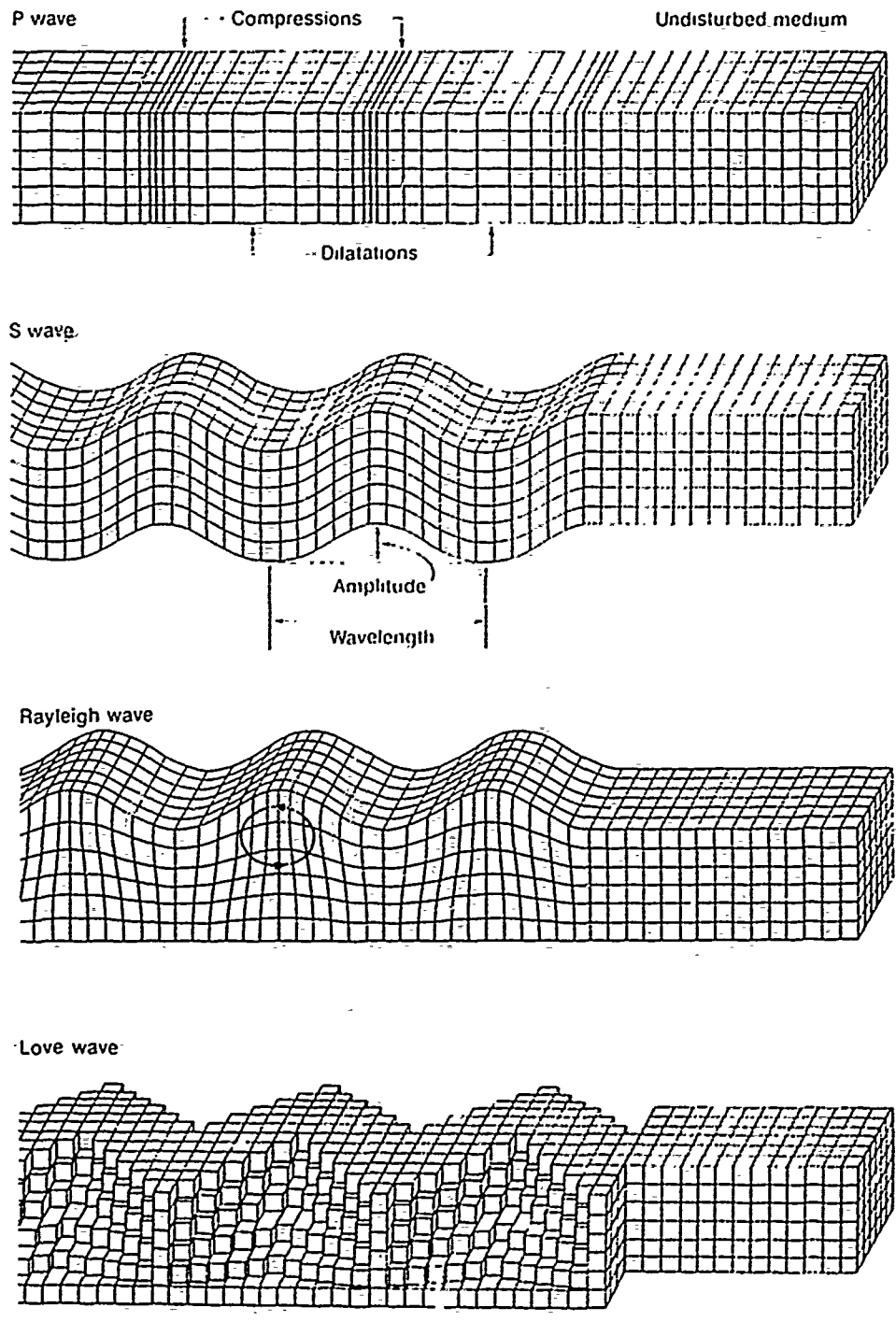


Fig. 3. The fundamental categories of seismic waves, with corresponding sense of particle motion as the wave propagates from left to right. The top two are body waves, which propagate throughout the Earth's interior. The lower two are surface waves, with particle motions confined to near the Earth's surface. Explosions preferentially excite short wavelength P waves and Rayleigh waves, while the shearing motion of earthquakes excites strong S waves and Love waves as well.

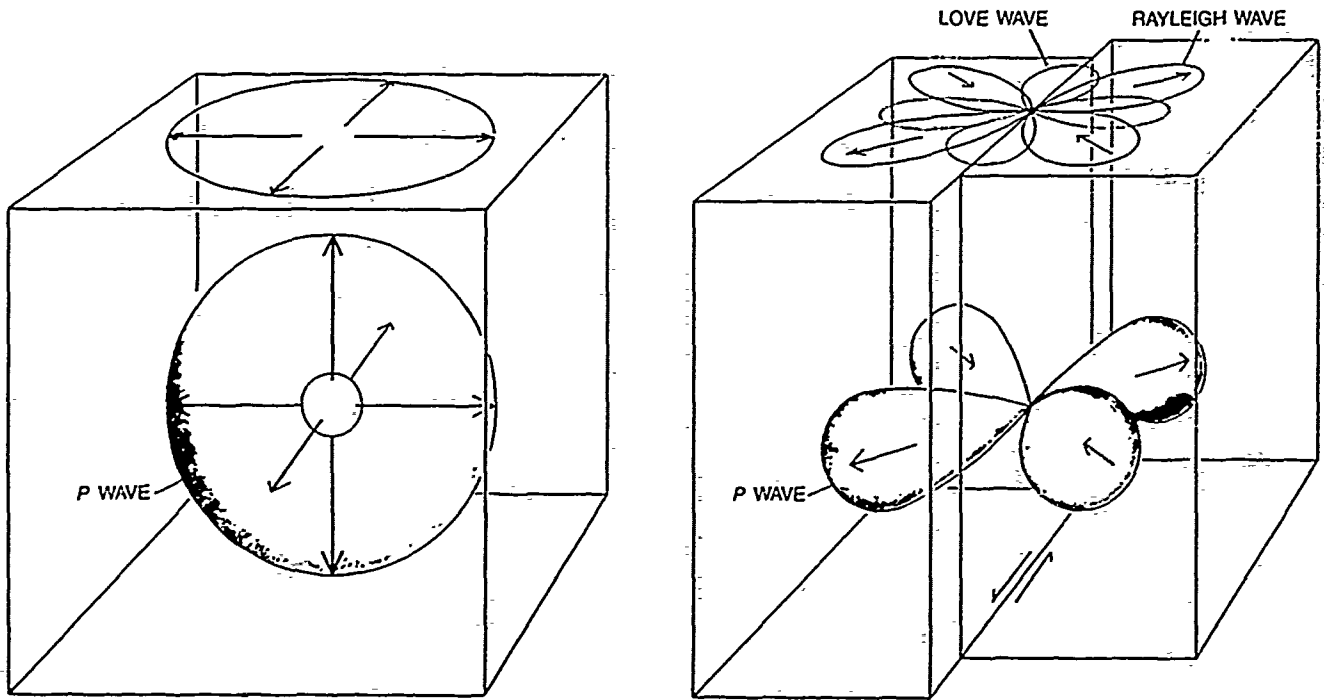


Fig. 4. Illustration of the symmetrical radiation of P wave and Rayleigh wave energy for an explosion (left), in contrast to the quadrupolar P, Rayleigh and Love wave radiation for a shear fault source.

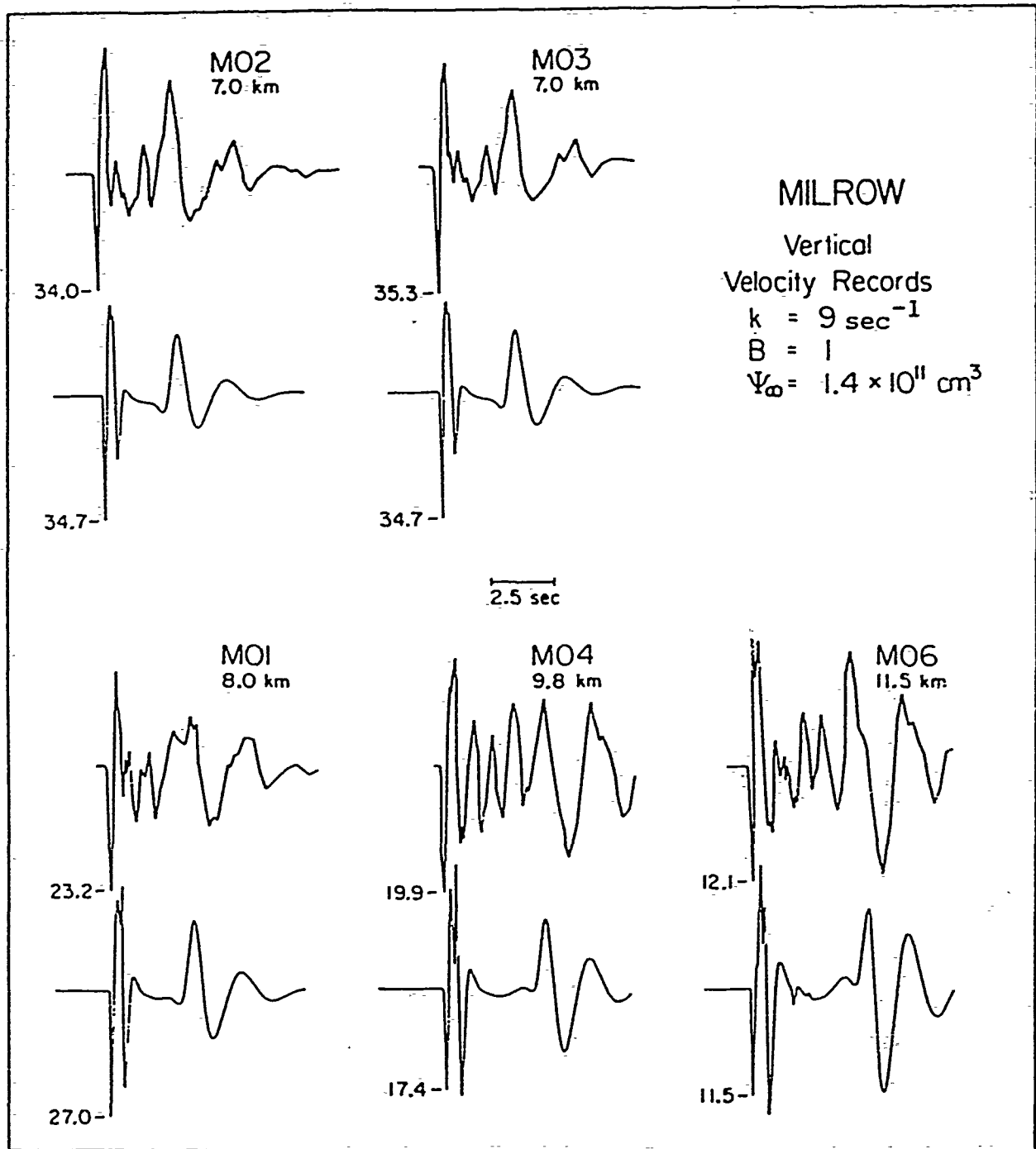


Fig. 5. Observed (top trace) and calculated P and Rayleigh waves from ground velocity seismometers within a few kilometers of a large underground explosion, illustrating how well elastic wave propagation theory can match observed signals from an explosion.

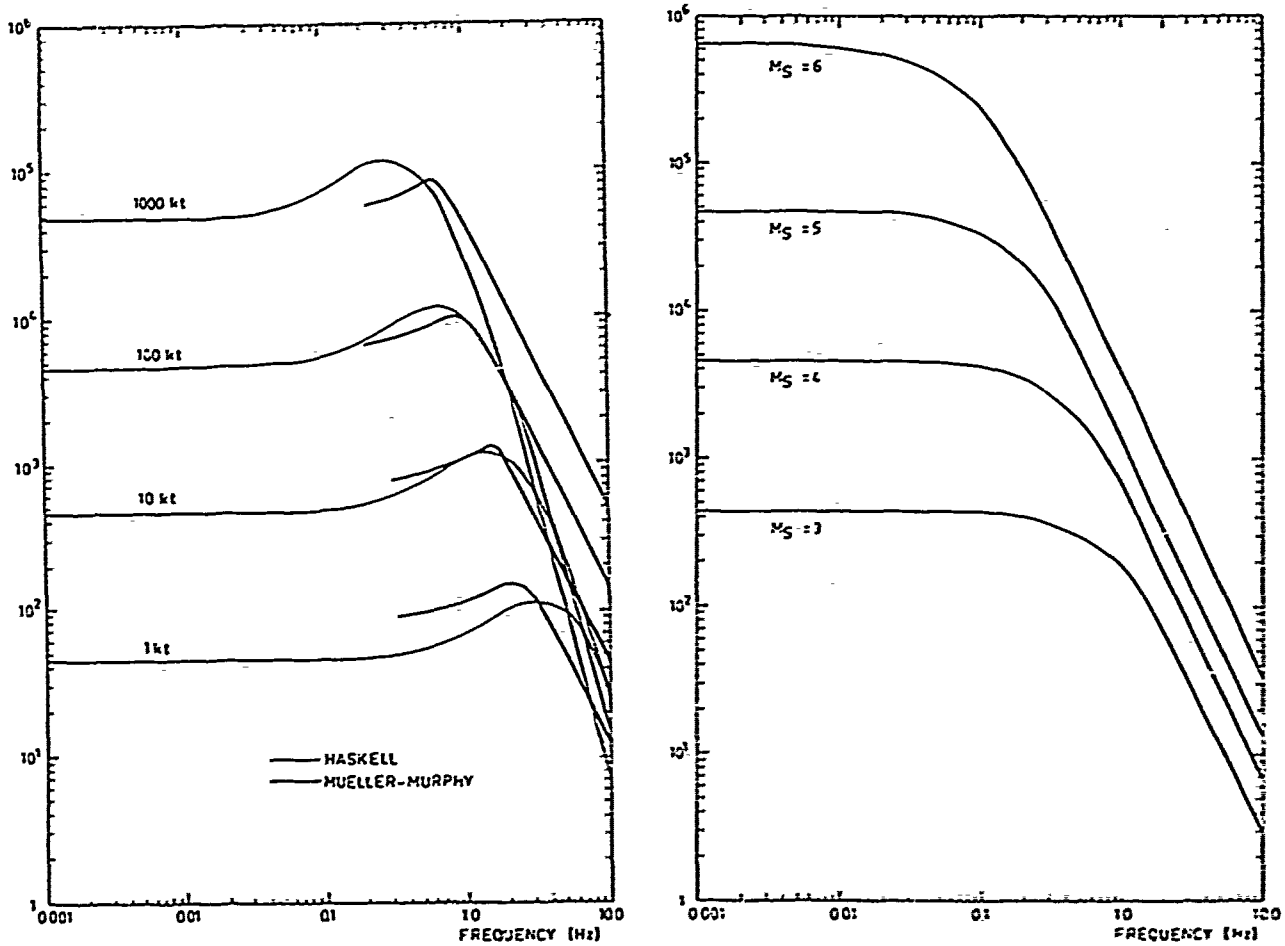


Fig. 6. Comparison of relative amplitude spectra for two explosion source models (left), and a model for earthquake spectra. Explosion source models differ in the scaling-with yield, the high frequency spectral fall-off, and the amount of overshoot (peaking) of the amplitude spectrum. The explosion and earthquake spectra are not on a common baseline, with only relative scaling being shown here.

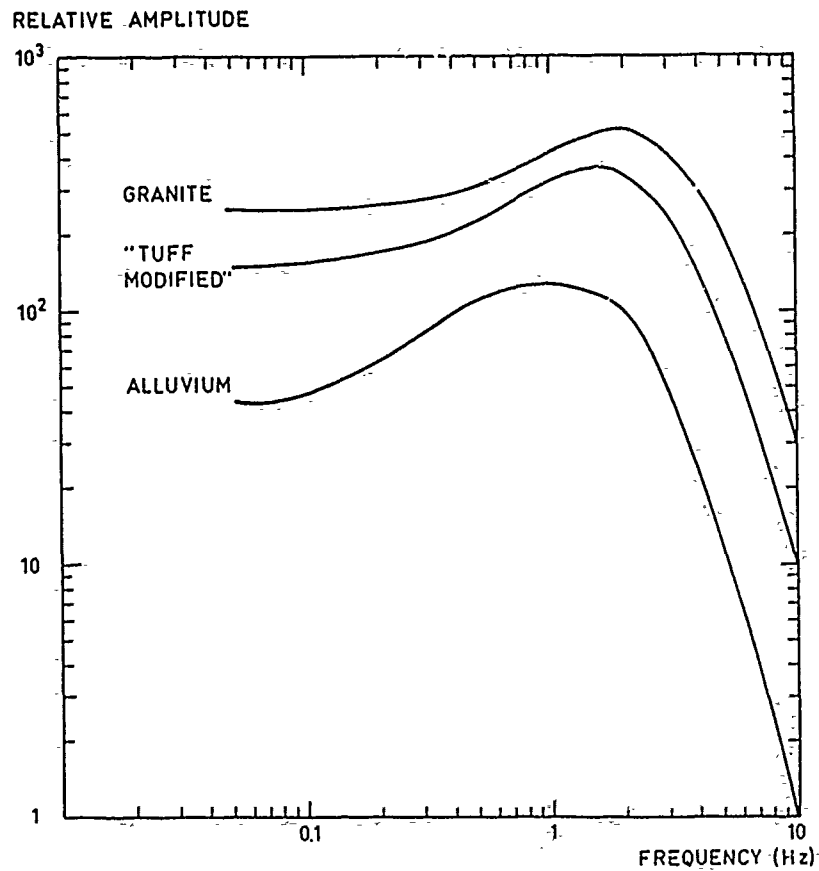


Fig. 7. Comparison of far-field amplitude spectra for equivalent 5 kt explosions in different source media. Note that harder rock couples better, in that stronger far-field amplitudes are produced. Knowledge of the source medium is important for estimating the strength of the source.

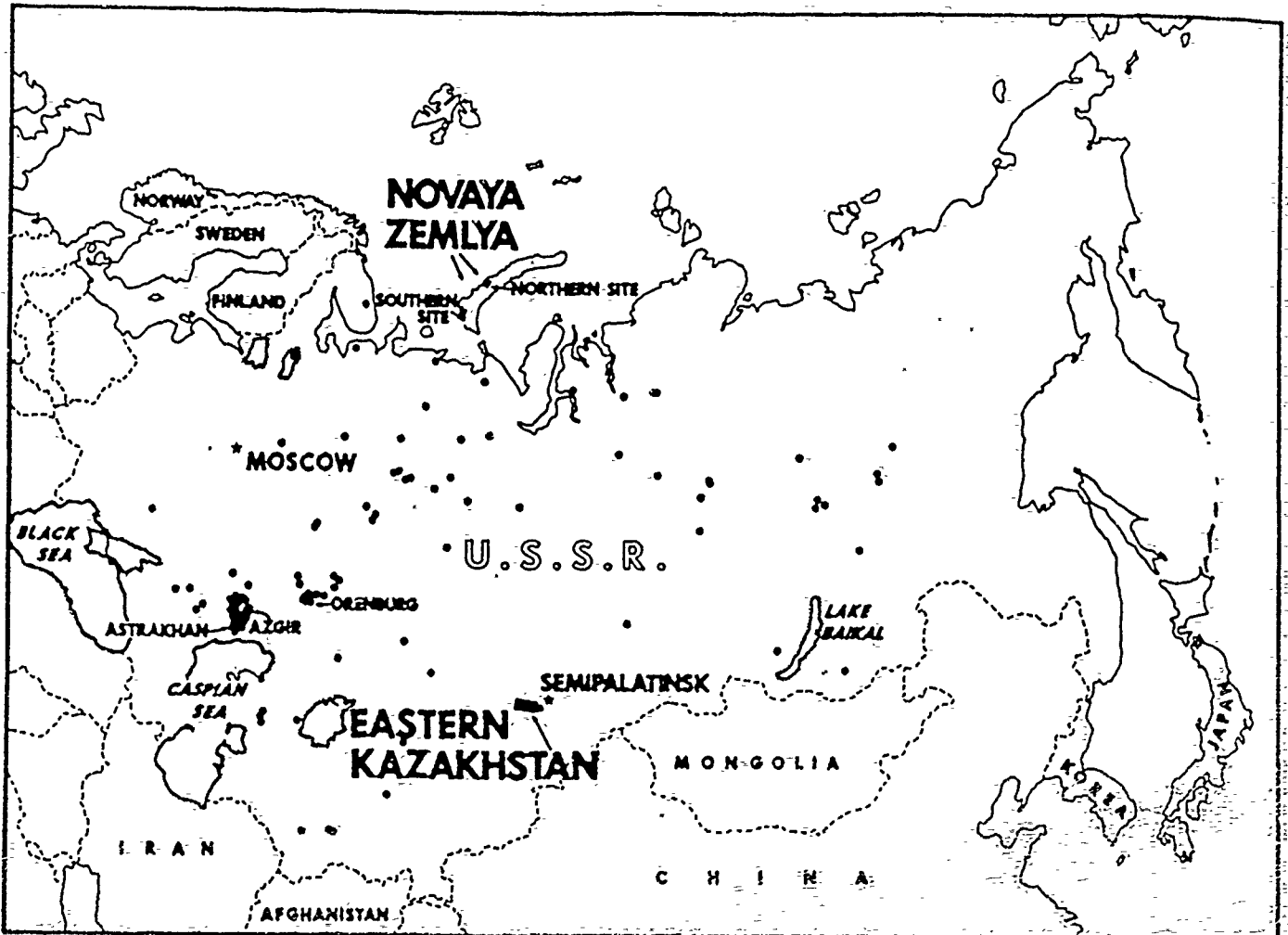


Fig. 8. Locations of underground nuclear tests in the Soviet Union. The primary test sites are in Novaya Zemlya and Eastern Kazakhstan. Many of the scattered tests have been conducted under the Peaceful Nuclear Explosion program, for the purpose of large scale excavation.

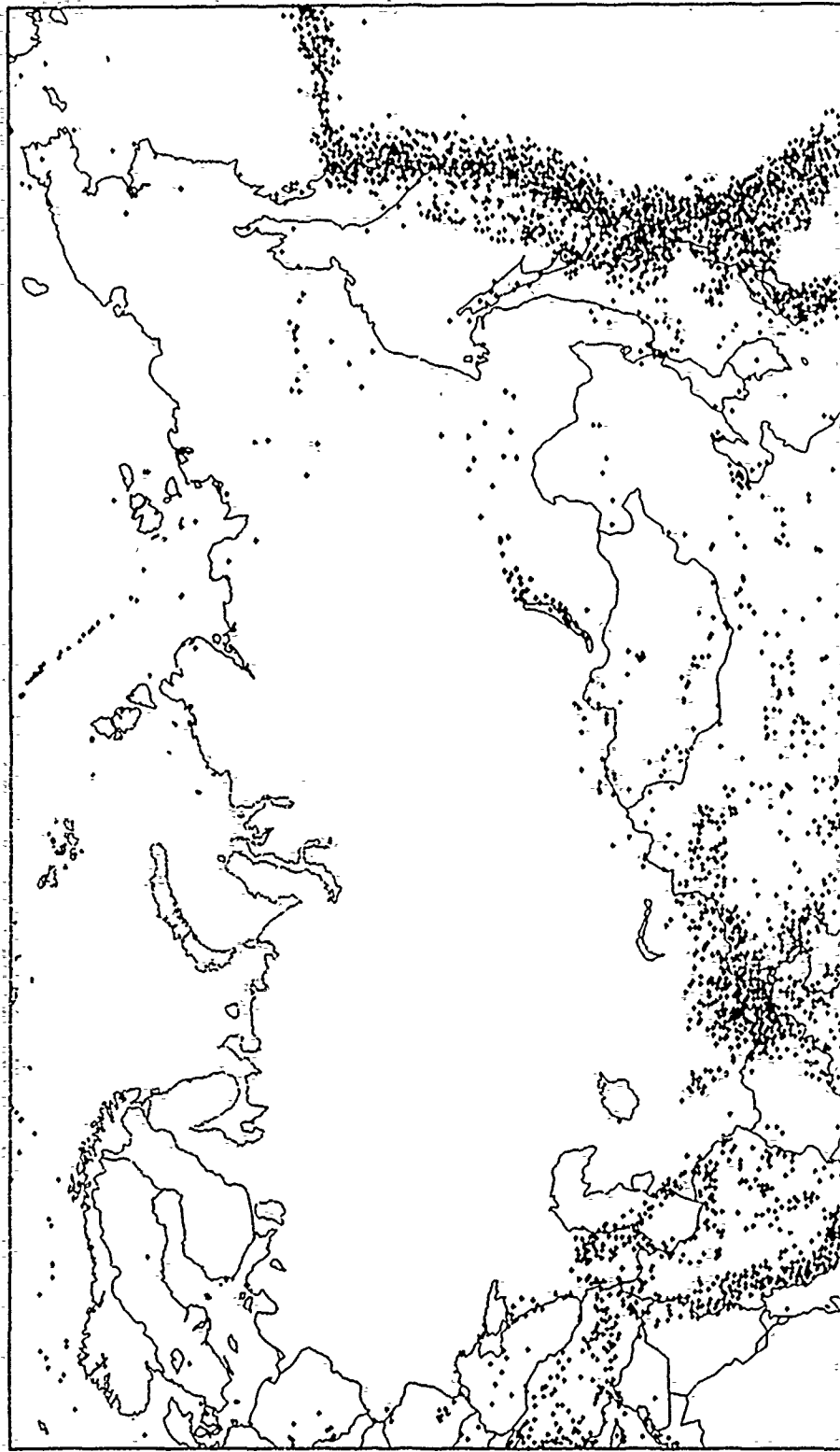


Fig. 9. Distribution of natural earthquake activity in the Soviet Union. Evasion techniques based on simulating an earthquake, hiding in an earthquake, or simply being very small, unidentifiable events, are most likely to take place in active earthquake zones.

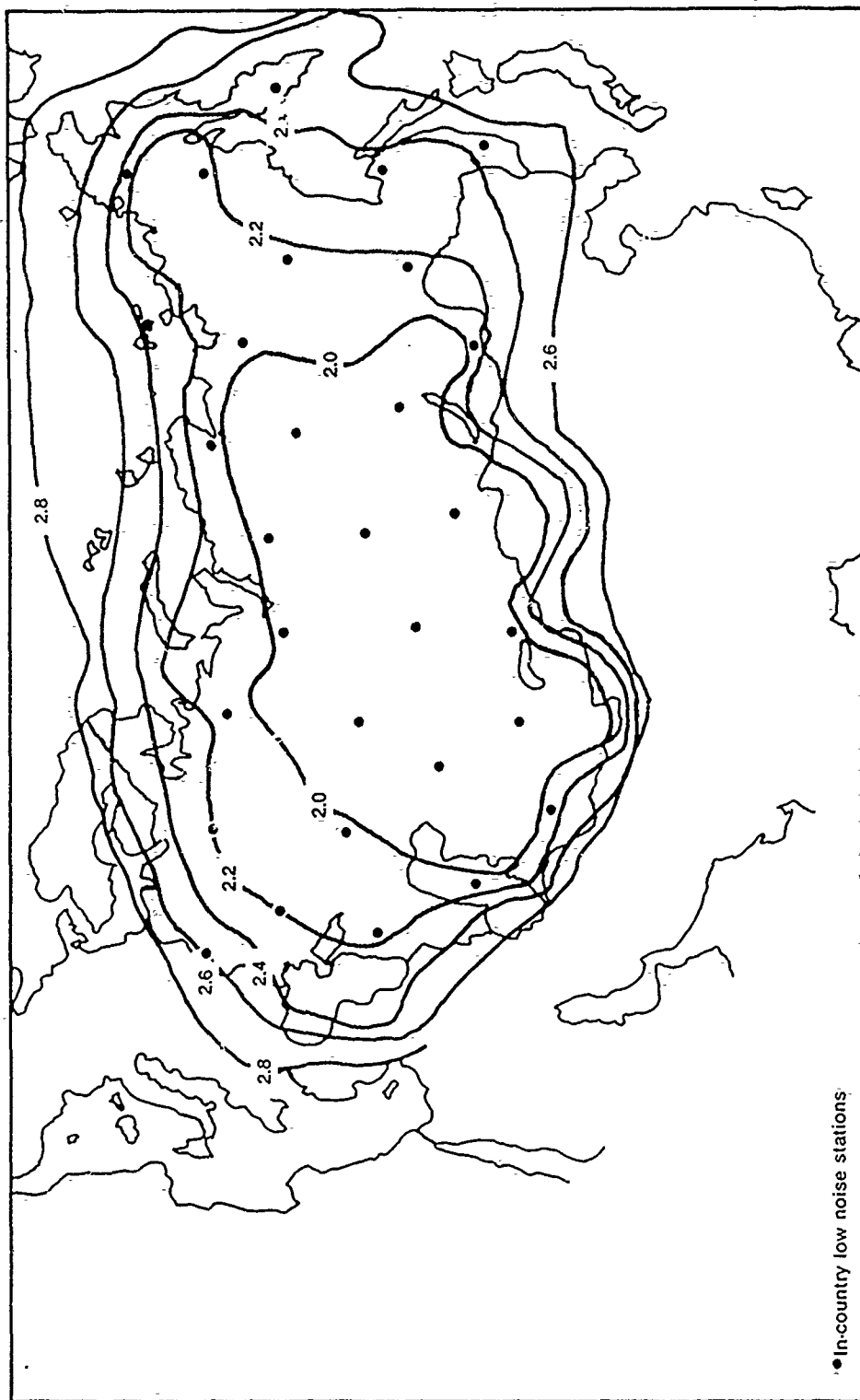


Fig. 10. Calculated explosion detection capability, in magnitude units, of an external network combined with 30 internal, low-noise arrays. This would allow detection at the 90% probability level for well coupled explosions of 0.1-0.01 kt, or fully decoupled explosions of about 1 kt.

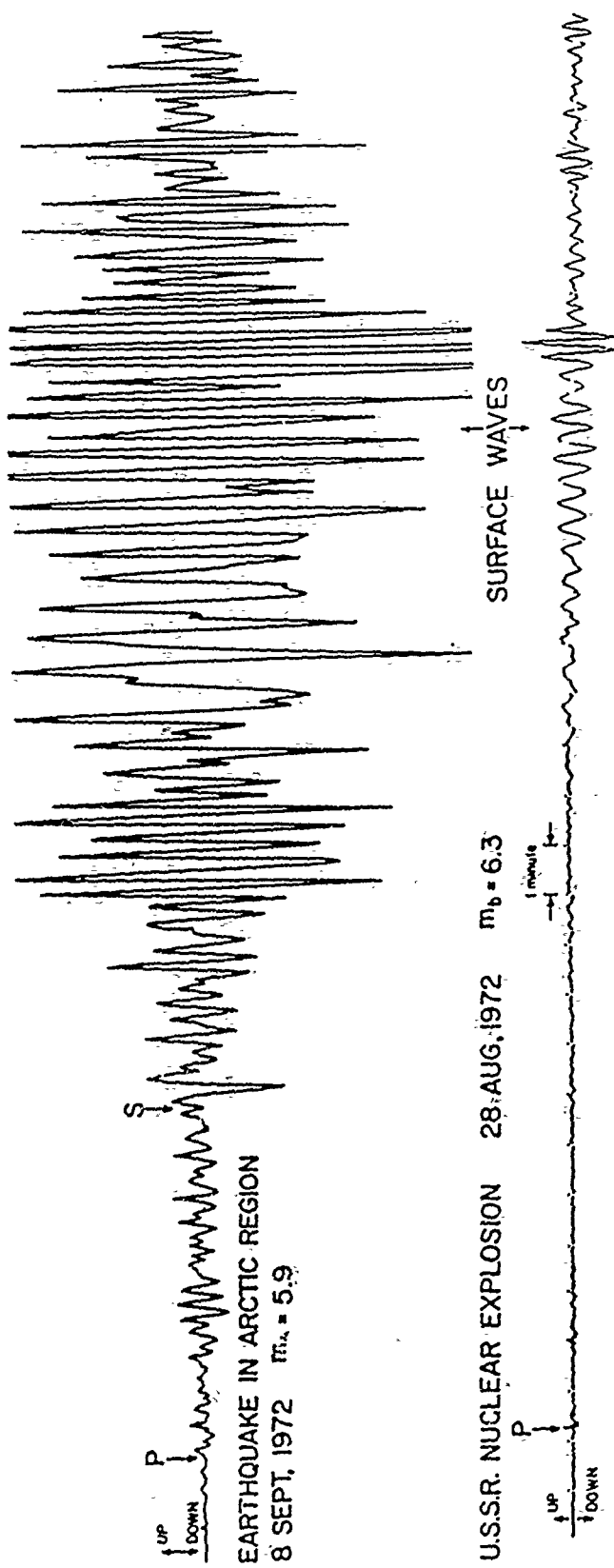


Fig. 11. Comparison of seismic signals recorded for an earthquake and an explosion that has slightly stronger high frequency P wave amplitudes. Note that the explosion has much smaller surface waves, and the P wave is much higher frequency than for the earthquake.

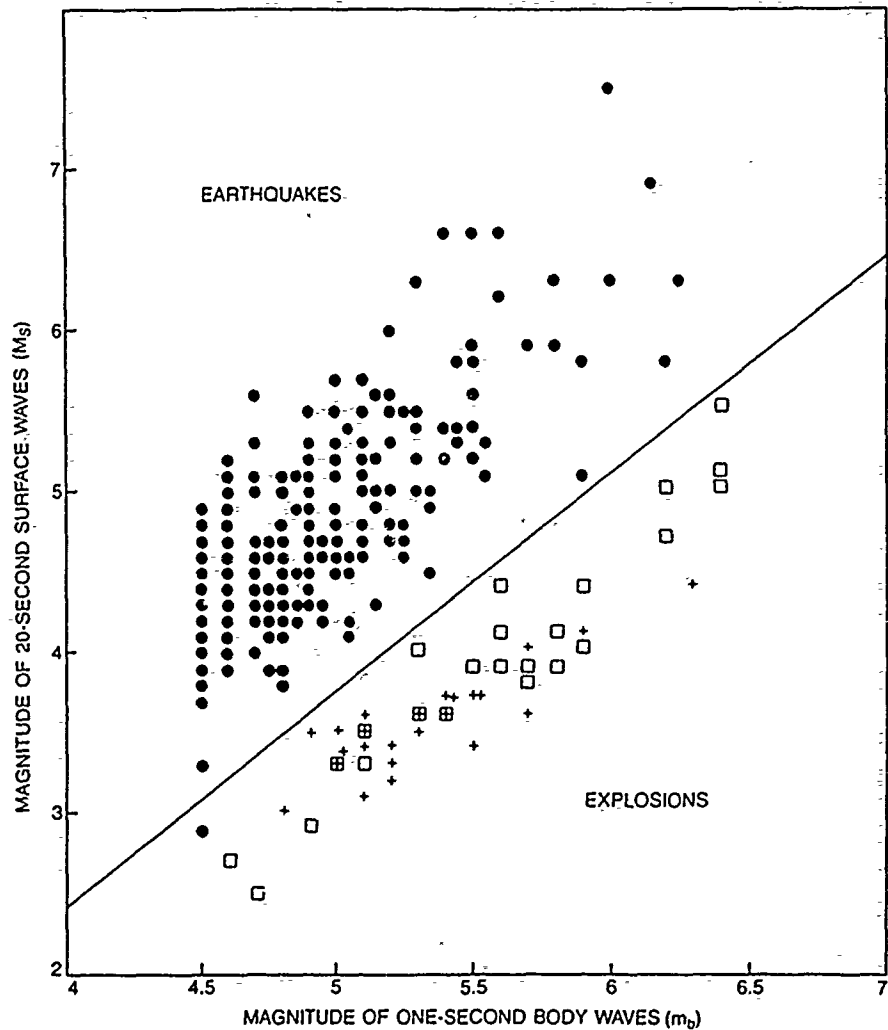


Fig. 12. A procedure for discriminating earthquakes from explosions based on differences in their relative excitation of long period surface waves (measured by M_s) and high frequency body waves (measured by m_b). Squares denote U.S. explosions, while crosses are Soviet explosions, and the m_b values are adjusted to account for regional variations in the amplitudes of short period waves.

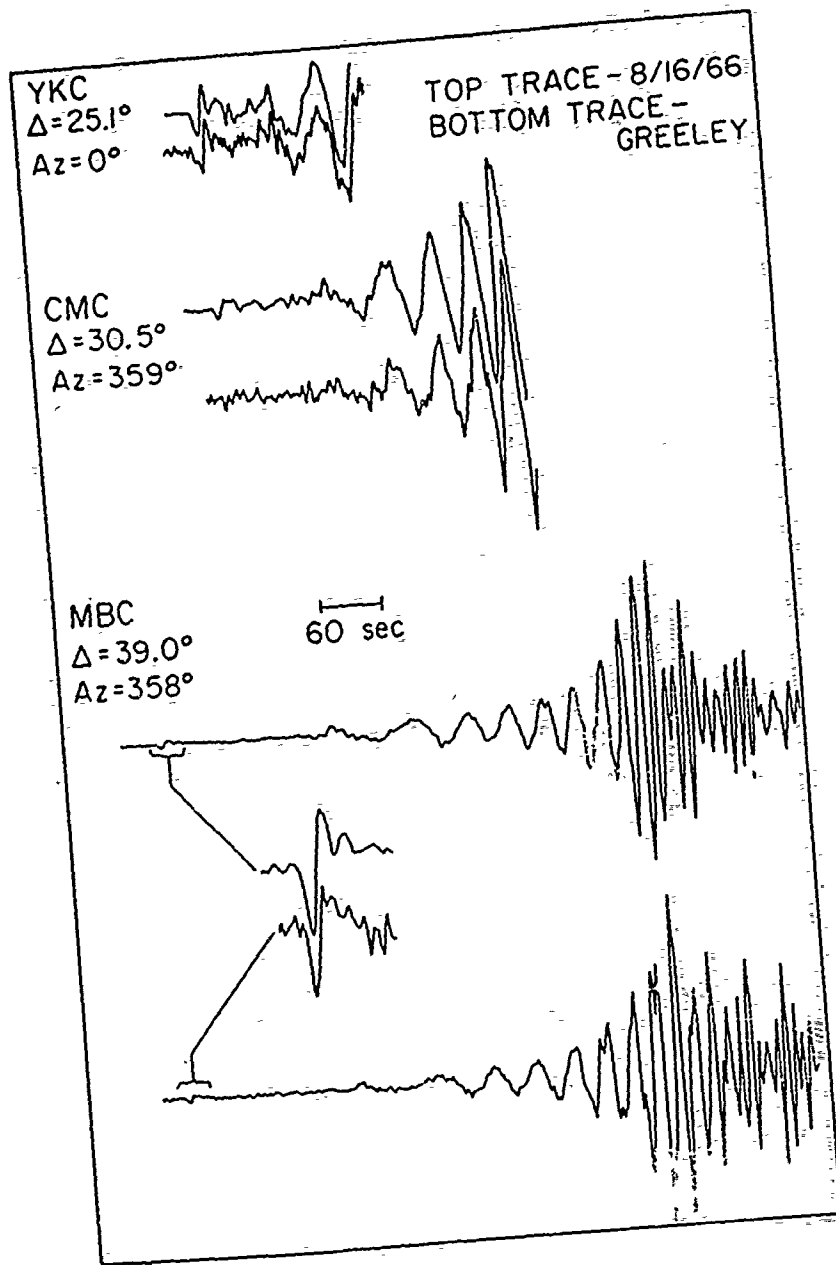


Fig. 13. Comparison of SH and Love wave recordings from an earthquake on August 16, 1966, and the NTS explosion GREELEY. The explosion produced a large amount of tectonic release, resulting in signals that are almost identical to an earthquake.

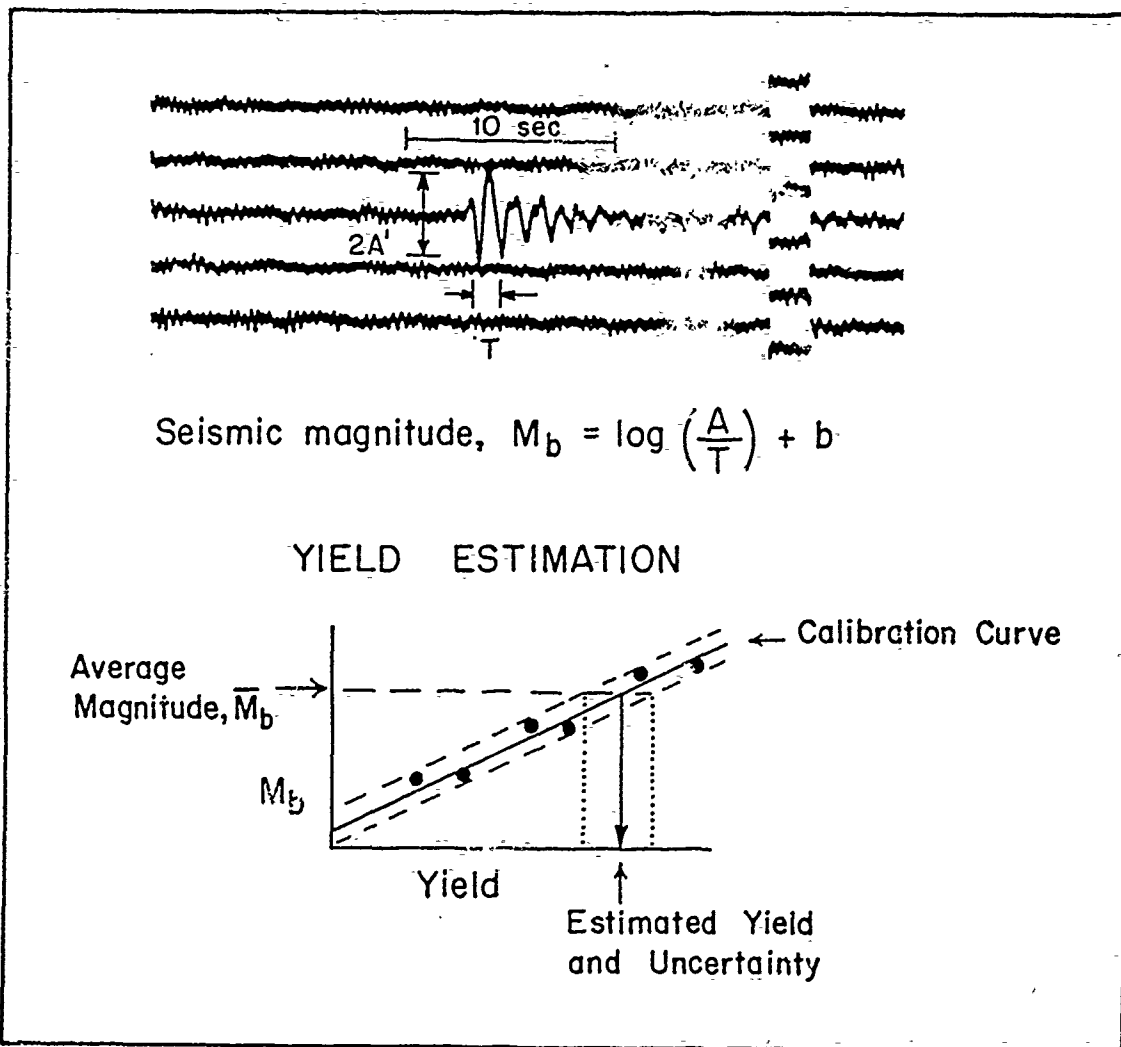


Fig. 14. Procedure for estimating seismic yield. The body wave magnitude is measured from an observed P wave recording, and the network average magnitude is compared with a calibration curve to estimate yield and its uncertainty.

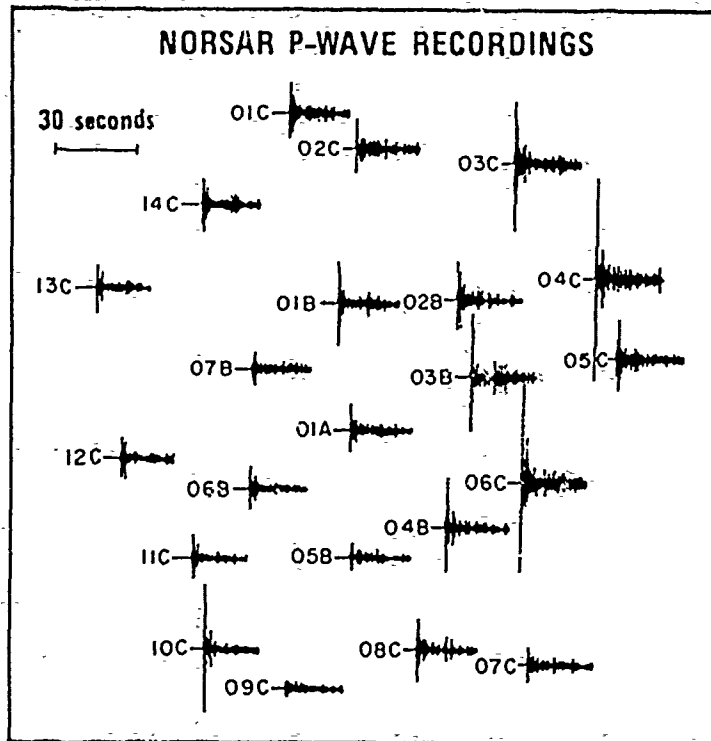
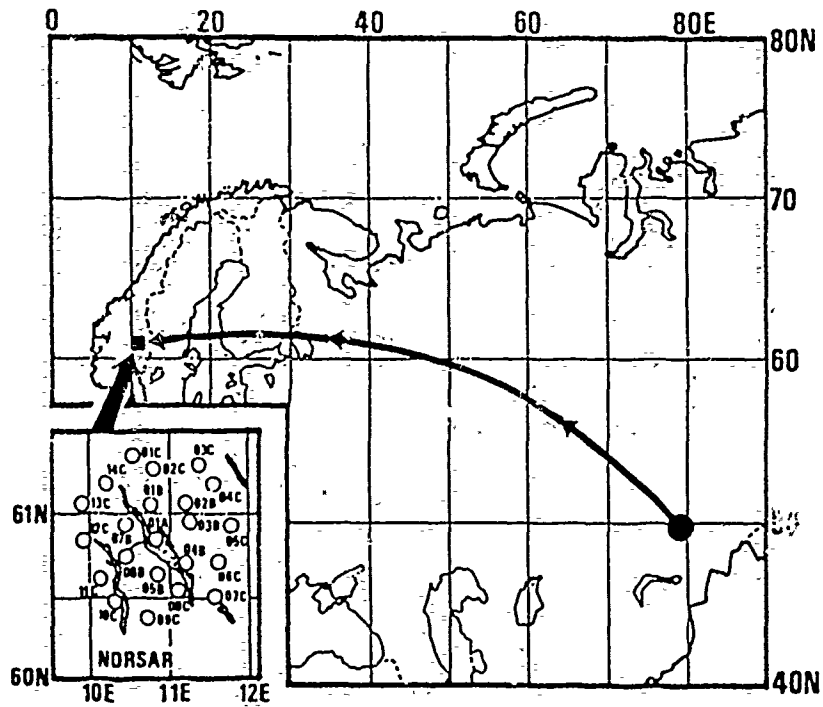


Fig. 15. Illustration of the variability of P wave amplitudes across a seismic array. This variability suggests the importance of both source and receiver corrections in the computation of magnitudes and yield determination.

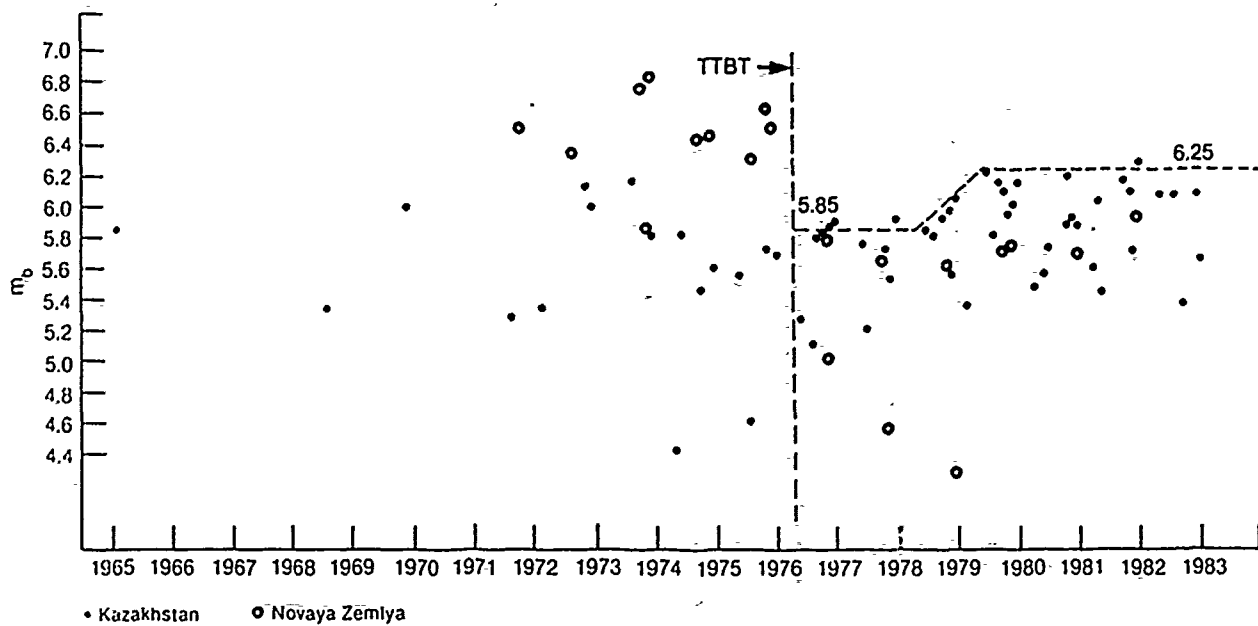


Fig. 16. Average magnitude of Soviet explosions as a function of time. Assessing Soviet compliance with the TTBT limit requires accurate determination of yield from the magnitudes.

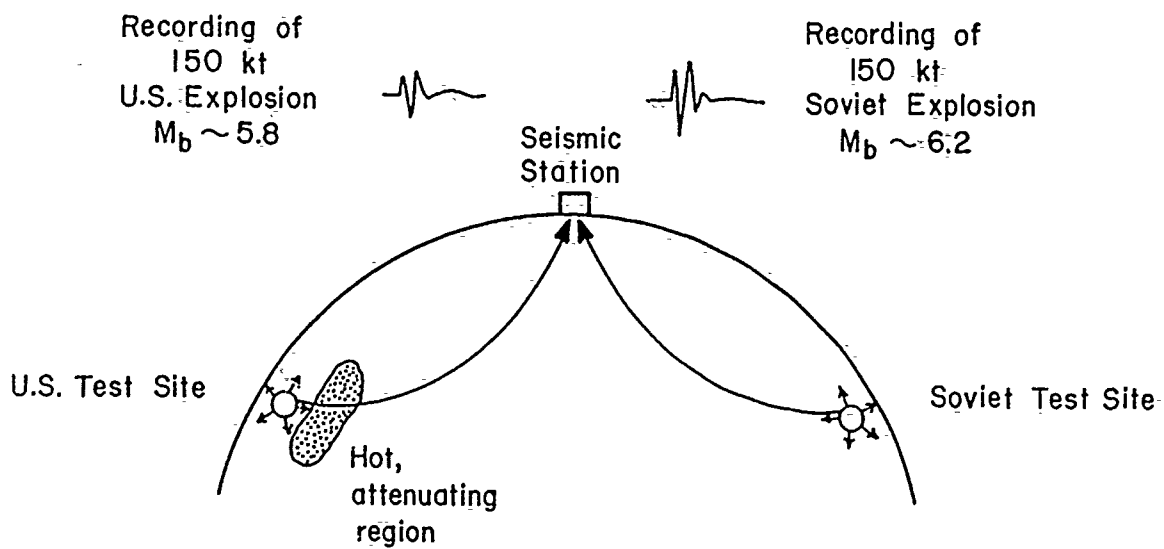


Fig. 17. Illustration of systematic effects on explosion magnitudes due to variation in properties under different source regions. As a result of strong attenuation of P wave energy under the Nevada Test Site, the m_b will be smaller than for the same size explosion at a Soviet site.

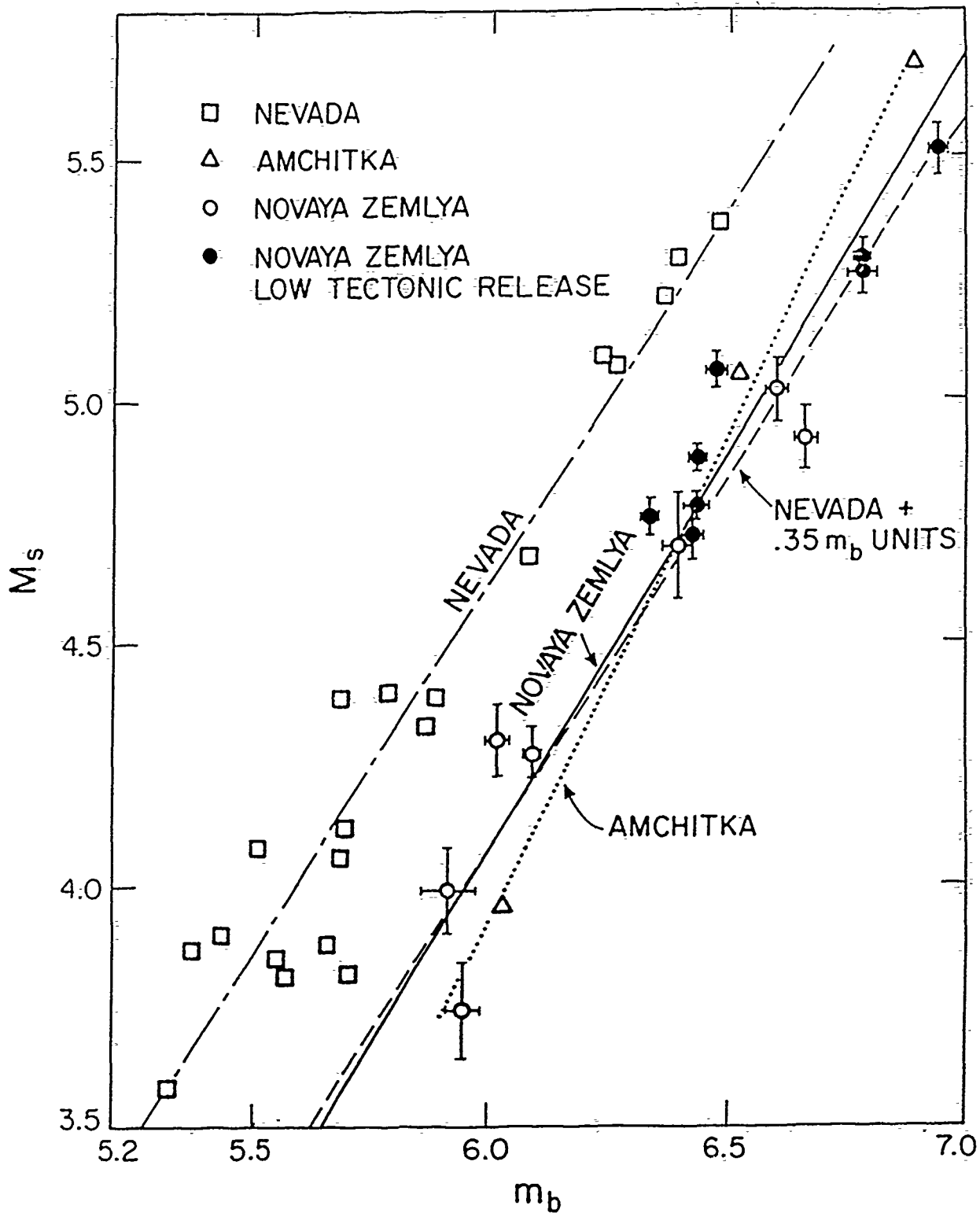


Fig. 18. Procedure for estimating source region baseline shifts based on relative behavior of different seismic magnitudes. Increasing the Nevada Test Site m_b values by 0.35 produces close agreement with the Amchitka and Novaya Zemlya test sites. M_s is believed to be less sensitive to variations in upper mantle properties than m_b .

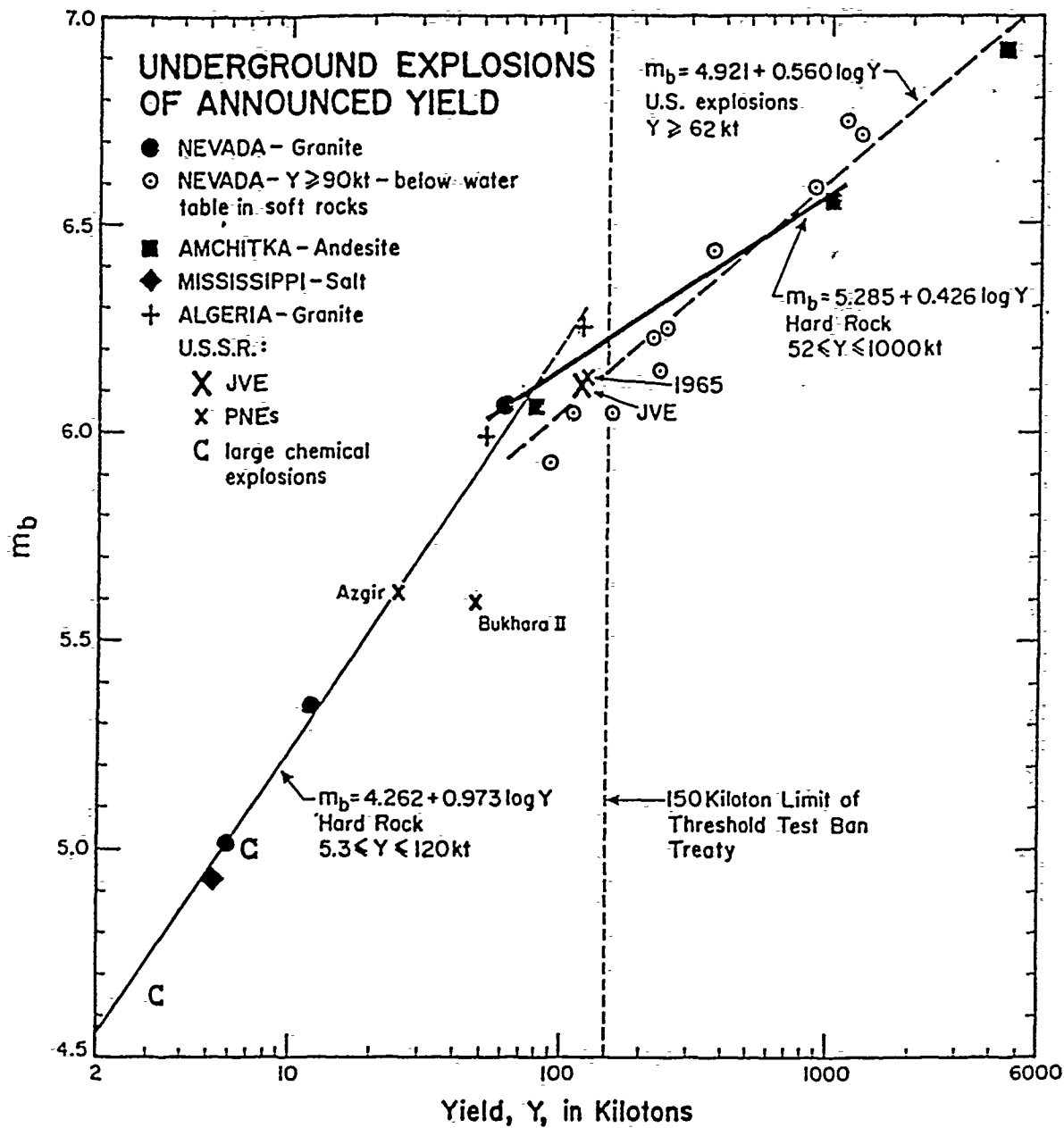


Fig. 19. Composite hard-rock magnitude-yield calibration curve. The data from different test sites have been shifted to correspond to the Shagan River, U.S.S.R. site. Three different regressions are shown to illustrate the variability of slope with yield. The measured values for the Joint Verification Experiment are compared with the reference curves, indicating that the seismic yield estimate based on the other data would be quite accurate.

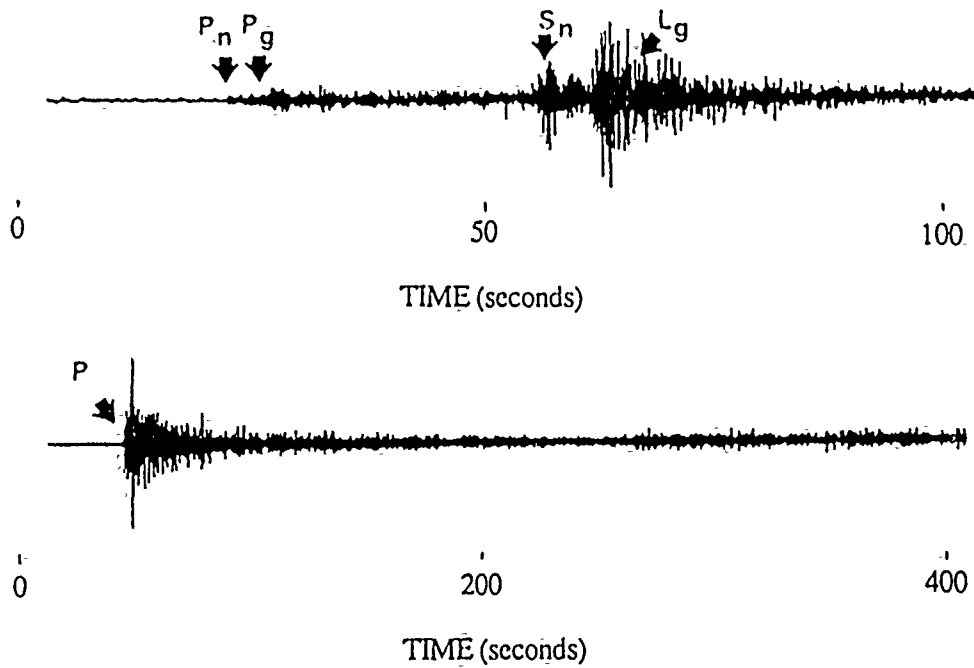


Fig. 21. Comparison of seismic waveforms recorded at regional (top) and teleseismic (bottom) distances. The P_n and S_n phases are refracted along the crust-mantle interface, while the P_g and L_g phases are intra-crustal reflections and reverberations. Magnitude-yield scales can be developed for each type of phase.

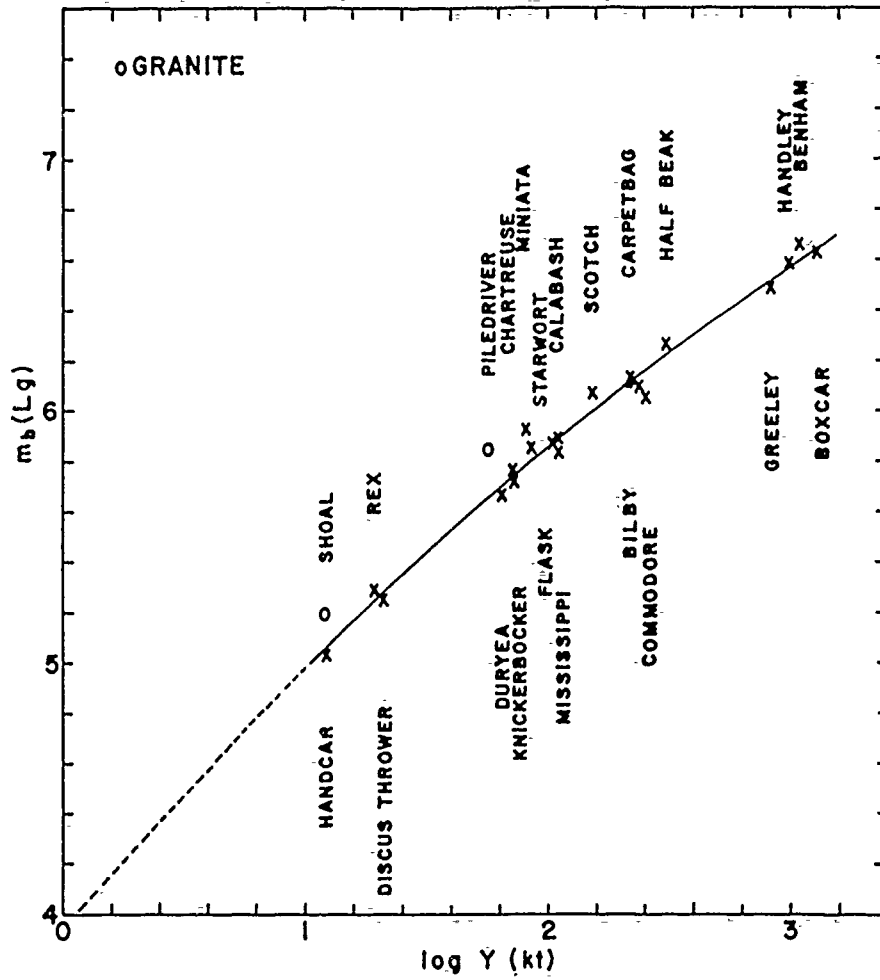


Fig. 22. Example of a magnitude-yield curve for L_g phases for U.S. explosions. Note the very small variation about the reference curve, indicating that L_g can be used to accurately determine yield for U.S. tests.

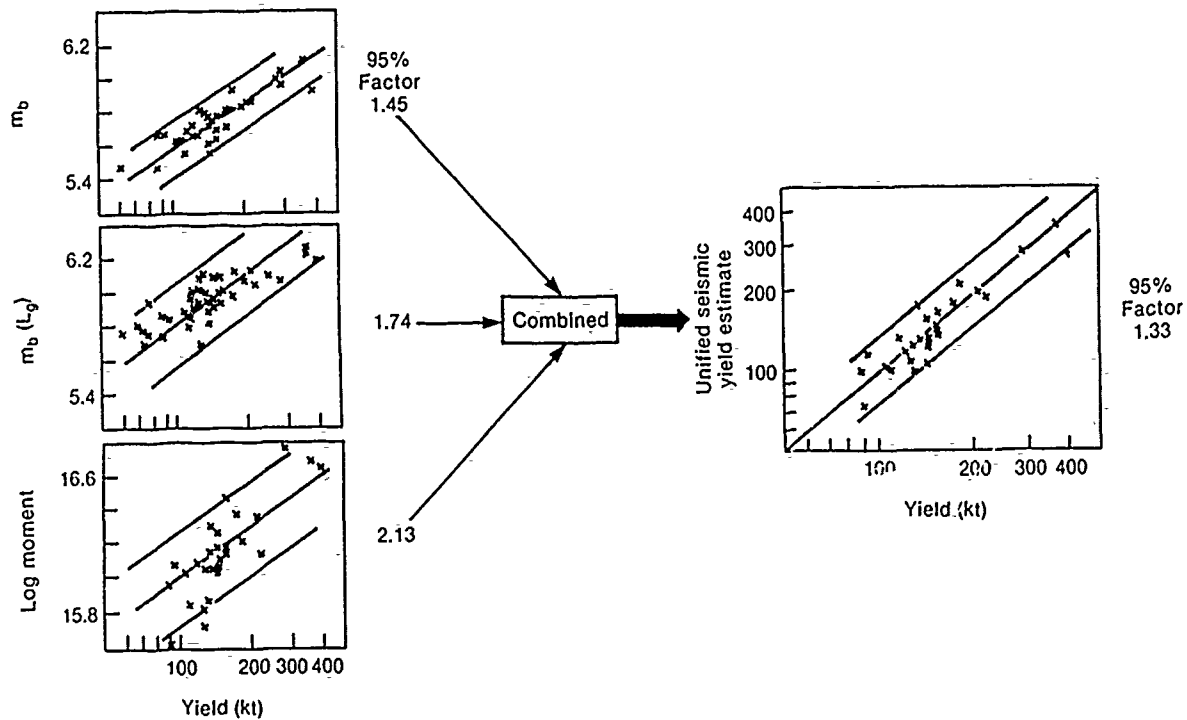


Fig. 23. Illustration of the unified yield estimation procedure, which exploits two or more yield estimates based on different wavetypes to reduce the uncertainty in yield estimates. The uncertainty factors are shown for a yield of about 150 kt. The success of this procedure depends on the degree to which the yield estimates are statistically independent. Further reduction of uncertainty can be accomplished by exploiting calibration shots which improve the baseline confidence of each procedure.

Prof. Thomas Ahrens
Seismological Lab, 252-21
Division of Geological & Planetary Sciences
California Institute of Technology
Pasadena, CA 91125

Prof. Charles B. Archambeau
CIRES
University of Colorado
Boulder, CO 80309

Dr. Thomas C. Bache, Jr.
Science Applications Int'l Corp.
10260 Campus Point Drive
San Diego, CA 92121 (2 copies)

Prof. Muawia Barazangi
Institute for the Study of the Continent
Cornell University
Ithaca, NY 14853

Dr. Jeff Barker
Department of Geological Sciences
State University of New York
at Binghamton
Vestal, NY 13901

Dr. Douglas R. Baumgardt
ENSCO, Inc
5400 Port Royal Road
Springfield, VA 22151-2388

Prof. Jonathan Berger
IGPP, A-025
Scripps Institution of Oceanography
University of California, San Diego
La Jolla, CA 92093

Dr. Gilbert A. Bollinger
Department of Geological Sciences
Virginia Polytechnical Institute
21044 Derring Hall
Blacksburg, VA 24061

Dr. Lawrence J. Burdick
Woodward-Clyde Consultants
566 El Dorado Street
Pasadena, CA 91109-3245

Dr. Jerry Carter
Center for Seismic Studies
1300 North 17th St., Suite 1450
Arlington, VA 22209-2308

Prof. Vernon F. Cormier
Department of Geology & Geophysics
U-45, Room 207
The University of Connecticut
Storrs, CT 06268

Professor Anton W. Dainty
Earth Resources Laboratory
Massachusetts Institute of Technology
42 Carleton Street
Cambridge, MA 02142

Prof. Steven Day
Department of Geological Sciences
San Diego State University
San Diego, CA 92182

Dr. Zoltan A. Der
ENSCO, Inc.
5400 Port Royal Road
Springfield, VA 22151-2388

Prof. Lewis M. Duncan
Dept. of Physics & Astronautics
Clemson University
Clemson, SC 29634-1901

Prof. John Ferguson
Center for Lithospheric Studies
The University of Texas at Dallas
P.O. Box 830688
Richardson, TX 75083-0688

Dr. Mark D. Fisk
Mission Research Corporation
735 State Street
P. O. Drawer 719
Santa Barbara, CA 93102

Prof. Stanley Flatte
Applied Sciences Building
University of California
Santa Cruz, CA 95064

Dr. Alexander Florence
SRI International
333 Ravenswood Avenue
Menlo Park, CA 94025-3493

Dr. Clifford Frohlich
Institute of Geophysics
8701 North Mopac
Austin, TX 78759

Dr. Holy K. Given
IGPP, A-025
Scripps Institute of Oceanography
University of California, San Diego
La Jolla, CA 92093

Prof. Henry L. Gray
Vice Provost and Dean
Department of Statistical Sciences
Southern Methodist University
Dallas, TX 75275

Dr. Indra Gupta
Teledyne Geotech
314 Montgomery Street
Alexandria, VA 22314

Prof. David G. Harkrider
Seismological Laboratory
Division of Geological & Planetary Sciences
California Institute of Technology
Pasadena, CA 91125

Prof. Danny Harvey
CI-ES
University of Colorado
Boulder, CO 80309

Prof. Donald V. Helmberger
Seismological Laboratory
Division of Geological & Planetary Sciences
California Institute of Technology
Pasadena, CA 91125

Prof. Eugene Herrin
Institute for the Study of Earth and Man
Geophysical Laboratory
Southern Methodist University
Dallas, TX 75275

Prof. Bryan Isacks
Cornell University
Department of Geological Sciences
SNEE Hall
Ithaca, NY 14850

Dr. Rong-Song Jih
Teledyne Geotech
314 Montgomery Street
Alexandria, VA 22314

Prof. Lane R. Johnson
Seismographic Station
University of California
Berkeley, CA 94720

Dr. Richard LaCoss
MIT-Lincoln Laboratory
M-200B
P. O. Box 73
Lexington, MA 02173-0073 (3 copies)

Prof Fred K. Lamb
University of Illinois at Urbana-Champaign
Department of Physics
1110 West Green Street
Urbana, IL 61801

Prof. Charles A. Langston
Geosciences Department
403 Deike Building
The Pennsylvania State University
University Park, PA 16802

Prof. Thorne Lay
Institute of Tectonics
Earth Science Board
University of California, Santa Cruz
Santa Cruz, CA 95064

Prof. Arthur Lerner-Lam
Lamont-Doherty Geological Observatory
of Columbia University
Palisades, NY 10964

Dr. Christopher Lynnes
Teledyne Geotech
314 Montgomery Street
Alexandria, VA 22314

Prof. Peter Malin
Department of Geology
Old Chemistry Bldg.
Duke University
Durham, NC 27706

Dr. Randolph Martin, III
New England Research, Inc.
76 Olcott Drive
White River Junction, VT 05001

Prof. Thomas V. McEvelly
Seismographic Station
University of California
Berkeley, CA 94720

Dr. Keith L. McLaughlin
S-CUBED
A Division of Maxwell Laboratory
P.O. Box 1620
La Jolla, CA 92038-1620

Prof. William Menke
Lamont-Doherty Geological Observatory
of Columbia University
Palisades, NY 10964

Stephen Miller
SRI International
333 Ravenswood Avenue
Box AF 116
Menlo Park, CA 94025-3493

Prof. Bernard Minster
IGPP, A-025
Scripps Institute of Oceanography
University of California, San Diego
La Jolla, CA 92093

Prof. Brian J. Mitchell
Department of Earth & Atmospheric Sciences
St. Louis University
St. Louis, MO 63156

Mr. Jack Murphy
S-CUBED, A Division of Maxwell Laboratory
11800 Sunrise Valley Drive
Suite 1212
Reston, VA 22091 (2 copies)

Prof. John A. Orcutt
IGPP, A-025
Scripps Institute of Oceanography
University of California, San Diego
La Jolla, CA 92093

Prof. Keith Priestley
University of Cambridge
Bullard Labs, Dept. of Earth Sciences
Madingley Rise, Madingley Rd.
Cambridge CB3 0EZ, ENGLAND

Dr. Jay J. Pulli
Radix Systems, Inc.
2 Taft Court, Suite 203
Rockville, MD 20850

Prof. Paul G. Richards
Lamont Doherty Geological Observatory
of Columbia University
Palisades, NY 10964

Dr. Wilmer Rivers
Teledyne Geotech
314 Montgomery Street
Alexandria, VA 22314

Prof. Charles G. Sammis
Center for Earth Sciences
University of Southern California
University Park
Los Angeles, CA 90089-0741

Prof. Christopher H. Scholz
Lamont-Doherty Geological Observatory
of Columbia University
Palisades, NY 10964

Thomas J. Sereno, Jr.
Science Application Int'l Corp.
10260 Campus Point Drive
San Diego, CA 92121

Prof. David G. Simpson
Lamont-Doherty Geological Observatory
of Columbia University
Palisades, NY 10964

Dr. Jeffrey Stevens
S-CUBED
A Division of Maxwell Laboratory
P.O. Box 1620
La Jolla, CA 92038-1620

Prof. Brian Stump
Institute for the Study of Earth & Man
Geophysical Laboratory
Southern Methodist University
Dallas, TX 75275

Prof. Jeremiah Sullivan
University of Illinois at Urbana-Champaign
Department of Physics
1110 West Green Street
Urbana, IL 61801

Prof. Clifford Thurber
University of Wisconsin-Madison
Department of Geology & Geophysics
1215 West Dayton Street
Madison, WI 53706

Prof. M. Nafi Toksoz
Earth Resources Lab
Massachusetts Institute of Technology
42 Carleton Street
Cambridge, MA 02142

Prof. John E. Vidale
University of California at Santa Cruz
Seismological Laboratory
Santa Cruz, CA 95064

Prof. Terry C. Wallace
Department of Geosciences
Building #77
University of Arizona
Tucson, AZ 85721

Dr. William Wortman
Mission Research Corporation
8560 Cinderbed Rd.
Suite # 700
Newington, VA 22122

Prof. Francis T. Wu
Department of Geological Sciences
State University of New York
at Binghamton
Vestal, NY 13901

UNITED STATES (Others)

Dr. Monem Abdel-Gawad
Rockwell International Science Center
1049 Camino Dos Rios
Thousand Oaks, CA 91360

Michael Browne
Teledyne Geotech
3401 Shiloh Road
Garland, TX 75041

Prof. Keiiti Aki
Center for Earth Sciences
University of Southern California
University Park
Los Angeles, CA 90089-0741

Mr. Roy Burger
1221 Serry Road
Schenectady, NY 12309

Prof. Shelton S. Alexander
Geosciences Department
403 Deike Building
The Pennsylvania State University
University Park, PA 16802

Dr. Robert Burrige
Schlumberger-Doll Research Center
Old Quarry Road
Ridgefield, CT 06877

Dr. Kenneth Anderson
BBNSTC
Mail Stop 14/1B
Cambridge, MA 02238

Dr. W. Winston Chan
Teledyne Geotech
314 Montgomery Street
Alexandria, VA 22314-1581

Dr. Ralph Archuleta
Department of Geological Sciences
University of California at Santa Barbara
Santa Barbara, CA 93102

Dr. Theodore Cherry
Science Horizons, Inc.
710 Encinitas Blvd., Suite 200
Encinitas, CA 92024 (2 copies)

Dr. Susan Beck
Department of Geosciences
Bldg. # 77
University of Arizona
Tucson, AZ 85721

Prof. Jon F. Claerbout
Department of Geophysics
Stanford University
Stanford, CA 94305

Dr. T.J. Bennett
S-CUBED
A Division of Maxwell Laboratory
11800 Sunrise Valley Drive, Suite 1212
Reston, VA 22091

Prof. Robert W. Clayton
Seismological Laboratory
Division of Geological & Planetary Sciences
California Institute of Technology
Pasadena, CA 91125

Mr. William J. Best
907 Westwood Drive
Vienna, VA 22180

Prof. F. A. Dahlen
Geological and Geophysical Sciences
Princeton University
Princeton, NJ 08544-0636

Dr. N. Biswas
Geophysical Institute
University of Alaska
Fairbanks, AK 99701

Mr. Charles Doll
Earth Resources Laboratory
Massachusetts Institute of Technology
42 Carleton St.
Cambridge, MA 02142

Dr. Stephen Bratt
Center for Seismic Studies
1300 North 17th Street
Suite 1450
Arlington, VA 22209

Prof. Adam Dziewonski
Hoffman Laboratory, Harvard Univ.
Dept. of Earth Atmos. & Planetary Sciences
20 Oxford St
Cambridge, MA 02138

Prof. John Ebel
Department of Geology & Geophysics
Boston College
Chestnut Hill, MA 02167

Eric Fielding
SNEE Hall
INSTOC
Cornell University
Ithaca, NY 14853

Dr. John Foley
Phillips Laboratory/LWH
Hanscom AFB, MA 01731-5000

Prof. Donald Forsyth
Department of Geological Sciences
Brown University
Providence, RI 02912

Dr. Anthony Gangi
Texas A&M University
Department of Geophysics
College Station, TX 77843

Dr. Freeman Gilbert
IGPP, A-025
Scripps Institute of Oceanography
University of California
La Jolla, CA 92093

Mr. Edward Giller
Pacific Sierra Research Corp.
1401 Wilson Boulevard
Arlington, VA 22209

Dr. Jeffrey W. Given
SAIC
10260 Campus Point Drive
San Diego, CA 92121

Prof. Stephen Grand
University of Texas at Austin
Department of Geological Sciences
Austin, TX 78713-7909

Prof. Roy Greenfield
Geosciences Department
403 Deike Building
The Pennsylvania State University
University Park, PA 16802

Dan N. Hagedorn
Battelle
Pacific Northwest Laboratories
Battelle Boulevard
Richland, WA 99352

Dr. James Hannon
Lawrence Livermore National Laboratory
P. O. Box 808
Livermore, CA 94550

Prof. Robert B. Herrmann
Dept. of Earth & Atmospheric Sciences
St. Louis University
St. Louis, MO 63156

Ms. Heidi Houston
Seismological Laboratory
University of California
Santa Cruz, CA 95064

Kevin Hutchenson
Department of Earth Sciences
St. Louis University
3507 Laclede
St. Louis, MO 63103

Dr. Hans Israelsson
Center for Seismic Studies
1300 N. 17th Street, Suite 1450
Arlington, VA 22209-2308

Prof. Thomas H. Jordan
Department of Earth, Atmospheric
and Planetary Sciences
Massachusetts Institute of Technology
Cambridge, MA 02139

Prof. Alan Kafka
Department of Geology & Geophysics
Boston College
Chestnut Hill, MA 02167

Robert C. Kemerait
ENSCO, Inc.
445 Pineda Court
Melbourne, FL 32940

William Kikendall
Teledyne Geotech
3401 Shiloh Road
Garland, TX 75041

Prof. Leon Knopoff
University of California
Institute of Geophysics & Planetary Physics
Los Angeles, CA 90024

Prof. Jack Oliver
Department of Geology
Cornell University
Ithaca, NY 14850

Prof. John Kuo
Aldridge Laboratory of Applied Geophysics
Columbia University
842 Mudd Bldg.
New York, NY 10027

Dr. Kenneth Olsen
P. O. Box 1273
Linwood, WA 98046-1273

Prof. L. Timothy Long
School of Geophysical Sciences
Georgia Institute of Technology
Atlanta, GA 30332

Prof. Jeffrey Park
Department of Geology and Geophysics
Kline Geology Laboratory
P. O. Box 6666
New Haven, CT 06511-8130

Dr. Gary McCartor
Department of Physics
Southern Methodist University
Dallas, TX 75275

Howard J. Patton
Lawrence Livermore National Laboratory
L-205
P. O. Box 808
Livermore, CA 94550

Prof. Art McGarr
Mail Stop 977
Geological Survey
345 Middlefield Rd.
Menlo Park, CA 94025

Prof. Robert Phinney
Geological & Geophysical Sciences
Princeton University
Princeton, NJ 08544-0636

Dr. George Mellman
Sierra Geophysics
11255 Kirkland Way
Kirkland, WA 98033

Dr. Paul Pomeroy
Rondout Associates
P.O. Box 224
Stone Ridge, NY 12484

Prof. John Nabelek
College of Oceanography
Oregon State University
Corvallis, OR 97331

Dr. Norton Rimer
S-CUBED
A Division of Maxwell Laboratory
P.O. Box 1620
La Jolla, CA 92038-1620

Prof. Geza Nagy
University of California, San Diego
Department of Ames, M.S. B-010
La Jolla, CA 92093

Prof. Larry J. Ruff
Department of Geological Sciences
1006 C.C. Little Building
University of Michigan
Ann Arbor, MI 48109-1063

Dr. Keith K. Nakanishi
Lawrence Livermore National Laboratory
L-205
P. O. Box 808
Livermore, CA 94550

Dr. Richard Sailor
TASC Inc.
55 Walkers Brook Drive
Reading, MA 01867

Prof. Amos Nur
Department of Geophysics
Stanford University
Stanford, CA 94305

Dr. Susan Schwartz
Institute of Tectonics
1156 High St.
Santa Cruz, CA 95064

John Sherwin
Teledyne Geotech
3401 Shiloh Road
Garland, TX 75041

Dr. Matthew Sibol
Virginia Tech
Seismological Observatory
4044 Derring Hall
Blacksburg, VA 24061-0420

Dr. Albert Smith
Lawrence Livermore National Laboratory
L-205
P. O. Box 808
Livermore, CA 94550

Prof. Robert Smith
Department of Geophysics
University of Utah
1400 East 2nd South
Salt Lake City, UT 84112

Dr. Stewart W. Smith
Geophysics AK-50
University of Washington
Seattle, WA 98195

Donald L. Springer
Lawrence Livermore National Laboratory
L-205
P. O. Box 808
Livermore, CA 94550

Dr. George Sutton
Rondout Associates
P.O. Box 224
Stone Ridge, NY 12484

Prof. L. Sykes
Lamont-Doherty Geological Observatory
of Columbia University
Palisades, NY 10964

Prof. Pradeep Talwani
Department of Geological Sciences
University of South Carolina
Columbia, SC 29208

Dr. David Taylor
ENSCO, Inc.
445 Pineda Court
Melbourne, FL 32940

Dr. Steven R. Taylor
Lawrence Livermore National Laboratory
L-205
P. O. Box 808
Livermore, CA 94550

Professor Ta-Liang Teng
Center for Earth Sciences
University of Southern California
University Park
Los Angeles, CA 90089-0741

Dr. Gregory van der Vink
IRIS, Inc.
1616 North Fort Myer Drive
Suite 1440
Arlington, VA 22209

Professor Daniel Walker
University of Hawaii
Institute of Geophysics
Honolulu, HI 96822

William R. Walter
Seismological Laboratory
University of Nevada
Reno, NV 89557

Dr. Raymond Willeman
Phillips Laboratory/LWH
Hanscom AFB, MA 01731-5000

Dr. Gregory Wojcik
Weidlinger Associates
4410 El Camino Real
Suite 110
Los Altos, CA 94022

Dr. Lorraine Wolf
Phillips Laboratory/LWH
Hanscom AFB, MA 01731-5000

Dr. Gregory B. Young
ENSCO, Inc.
5400 Port Royal Road
Springfield, VA 22151-2388

Dr. Eileen Vergino
Lawrence Livermore National Laboratory
L-205
P. O. Box 808
Livermore, CA 94550

J. J. Zucca
Lawrence Livermore National Laboratory
P. O. Box 808
Livermore, CA 94550

CONTRACTORS (Foreign)

Dr. Ramon Cabre, S.J.
Observatorio San Calixto
Casilla 5939
La Paz, Bolivia

Prof. Hans-Peter Harjes
Institute for Geophysik
Ruhr University/Bochum
P.O. Box 102148
4630 Bochum 1, FRG

Prof. Eystein Husebye
NTNF/NORSAR
P.O. Box 51
N-2007 Kjeller, NORWAY

Prof. Brian L.N. Kennett
Research School of Earth Sciences
Institute of Advanced Studies
G.P.O. Box 4
Canberra 2601, AUSTRALIA

Dr. Bernard Massinon
Societe Radiomana
27 rue Claude-Bernard
75005 Paris, FRANCE (2 Copies)

Dr. Pierre Mecheler
Societe Radiomana
27 rue Claude Bernard
75005 Paris, FRANCE

Dr. Svein Mykkeltveit
NTNF/NORSAR
P.O. Box 51
N-2007 Kjeller, NORWAY (3 copies)

FOREIGN (Others)

Dr. Peter Basham
Earth Physics Branch
Geological Survey of Canada
1 Observatory Crescent
Ottawa, Ontario, CANADA K1A 0Y3

Dr. Eduard Berg
Institute of Geophysics
University of Hawaii
Honolulu, HI 96822

Dr. Michel Bouchon
I.R.I.G.M.-B.P. 68
38402 St. Martin D'Herès
Cedex, FRANCE

Dr. Hilmar Bungum
NTNF/NORSAR
P.O. Box 51
N-2007 Kjeller, NORWAY

Dr. Michel Campillo
Observatoire de Grenoble
I.R.I.G.M.-B.P. 53
38041 Grenoble, FRANCE

Dr. Kin Yip Chun
Geophysics Division
Physics Department
University of Toronto
Ontario, CANADA M5S 1A7

Dr. Alan Douglas
Ministry of Defense
Blacknest, Brimpton
Reading RG7-4RS, UNITED KINGDOM

Dr. Manfred Henger
Federal Institute for Geosciences & Nat'l Res.
Postfach 510153
D-3000 Hanover 51, FRG

Ms. Eva Johannisson
Senior Research Officer
National Defense Research Inst.
P.O. Box 27322
S-102 54 Stockholm, SWEDEN

Dr. Fekadu Kebede
Geophysical Observatory, Science Faculty
Addis Ababa University
P. O. Box 1176
Addis Ababa, ETHIOPIA

Dr. Tormod Kvaerna
NTNF/NORSAR
P.O. Box 51
N-2007 Kjeller, NORWAY

Dr. Peter Marshall
Procurement Executive
Ministry of Defense
Blacknest, Brimpton
Reading FG7-4RS, UNITED KINGDOM

Prof. Ari Ben-Menahem
Department of Applied Mathematics
Weizman Institute of Science
Rehovot, ISRAEL 951729

Dr. Robert North
Geophysics Division
Geological Survey of Canada
1 Observatory Crescent
Ottawa, Ontario, CANADA K1A 0Y3

Dr. Frode Ringdal
NTNF/NORSAR
P.O. Box 51
N-2007 Kjeller, NORWAY

Dr. Jorg Schlittenhardt
Federal Institute for Geosciences & Nat'l Res.
Postfach 510153
D-3000 Hannover 51, FEDERAL REPUBLIC OF
GERMANY

Universita Degli Studi Di Trieste
Facolta Di Ingegneria
Istituto Di Miniere E. Geofisica Applicata, Trieste,
ITALY

Dr. John Woodhouse
Oxford University
Dept of Earth Sciences
Parks Road
Oxford OX13PR, ENGLAND

GOVERNMENT

Dr. Ralph Alewine III
DARPA/NMRO
1400 Wilson Boulevard
Arlington, VA 22209-2308

Mr. James C. Battis
Phillips Laboratory/LWH
Hanscom AFB, MA 01731-5000

Harley Benz
U.S. Geological Survey, MS-977
345 Middlefield Rd.
Menlo Park, CA 94025

Dr. Robert Blandford
AFTAC/TT
Center for Seismic Studies
1300 North 17th St. Suite 1450
Arlington, VA 22209-2308

E. Chael
Division 9241
Sandia Laboratory
Albuquerque, NM 87185

Dr. John J. Cipar
Phillips Laboratory/LWH
Hanscom AFB, MA 01731-5000

Cecil Davis
Group P-15, Mail Stop D406
P.O. Box 1663
Los Alamos National Laboratory
Los Alamos, NM 87544

Mr. Jeff Duncan
Office of Congressman Markey
2133 Rayburn House Bldg.
Washington, DC 20515

Dr. Jack Evernden
USGS - Earthquake Studies
345 Middlefield Road
Menlo Park, CA 94025

Art Frankel
USGS
922 National Center
Reston, VA 22092

Dr. Dale Glover
DIA/DT-1B
Washington, DC 20301

Dr. T. Hanks
USGS
Nat'l Earthquake Research Center
345 Middlefield Road
Menlo Park, CA 94025

Dr. Roger Hansen
AFTAC/TT
Patrick AFB, FL 32925

Paul Johnson
ESS-4, Mail Stop J979
Los Alamos National Laboratory
Los Alamos, NM 87545

Janet Johnston
Phillips Laboratory/LWH
Hanscom AFB, MA 01731-5000

Dr. Katharine Kadinsky-Cade
Phillips Laboratory/LWH
Hanscom AFB, MA 01731-5000

Ms. Ann Kerr
IGPP, A-025
Scripps Institute of Oceanography
University of California, San Diego
La Jolla, CA 92093

Dr. Max Koontz
US Dept of Energy/DP 5
Forrestal Building
1000 Independence Avenue
Washington, DC 20585

Dr. W.H.K. Lee
Office of Earthquakes, Volcanoes,
& Engineering
345 Middlefield Road
Menlo Park, CA 94025

Dr. William Leith
U.S. Geological Survey
Mail Stop 928
Reston, VA 22092

Dr. Richard Lewis
Director, Earthquake Engineering & Geophysics
U.S. Army Corps of Engineers
Box 631
Vicksburg, MS 39180

James F. Lewkowicz
Phillips Laboratory/LWH
Hanscom AFB, MA 01731-5000

Mr. Alfred Lieberman
ACDA/VI-OA State Department Bldg
Room 5726
320 - 21st Street, NW
Washington, DC 20451

Stephen Mangino
Phillips Laboratory/LWH
Hanscom AFB, MA 01731-5000

Dr. Robert Masse
Box 25046, Mail Stop 967
Denver Federal Center
Denver, CO 80225

Art McGarr
U.S. Geological Survey, MS-977
345 Middlefield Road
Menlo Park, CA 94025

Richard Morrow
ACDA/VI, Room 5741
320 21st Street N.W
Washington, DC 20451

Dr. Carl Newton
Los Alamos National Laboratory
P.O. Box 1663
Mail Stop C335, Group ESS-3
Los Alamos, NM 87545

Dr. Bao Nguyen
AFTAC/TTR
Patrick AFB, FL 32925

Dr. Kenneth H. Olsen
Los Alamos Scientific Laboratory
P. O. Box 1663
Mail Stop D-406
Los Alamos, NM 87545

Mr. Chris Paine
Office of Senator Kennedy
SR 315
United States Senate
Washington, DC 20510

Colonel Jerry J. Perrizo
AFOSR/NP, Building 410
Bolling AFB
Washington, DC 20332-6448

Dr. Frank F. Pilotte
HQ AFTAC/TT
Patrick AFB, FL 32925-6001

Katie Poley
CIA-ACIS/TMC
Room 4X16NHB
Washington, DC 20505

Mr. Jack Rachlin
U.S. Geological Survey
Geology, Rm 3 C136
Mail Stop 928 National Center
Reston, VA 22092

Dr. Robert Reinke
WL/NTEG
Kirtland AFB, NM 87117-6008

Dr. Byron Ristvet
HQ DNA, Nevada Operations Office
Attn: NVCG
P.O. Box 98539
Las Vegas, NV 89193

Dr. George Rothe
HQ AFTAC/TTR
Patrick AFB, FL 32925-6001

Dr. Alan S. Ryall, Jr.
DARPA/NMRO
1400 Wilson Boulevard
Arlington, VA 22209-2308

Dr. Michael Shore
Defense Nuclear Agency/SPSS
6801 Telegraph Road
Alexandria, VA 22310

Mr. Charles L. Taylor
Phillips Laboratory/LWH
Hanscom AFB, MA 01731-5000

Phillips Laboratory
Attn: XO
Hanscom AFB, MA 01731-5000

Dr. Larry Turnbull
CIA-OSWR/NED
Washington, DC 20505

Phillips Laboratory
Attn: LW
Hanscom AFB, MA 01731-5000

Dr. Thomas Weaver
Los Alamos National Laboratory
P.O. Box 1663, Mail Stop C335
Los Alamos, NM 87545

DARPA/PM
1400 Wilson Boulevard
Arlington, VA 22209

Phillips Laboratory
Research Library
ATTN: SULL
Hanscom AFB, MA 01731-5000

Defense Technical Information Center
Cameron Station
Alexandria, VA 22314 (2 copies)

Phillips Laboratory
ATTN: SUL
Kirtland AFB, NM 87117-6008 (2 copies)

Defense Intelligence Agency
Directorate for Scientific & Technical Intelligence
Attn: DT1B
Washington, DC 20340-6158

Secretary of the Air Force
(SAFRD)
Washington, DC 20330

AFTAC/CA
(STINFO)
Patrick AFB, FL 32925-6001

Office of the Secretary Defense
DDR & E
Washington, DC 20330

TACTEC
Battelle Memorial Institute
505 King Avenue
Columbus, OH 43201 (Final Report Only)

HQ DNA
Attn: Technical Library
Washington, DC 20305

DARPA/RMO/RETRIEVAL
1400 Wilson Boulevard
Arlington, VA 22209

DARPA/RMO/Security Office
1400 Wilson Boulevard
Arlington, VA 22209